Jordan Journal of Mechanical and Industrial Engineering (JJMIE)

JJMIE is a high-quality scientific journal devoted to fields of Mechanical and Industrial Engineering. It is published by The Jordanian Ministry of Higher Education and Scientific Research in corporation with the Hashemite University.

SUBMISSION ADDRESS:

Prof. **Mousa S. Mohsen**, Editor-in-Chief
Jordan Journal of Mechanical & Industrial Engineering,
Hashemite University,
PO Box 330127, Zarqa, 13133 , Jordan

E-mail: jjmie@hu.edu.jo

Hashemite Kingdom of Jordan

Hashemite University

Jordan Journal of Mechanical and Industrial Engineering

JJMIE

An International Peer-Reviewed Scientific Journal

http://jjmie.hu.edu.jo/

ISSN 1995-6665

Jordan Journal of Mechanical and Industrial Engineering (JJMIE)

JJMIE is a high-quality scientific journal devoted to fields of Mechanical and Industrial Engineering. It is published by The Jordanian Ministry of Higher Education and Scientific Research in corporation with the Hashemite University.

Intruduction: The Editorial Board is very committed to build the Journal as one of the leading international journals in mechanical and industrial engineering sciences in the next few years. With the support of the Ministry of Higher Education and Scientific Research and Jordanian Universities, it is expected that a heavy resource to be channeled into the Journal to establish its international reputation. The Journal's reputation will be enhanced from arrangements with several organizers of international conferences in publishing selected best papers of the conference proceedings.

Aims and Scope: Jordan Journal of Mechanical and Industrial Engineering (JJMIE) is a refereed international journal to be of interest and use to all those concerned with research in various fields of, or closely related to, mechanical and industrial engineering disciplines. Jordan Journal of Mechanical and Industrial Engineering aims to provide a highly readable and valuable addition to the literature which will serve as an indispensable reference tool for years to come. The coverage of the journal includes all new theoretical and experimental findings in the fields of mechanical and industrial engineering or any closely related fields. The journal also encourages the submission of critical review articles covering advances in recent research of such fields as well as technical notes.

Guide for Authors

Manuscript Submission

High-quality submissions to this new journal are welcome now and manuscripts may be either submitted online or mail.

Online: For online submission upload one copy of the full paper including graphics and all figures at the online submission site, accessed via E-mail: jjmie@hu.edu.jo. The manuscript must be written in MS Word Format. All correspondence, including notification of the Editor's decision and requests for revision, takes place by e-mail and via the Author's homepage, removing the need for a hard-copy paper trail.

By Mail: Manuscripts (1 original and 3 copies) accompanied by a covering letter may be sent to the Editor-in-Chief. However, a copy of the original manuscript, including original figures, and the electronic files should be sent to the Editor-in-Chief. Authors should also submit electronic files on disk (one disk for text material and a separate disk for graphics), retaining a backup copy for reference and safety.

Note that contributions may be either submitted online or sent by mail. Please do NOT submit via both routes. This will cause confusion and may lead to delay in article publication. Online submission is preferred.

Submission address and contact:

Prof. **Mousa S. Mohsen**, Editor-in-Chief
Jordan Journal of Mechanical & Industrial Engineering,
Hashemite University,
PO Box 330127, Zarqa, 13115 , Jordan
E-mail: jjmie@hu.edu.jo

Types of contributions: Original research papers

Corresponding author: Clearly indicate who is responsible for correspondence at all stages of refereeing and publication, including post-publication. Ensure that telephone and fax numbers (with country and area code) are provided in addition to the e-mail address and the complete postal address. Full postal addresses must be given for all co-authors.

Original material: Submission of an article implies that the work described has not been published previously (except in the form of an abstract or as part of a published lecture or academic thesis), that it is not under consideration for publication elsewhere, that its publication is approved by all authors and that, if accepted, it will not be published elsewhere in the same form, in English or in any other language, without the written consent of the Publisher. Authors found to be deliberately contravening the submission guidelines on originality and exclusivity shall not be considered for future publication in this journal.

Supplying Final Accepted Text on Disk: If online submission is not possible: Once the paper has been accepted by the editor, an electronic version of the text should be submitted together with the final hardcopy of the manuscript. The electronic version must match the hardcopy exactly. We accept MS Word format only. Always keep a backup copy of the electronic file for reference and safety. Label the disk with your name. Electronic files can be stored on CD.

Notification: Authors will be notified of the acceptance of their paper by the editor. The Publisher will also send a notification of receipt of the paper in production.

Copyright: All authors must sign the Transfer of Copyright agreement before the article can be published. This transfer agreement enables Jordan Journal of Mechanical and Industrial Engineering to protect the copyrighted material for the authors, but does not relinquish the authors' proprietary rights. The copyright transfer covers the exclusive rights to reproduce and distribute the article, including reprints, photographic reproductions, microfilm or any other reproductions of similar nature and translations.

PDF Proofs: One set of page proofs in PDF format will be sent by e-mail to the corresponding author, to be checked for typesetting/editing. The corrections should be returned within 48 hours. No changes in, or additions to, the accepted (and subsequently edited) manuscript will be allowed at this stage. Proofreading is solely the author's responsibility. Any queries should be answered in full. Please correct factual errors only, or errors introduced by typesetting. Please note that once your paper has been proofed we publish the identical paper online as in print.

Author Benefits

Page charge: Publication in this journal is free of charge.
Free off-prints: Three journal issues of which the article appears in along with twenty-five off-prints will be supplied free of charge to the corresponding author. Corresponding authors will be given the choice to buy extra off-prints before printing of the article.

Manuscript Preparation:

General: Editors reserve the right to adjust style to certain standards of uniformity. Original manuscripts are discarded after publication unless the Publisher is asked to return original material after use. If online submission is not possible, an electronic copy of the manuscript on disk should accompany the final accepted hardcopy version. Please use MS Word for the text of your manuscript.

Structure: Follow this order when typing manuscripts: Title, Authors, Affiliations, Abstract, Keywords, Introduction, Main text, Conclusions, Acknowledgements, Appendix, References, Figure Captions, Figures and then Tables. For submission in hardcopy, do not import figures into the text - see Illustrations. For online submission, please supply figures imported into the text AND also separately as original graphics files. Collate acknowledgements in a separate section at the end of the article and do not include them on the title page, as a footnote to the title or otherwise.

Text Layout: Use double spacing and wide (3 cm) margins. Ensure that each new paragraph is clearly indicated. Present tables and figure legends on separate pages at the end of the manuscript. If possible, consult a recent issue of the journal to become familiar with layout and conventions. All footnotes (except for table and corresponding author footnotes) should be identified with superscript Arabic numbers. To conserve space, authors are requested to mark the less important parts of the paper (such as records of experimental results) for printing in smaller type. For long papers (more that 4000 words) sections which could be deleted without destroying either the sense or the continuity of the paper should be indicated as a guide for the editor. Nomenclature should conform to that most frequently used in the scientific field concerned. Number all pages consecutively; use 12 or 10 pt font size and standard fonts. If submitting in hardcopy, print the entire manuscript on one side of the paper only.

Corresponding author: Clearly indicate who is responsible for correspondence at all stages of refereeing and publication, including post-publication. The corresponding author should be identified with an asterisk and footnote. Ensure that telephone and fax numbers (with country and area code) are provided in addition to the e-mail address and the complete postal address. Full postal addresses must be given for all co-authors. Please consult a recent journal paper for style if possible.

Abstract: A self-contained abstract outlining in a single paragraph the aims, scope and conclusions of the paper must be supplied.

Keywords: Immediately after the abstract, provide a maximum of six keywords (avoid, for example, 'and', 'of'). Be sparing with abbreviations: only abbreviations firmly established in the field may be eligible.

Symbols: All Greek letters and unusual symbols should be identified by name in the margin, the first time they are used.

Units: Follow internationally accepted rules and conventions: use the international system of units (SI). If other quantities are mentioned, give their equivalent in SI.

Maths: Number consecutively any equations that have to be displayed separately from the text (if referred to explicitly in the text).

References: All publications cited in the text should be presented in a list of references following the text of the manuscript.

Text: Indicate references by number(s) in square brackets in line with the text. The actual authors can be referred to, but the reference number(s) must always be given.

List: Number the references (numbers in square brackets) in the list in the order in which they appear in the text.

Examples:

Reference to a journal publication:

[1] M.S. Mohsen, B.A. Akash, “Evaluation of domestic solar water heating system in Jordan using analytic hierarchy process”. Energy Conversion & Management, Vol. 38, No. 9, 1997, 1815-1822.

Reference to a book:

[2] Strunk Jr W, White EB. The elements of style. 3rd ed. New York: Macmillan; 1979.

Reference to a conference proceeding:

[3] B. Akash, S. Odeh, S. Nijmeh, “Modeling of solar-assisted double-tube evaporator heat pump system under local climate conditions”. 5th Jordanian International Mechanical Engineering Conference, Amman, Jordan, 2004.

Reference to a chapter in an edited book:

[4] Mettam GR, Adams LB. How to prepare an electronic version of your article. In: Jones BS, Smith RZ, editors. Introduction to the electronic age, New York: E-Publishing Inc; 1999, p. 281-304

Free Online Color: If, together with your accepted article, you submit usable color and black/white figures then the journal will ensure that these figures will appear in color on the journal website electronic version.

Tables: Tables should be numbered consecutively and given suitable captions and each table should begin on a new page. No vertical rules should be used. Tables should not unnecessarily duplicate results presented elsewhere in the manuscript (for example, in graphs). Footnotes to tables should be typed below the table and should be referred to by superscript lowercase letters.

JJMIE
Jordan Journal of Mechanical and Industrial Engineering

EDITORIAL PREFACE

It is my great pleasure to publish the first issue of the Jordan Journal of Mechanical and Industrial Engineering (JJMIE). JJMIE is a refereed, peer reviewed quarterly international journal issued by the Jordanian Ministry of Higher Education and Scientific Research in cooperation with the Hashemite University. The journal covers a wide range of research and development concerning mechanical and industrial engineering. Through the publication, we hope to establish and provide an international platform for information exchange in different fields of mechanical and industrial engineering.

Jordan Journal of Mechanical and Industrial Engineering aims to provide a highly readable and valuable addition to the literature, which will serve as an indispensable reference tool for years to come. The coverage of the journal includes all new theoretical and experimental findings in all aspects of mechanical and industrial engineering or any closely related fields. The journal also encourages the submission of critical review articles covering advances in recent research of such fields as well as technical notes.

The Editorial Board is very committed to build the Journal as one of the leading international journals in mechanical and industrial engineering sciences in the next few years. With the support of the Ministry of Higher Education and Scientific Research and Jordanian Universities, it is expected that a valuable resource to be channeled into the Journal to establish its international reputation.

I have received an excellent response to the first issue of JJMIE from both academics and practitioners. I am pleased by this response and proud to report that JJMIE is achieving its mission of promoting research and applications in mechanical and industrial engineering. In the first issue, there are seven interesting papers dealing with various aspects of mechanical and industrial engineering: (i) a study of the effects of parameters on the surface roughness in the end-milling process; (ii) assessments of power augmentation from gas turbine power plants using different inlet air cooling systems; (iii) a fuzzy monitoring system for an extrusion line; (iv) effect of water depth on the performance evaluation of solar still; (v) a nonlinear torsional dynamic model of multi-mesh gear trains having flexible shafts; (vi) a neural network based real time controller for turning process; and (vii) a graphical design of an input shaping controller for quay-side container cranes with large hoisting: theory and experiments. The methodology employed in these research articles ranges from analytical and empirical models to experimental studies.

JJMIE will bring you top quality research papers from an international body of contributors and a team of distinguished editors from the world's leading institutions engaged in all aspects of mechanical and industrial engineering. Now, the JJMIE invites contributions from the entire international research community. The new journal will continue to deliver up to date research to a wide range of mechanical and industrial engineering professionals. The JJMIE will assure that rapid turnaround and publication of manuscripts will occur within three to six months after submission.

I would like to thank all members of the editorial board and the international advisory board members for their continued support to JJMIE with their highly valuable advice. Additionally, I would like to thank the manuscript reviewers for providing valuable comments and suggestions to the authors that helped greatly in improving the quality of the papers. My sincere appreciation goes to all authors and readers of JJMIE for their excellent support and timely contribution to this journal.

I would be delighted if the JJMIE could deliver valuable and interesting information to the worldwide community of mechanical and industrial engineering. Your cooperation and contribution would be highly appreciated. More information about the JJMIE guidelines for preparing and submitting papers may be obtained from www. jjmie.hu.edu.jo

Prof. Mousa S. Mohsen
Editor-in-Chief
Hashemite University
Zarqa, Jordan

JJMIE
Jordan Journal of Mechanical and Industrial Engineering

PAGES	PAPERS
1 – 6	A Study of the Effects of Machining Parameters on the Surface Roughness in the End-Milling Process *Mohammed T. Hayajneh, Montasser S. Tahat, Joachim Bluhm*
7 – 16	Assessment of Power Augmentation from Gas Turbine Power Plants Using Different Inlet Air Cooling Systems *Q.M. Jaber, J.O. Jaber, M.A. Khawaldah*
17 – 22	A Fuzzy Monitoring System for an Extrusion Line *Mohanad Alata, Wael Masarweh , Said Kamal*
23 – 30	Effect of Water Depth on the Performance Evaluation of Solar Still *Muafag Suleiman K. Tarawneh*
31 – 42	A Nonlinear Torsional Dynamic Model of Multi-Mesh Gear Trains Having Flexible Shafts *Ahmad Al-Shhyab, Ahmet Kahraman*
43 – 56	A Neural Network Based Real Time Controller for Turning Process *Bahaa Ibraheem Kazem, Nihad F. H. Zangana*
57 – 67	A Graphical Design of An Input-Shaping Controller for Quay-Side Container Cranes with Large Hoisting: Theory and Experiments *Ziyad N. Masoud, Mohammed F. Daqaq*

JJMIE

Volume 1, Number 1, Sep. 2007
ISSN 1995-6665
Pages 1 - 5

Jordan Journal of Mechanical and Industrial Engineering

A Study of the Effects of Machining Parameters on the Surface Roughness in the End-Milling Process

Mohammed T. Hayajneh [a,*], Montasser S. Tahat [b], Joachim Bluhm [c]

[a] Industrial Engineering Dep., Faculty of Engineering, Jordan University of Science and Technology, P.O. Box 3030, Irbid-22110, Jordan
[b] Mechanical Engineering Department, Al-Huson Polytechnic, AlBalqa' Applied University, P. O. Box 50, Huson-21510 , Jordan
[c] Institute of Mechanics, University Duisburg-Essen, Campus Essen, 45117 Essen, Universitatsstr. 15, Germany

Abstract

A set of experiments designed to begin the characterization of surface quality for the end-milling process have been performed. The objective of this study is to develop a better understanding of the effects of spindle speed, cutting feed rate and depth of cut on the surface roughness and to build a multiple regression model. Such an understanding can provide insight into the problems of controlling the finish of machined surfaces when the process parameters are adjusted to obtain a certain surface finish. The model, which includes the effect of spindle speed, cutting feed rate and depth of cut, and any two-variable interactions, predicted the surface roughness values with an accuracy of about 12%.

Keywords: Surface Finish; ANOVA; Pareto Chart; Surface Roughness; End milling;

1. Introduction

Metal cutting is one of the most significant manufacturing processes in the area of material removal [1]. Black [2] defined metal cutting as the removal of metal chips from a workpiece in order to obtain a finished product with desired attributes of size, shape, and surface roughness.

The imperative objective of the science of metal cutting is the solution of practical problems associated with the efficient and precise removal of metal from workpiece. It has been recognized that the reliable quantitative predictions of the various technological performance measures, preferably in the form of equations, are essential to develop optimization strategies for selecting cutting conditions in process planning [3-5].

The progress in the development of predictive models, based on cutting theory, has not yet met the objective; the most essential cutting performance measures, such as, tool life, cutting force, roughness of the machined surface, energy consumption, … etc., should be defined using experimental studies. Therefore, further improvement and optimization for the technological and economic performance of machining operations depend on a well-based experimental methodology. Unfortunately, there is a lack of information dealing with test methodology and data evaluation in metal cutting experiments [6].

One may ask a logical question: do we really need to improve the methodology of metal cutting experimental study? The answer to this question is given in the recent CIRP working paper [7] the quote of which is as follows: "A recent survey by a leading tool manufacturer indicates that in the USA the correct cutting tool is selected less than 50% of the time, the tool is used at the rated cutting speed only 58% of the time, and only 38% of the tools are used up to their full tool life capability". The same has been found in an earlier survey of cutting regime selection on CNC machine tools in the American aircraft industry [8] showing that selected cutting speeds are far below the optimal economic speeds.

The demand for high quality and fully automated production focuses attention on the surface condition of the product, especially the roughness of the machined surface, because of its effect on product appearance, function, and reliability. For these reasons it is important to maintain consistent tolerances and surface finish [9]. Also, the quality of the machined surface is useful in diagnosing the stability of the machining process, where a deteriorating surface finish may indicate workpiece material non-homogeneity, progressive tool wear, cutting tool chatter, etc.

The accelerated application of computer aided manufacturing (CAM) to machining by the use of CNC machine tools has focused on developing reliable machinery data systems, to ensure optimum production using expensive equipment. These computerized machinability data systems have been classified into two

* Corresponding author. e-mail: hayajneh@just.edu.jo

general types [10], namely database system and mathematical model system. The database system uses the collection and storage of large quantities of data from experiments, and the mathematical models attempt to predict the optimum conditions [10].

Among several industrial machining processes, milling is a fundamental machining operation. End milling is the most common metal removal operation encountered. It is widely used in a variety of manufacturing industries including the aerospace and automotive sectors, where quality is an important factor in the production of slots and dies. The quality of the surface plays a very important role in the performance of milling as a good-quality milled surface significantly improves fatigue strength, corrosion resistance, and creep life. Surface roughness also affects several functional attributes of parts, such as wearing, heat transmission, ability of holding a lubricant, coating, or resisting fatigue. Therefore, the desired finish surface is usually specified and the appropriate processes are selected to reach the required quality. Several factors influence the final surface roughness in end milling operation [11]. Factors such as spindle speed, feed rate, and depth of cut that control the cutting operation can be setup in advance. However, factors such as tool geometry, tool wear, and chip formation, or the material properties of both tool and workpiece are uncontrolled [12].

One should develop techniques to predict the surface roughness of a product before milling in order to evaluate the robustness of machining parameters such as feed rate or spindle speed for keeping a desired surface roughness and increasing product quality. It is also important that the prediction technique should be accurate and reliable.

Researchers in this area attempt to develop models which can predict surface finish of a metal for a variety of machining conditions such as speed, feed, depth of cut, etc. Reliable models would not only simplify manufacturing process planning and control, but would assist in optimizing machinability of materials. Therefore, the purpose of this study is (1) to study the effect of machining parameters on the surface quality of the machined surfaces, (2) to develop one surface prediction technique which is termed the multiple regression prediction model and (3) to evaluate prediction ability of model.

2. Experimental Setup and Procedure

2.1. Experiment Design

Experiments have been performed in order to investigate the effects of one or more factors of the process parameters (spindle speed, feed rate and depth of cut) on the surface finish of the machined surface. When an experiment involves two or more factors, the factors can affect the response individually or interactally. Often, the experimental design does not give an idea about the interaction effects of the factors as in the case of one factor at-a time experimentation, All possible factor level combinations experiments conducted in completely randomized designs are especially useful for testing the interaction effect of the factors. Completely randomized designs are appropriate when there are no restrictions on the order of the testing to avoid systematic biases error due to the wear of the cutting tool. The procedure to define a model of the process includes the following steps:

1. Selecting the factors to be involved in the process and choosing the levels of these factors.
2. Conducting the experimental at all possible factor level combinations randomly.
3. Analyzing the collected data using parametric analyses of variance (ANOVA).
4. Building the multiple regression model.
5. Validating of the model.

2.2. Experimental Procedure

This experiment employed a Bridgeport end-milling machine. Eight ¾-inch four-flute high-speed steel cutters were used. The experiment has been done under dry machining environment. The experimental setup is shown in figure. 1. The cutting parameters were set as: four levels of spindle speed (750, 1000, 1250, 1500 rpm), seven levels of feed rate (150, 225, 300, 375, 450, 525, 600 mm/min), and three levels of depth of cut (0.25, 0.75, 1.25 mm). The cutters used to execute the experiment were selected randomly. Surface roughness R_a measured in micro-meters was the response variable. Several variables were put under close control including the machine on which milling operation was performed (the same machine was used for all experimental work), and the operator (the same operator machined all specimens). The surface roughness data were collected randomly for each of the 84 machining conditions defined by the levels of independent variables (4 spindle speeds ×7 cutting feeds × 3 depths of cut). The experiment was performed on aluminum workpieces.

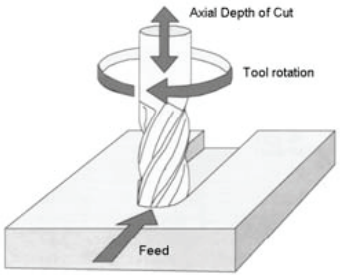

Figure 1: End milling operation

2.3. Building the multiple Regression model

The proposed multiple regression model is a two-way interaction equation:

$$Y = C + B_1X_1 + B_2X_2 + B_3X_3 + B_{12}X_1X_2 + B_{13}X_1X_2 + B_{23}X_2X_3 \quad (1)$$

where

Y: surface roughness in μm

X_1: spindle speed in rpm

X_2: cutting feed in m/min

X_3: depth of cut in mm

In this model, the criterion variable is the surface roughness (R_a) and the predictor variables are spindle speed, feed rate, and depth of cut. Because these variables are controllable machining parameters, they can be used to

predict the surface roughness in milling which will then enhance product quality. A commercial statistical package STATISTICA 6.0 was used to do the regression analysis. In order to judge the accuracy of the multiple regression prediction model, percentage deviation ϕ_i and average percentage deviation $\bar{\phi}$ were used and defined as

$$\phi_i = \frac{|R_{aim} - R_{aip}|}{R_{aim}} \times 100\% \quad (2)$$

where ϕ_i: percentage deviation of single sample data.

R_{aim}: measured R_a .

R_{aip}: predicted R_a generated by a multiple regression equation.

$$\bar{\phi} = \frac{\sum_{i=1}^{n} \phi_i}{n} \quad (3)$$

where $\bar{\phi}$: average percentage deviation of all sample data

n: the size of sample data

This method would test the average percentage deviation of actual R_a (measured by an off-line stylus type profilometer) and predicted R_a (produced by the multiple regression model).

3. Results and Discussion

After 84 specimens were cut for experimental purposes, they were measured off-line with a stylus type profilometer to obtain the roughness average value R_a. All original 84 samples were randomly divided into two data sets, training set and testing set. The training set contained 60 samples which were used to build the model and the testing set contained 24 samples which were used to test the flexibility and the validity of the regression model as shown in Tables 1 and 2, respectively. The collected data were analyzed using parametric analyses of variance (ANOVA) with surface finish as the dependent variable and spindle speed N, Cutting feed F and depth of cut D as independent variables. The ANOVA model was modified to include the main effects of the independent variables and up to two-variable interactions only. The significance level was based on the P-value from ANOVA [13] as

Insignificant if $P > 0.10$

Mildly significant if $0.05 < P < 0.10$

and

Significant if $P < 0.05$ *(4)*

A statistical model was created by regression function in STATISTICA 6.0 from the training data set. The R Square was 0.83879, which showed that 83.879 % of the observed variability in R_a could be explained by the independent variables. The Multiple R was 0.9158, which meant that the correlation coefficient between the observed value of the dependent variable and the predicted value based on the regression model was high.

Table 1 Effect of cutting parameters on the surface finish of the machined surfaces (training data set)

No.	Cutting parameters			R_a,	No.	Cutting parameters			R_a,	No.	Cutting parameters			R_a,
	N	F	D	μm		N	F	D	μm		N	F	D	μm
	rpm	mm/min	mm			rpm	mm/min	mm			rpm	mm/min	mm	
1	750	525	1.25	3.7	21	1500	450	1.25	2.6	41	1000	600	0.75	4.0
2	1250	300	1.25	2.4	22	750	600	0.75	4.5	42	1250	150	1.25	1.7
3	1000	375	0.25	2.6	23	1000	525	0.25	3.8	43	1000	375	0.75	2.6
4	750	600	1.25	4.4	24	750	300	1.25	2.4	44	1250	300	0.75	2.5
5	750	300	0.75	2.6	25	1500	225	0.75	1.9	45	1000	225	0.75	2.4
6	1500	375	1.25	2.5	26	1250	150	0.25	1.2	46	1500	300	0.75	2.1
7	1250	450	1.25	2.3	27	1250	525	1.25	2.5	47	1000	525	0.75	3.9
8	1000	300	1.25	2.3	28	1250	375	1.25	2.5	48	1250	225	0.25	2.1
9	750	150	1.25	1.9	29	1000	225	0.25	2.3	49	1000	150	0.75	1.9
10	1500	600	0.75	2.6	30	1000	450	0.75	3.0	50	1250	375	0.75	2.5
11	1500	450	0.25	3.2	31	1000	600	0.25	4.1	51	1000	150	0.25	1.6
12	1000	450	0.25	4.0	32	1500	150	0.25	1.3	52	1000	225	1.25	2.7
13	750	375	0.75	3.1	33	750	375	1.25	2.6	53	750	225	1.25	2.5
14	1250	600	0.25	3.8	34	1500	525	1.25	3.0	54	1250	450	0.75	2.2
15	1250	225	0.75	2.1	35	1250	300	0.25	2.6	55	1500	300	0.25	2.3
16	1000	150	1.25	1.6	36	1000	300	0.25	3.1	56	750	450	0.25	4.8
17	1000	300	0.75	2.1	37	1500	225	0.25	1.4	56	1250	600	0.75	2.6
18	750	450	1.25	3.3	38	750	225	0.75	2.6	58	750	525	0.25	4.5
19	1500	600	0.25	3.2	39	750	150	0.75	1.7	59	1250	225	1.25	2.4
20	1250	525	0.75	2.5	40	750	525	0.75	4.0	60	1250	150	0.75	1.7

Table 2 Effect of cutting parameters on the surface finish of the machined surfaces (testing data set)

No.	Cutting parameters			R_a,	No.	Cutting parameters			R_a,	No.	Cutting parameters			R_a,
	N	F	D	μm		N	F	D	μm		N	F	D	μm
	rpm	mm/min	mm			rpm	mm/min	mm			rpm	mm/min	mm	
1	1000	450	1.25	2.1	9	1500	450	0.75	2.3	17	1500	525	0.75	2.6
2	1500	150	1.25	1.5	10	750	600	0.25	4.7	18	1500	525	0.25	3.1
3	750	300	0.25	3.0	11	1500	375	0.75	2.1	19	1500	600	1.25	3.2
4	750	450	0.75	3.7	12	750	375	0.25	3.2	20	750	150	0.25	1.6
5	1000	375	1.25	2.6	13	1250	600	1.25	3.1	21	1250	450	0.25	2.5
6	750	225	0.25	2.1	14	1250	375	0.25	2.7	22	1500	150	0.75	1.4
7	1500	375	0.25	2.7	15	1000	600	1.25	2.1	23	1000	525	1.25	1.5
8	1250	525	0.25	3.1	16	1500	300	1.25	2.4	24	1500	225	1.25	1.8

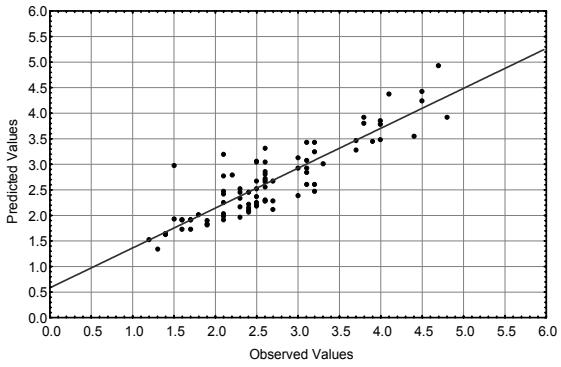

Figure 2:Observed vs. predicted values of surface roughness

In Table 3, the coefficients for the independent variables were listed in the column B. Using these coefficients, the multiple regression equation could be expressed as:

$$R_a = 1.178854 - 0.000492N + 0.009897F - 0.17625D - 0.000003N \times F + 0.000811N \times D - 0.003012F \times D \quad (5)$$

The scatterplot between the observed R_a and the predicted R_a of all 84 samples as shown in Figure 2 indicated that the relationship between the actual R_a and the predicted R_a was linear.

The result of average percentage deviation ($\bar{\phi}$) showed that the training data set (n=60) was 11.645% and the testing data set (n=24) was 12.134%. This means that the statistical model could predict the surface roughness (R_a) with about 88.355% accuracy of the training data set and approximately 87.866% accuracy of the testing data set.

Table 3: included in the multiple regression model (α=0.05)

Factor	Effect (Beta)	Standard error of effect (SE Beta)	Regression Coefficient (B)	P-value
Intercept			1.178854	0.0000*
N	-0.166194	0.173971	-0.000492	0.0000*
F	1.792732	0.242093	0.009897	0.0000*
D	-0.086891	0.258455	-0.176250	0.0002*
N×F	-0.803242	0.258455	-0.000003	0.0017*
N×D	0.507176	0.242093	0.000811	0.0585**
F×D	-0.726007	0.173971	-0.003012	0.0000*

* : Strongly significant
**: Mildly significant

The analysis indicated that all main factors and their interactions were highly significant (P<0.05). The individual effects of various factors as well as their interactions can be discussed from the Pareto chart illustrated by Figure 3. The length of each bar in the Pareto chart is proportional to the absolute value of its associated regression coefficient or estimated effect. The effects of all parameters and interactions terms, are standardized (each effect is divided by its standard error). The order in which the bars are displayed corresponds to the order of the size of the effect. The chart includes a vertical line that corresponds to the 95% limit indicating statistical significance. An effect is, therefore, significant if its corresponding bar crosses this vertical line.

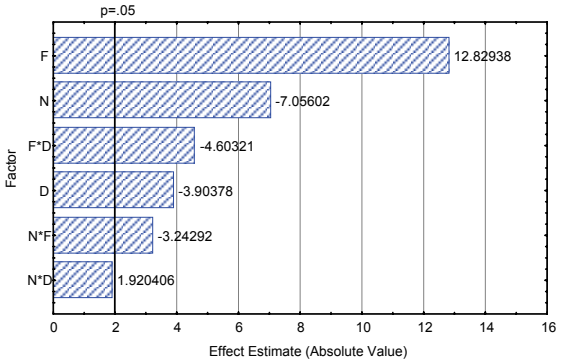

Figure 3: Pareto Chart of Standardized Effects for surface roughness R_a showing significant factors and interactions

The numerical estimates of the effects indicate that the effect of feed is the largest (12.82) and has positive direction. The positive direction means that the surface finish deteriorated with increasing the cutting feed. This is due to the increase in distance between the successive grooves made by the tool during the cutting action, as the cutting feed increases.

Figure 3 shows the effect of spindle speed (-7.05). The negative direction means that increasing the spindle speed improves the surface finish. It is generally well known that an increase in cutting speed improves machineability. This may be due to the continuous reduction in the build up edge formation as the cutting speed increases.

The interaction between the cutting feed and depth of cut significantly affects the surface roughness (-4.6). The interaction also suggests that to get a certain surface finish and maximum metal removal it is preferable to use a high cutting feed associated with depth of cut.

The depth of cut also has negative value (-3.9), which indicates that increasing the depth of cut improves the surface finish. The effect of the depth of cut is less significant on the surface finish.

The interaction between the cutting feed and spindle speed is significantly affecting the surface roughness as shown in Figure 3. The figure shows that increasing the spindle speed improves the surface finish as the cutting feed decreases. This supports the earlier discussion about the effect of decreasing cutting speed on the surface roughness of the machined workpieces.

The interaction between the depth of cut and spindle speed is less significant as shown in Figure 3. The interaction reveals that increasing the spindle speed and increasing the depth of cut deteriorates the surface finish.

4. Conclusions

A series of experiments has been conducted in order to begin to characterize the factors affecting surface roughness for the end-milling process. The effect of spindle speed, feed rate, depth of cut on surface roughness of aluminum samples was studied. The model generated, which includes the effect of spindle speed, feed rate, depth of cut, and the any two-variable interactions, predicts surface roughness reasonably well. The deviation between predicted and measured surface roughness values was within an error band of about 12%. The machining parameters investigated influenced the surface finish of the

machined workpiece significantly. In general, the study shows that cutting feed is by far the most dominant factor of those studied. The most important interactions, that effect surface roughness of machined surfaces, were between the cutting feed and depth of cut, and between cutting feed and spindle speed.

Acknowledgment

Machine shop and the laboratory facilities at Jordan University of Science and Technology and the Deutsche Forschungsgemeinschaft 'DFG, are gratefully acknowledged.

References

[1] J. C Chen and R. A. Smith: Journal of Industrial Technology, vol. 13, No.3, 1997, 15-19.
[2] J. T. Black: Journal of Engineering for Industry, vol. 101, No 4, 1979, 403-415.
[3] P. L. B. Oxley: The Mechanics of Machining An Analytical Approach to Assessing Machinability, Ellins Horwood Ltd., Chichester West Sussex, England, 1989.
[4] E. M. Trent: Metal Cutting, Butterworth-Heinemann Ltd., Oxford. England, 1991.
[5] V. P. Astakhov and M. O Osman: Journal of Materials Processing Technology, vol. 62, No 3, 1996, 175-179.
[6] V. P. Astakhov: Metal Cutting Mechanics, CRC press, 1999.
[7] E. J Armarego: CSME Forum SCGM A Manufacturing Science and Engineering, Hamilton, Canada, 1996, 18-27.
[8] E. J Armarego and R. H. Brown: The Machining of Metals, Prentice Hall, 1969.
[9] N Tabenkin: Carbide and Tool, vol. 21, 1985. 12-15.
[10] P. Balakrishnan and M. F. De Vries: Analysis of Mathematical Model building Techniques Adaptable to Machinability Data Base System, Proceeding of NAMRC-XI, 1983.
[11] G. Boothroyd and W. Knight: Fundamentals of Machining and Machine Tools. Second Edition, Marcel Dekker Inc., New York. 1989.
[12] V. M. Huynh and Y. Fan: The International Journal of Advanced Manufacturing Technology, vol. 7, 1992. 2-10.
[13] J. Neter, W. Wasserman and M. Kutner: Applied Linear Statistical Models, Irwin, Boston, MA, 1990

JJMIE

Volume 1, Number 1, Sep. 2007
ISSN 1995-6665
Pages 7 - 15

Jordan Journal of Mechanical and Industrial Engineering

Assessment of Power Augmentation from Gas Turbine Power Plants Using Different Inlet Air Cooling Systems

Q.M. Jaber [a], J.O. Jaber [a,*], M.A. Khawaldah [b]

[a] Faculty of Engineering Technology, Al-Balqa' Applied University, Amman, Jordan
[b] Directorate of Royal Maintenance Corps, Jordan Armed Forces, Amman, Jordan

Abstract

In this paper, the influence of air cooling intake on the gas turbine performance is presented. A comparison between using different cooling systems, i.e., evaporative and cooling coil, is performed. A computer simulation model for the employed systems is developed in order to evaluate the performance of the studied gas turbine unit, at Marka Power Station, Amman, Jordan. The performance characteristics are examined for a set of actual operational parameters including ambient temperature, relative humidity, turbine inlet temperature, pressure ratio, etc. The obtained results showed that the evaporative cooling system is capable of boosting the power and enhancing the efficiency of the studied gas turbine unit in a way much cheaper than cooling coil system due to its high power consumption required to run the vapor-compression refrigeration unit. Nevertheless, it provides full control on the temperature inlet conditions regardless of the relative humidity ratio.

Keywords: Power augmentation; temperature control; evaporative cooling; cooling coil; gas turbine

Abbreviations

CEGCO	Central Electricity Generation Company
GE	General Electric
GT	Gas Turbine
ISO	International Standard Organizations
PLC	Programmable Logic Controller
SPBP	Simple Payback Period
TET	Turbine exit temperature
TIT	Turbine inlet temperature

Symbols

C_{pa}	Specific heat for air (kJ/kg. °C)
C_{pg}	Specific heat of the flue gas (kJ/kg. °C)
COP	Coefficient of performance of the mechanical chiller
DBP	Design back pressure (kPa)
D_f	Diesel fuel High Heating Value (MJ/kg)
Eff	Evaporative cooling effectiveness
f	Fuel to air mass ratio
h	Specific enthalpy
k	Specific heat ratio
$\dot{m}_a$	Air mass flow rate (kg/s)
$\dot{m}_f$	Fuel mass flow rate (kg/s)
$\dot{m}_{tot}$	Total mass flow rate (kg/s)
$\dot{m}_w$	Water mass flow rate (kg/s)
P_{atm}	Atmospheric pressure (kPa)
P_{base}	Power output in base case (kW)
$\Delta P_{combustion}$	Pressure drop in the combustor (kPa)
ΔP_{intake}	Intake pressure drop (kPa)
Q_{coil}	Cooling load on the coil cooler (kW)
Q_{in}	Heat input to the combustor (kW)
r_p	Pressure ratio
T	Temperature (K)
w	Specific humidity (kg water/kg air)
W_{ac}	Power consumed by the coil cooling (kW)
W_C	Compressor work (kW)
W_{net}	Net power produced (kW)
W_t	Turbine work (kW)
ϕ	Relative humidity
$\eta_{combustion}$	Combustion efficiency
$\eta_{compressor}$	Compressor isentropic efficiency
η_{th}	Thermal efficiency
$\eta_{turbine}$	Turbine isentropic efficiency

* Corresponding author. e-mail: jojaber@yahoo.co.uk

1. Introduction

Gas turbines (GT) have been used for electricity generation in most countries around the world. In the past, their use has been generally limited to generating electricity in periods of peak electricity demand. Gas turbines are ideal for this application as they can be started and stopped quickly enabling them to be brought into service as required to meet energy demand peaks. However, due to availability of natural gas at relatively cheap prices compared to distillate fuels, many countries around the world, e.g. Jordan, use large conventional GTs as base load units, while small ones to meet any shortages in available electricity supplies occurring during an emergency or during the peak load demand periods. Such systems, especially those operating in an open or simple cycle have the disadvantage of being least efficient and so the unit cost of generated electricity is relatively high. For example, in Jordan, gas turbines used as peaking units consumed about $35x10^3$ tonnes of diesel fuel, but supplied less than 111 GWh, i.e, 1.3% of electricity generated in 2005 [1]. The average efficiency of GT peaking plants in Jordan over the last five years was in the range of 20-28% [2,3]. Such low efficiencies can be attributed to many reasons, such as, operation mode, poor maintenance, engine size and age. Unit cost of produced electricity and gaseous emissions that would otherwise arises from conventional generators could be reduced by employing a hybrid system that uses a renewable energy source, such as, solar energy [4-6], or by using advanced technologies, such as, regenerative cycle, combined cycle and power augmentation. The latter is achieved by cooling the air at the compressor intake which helps increasing the density of air flowing into the GT plant and thereby increasing the generated power from the engine.

Different geographical regions have different climatic conditions, i.e, ambient temperature and relative humidity ratio. For example, the weather in deserts (hot and dry) is different from that of coastal regions in which humidity is very high. In Jordan, during the summer season, the ambient temperature may reach as high as 37 °C, or even higher in July and August when peak demand occurred due to increasing demand on electrical energy for air-conditioning and ventilation systems. The ambient temperature has a strong influence on the gas turbine performance [7,8]. Generally, unlike the heat rate, the net power output form a gas turbine decreases with the increase of the ambient air temperature. This is due to reduced net power output, which is directly proportional to the air mass flow rate; net power produced decreases when the ambient air temperature increases. Practically, a 25% loss of the rated power capacity of the gas turbine at ISO conditions as the ambient temperature reaches 40 °C is reported [9]. On the other hand, during summer the demand for electrical energy rises up. Therefore, it is necessary to enhance GT power output, which can be achieved through cooling the air just before it enters the gas turbine's compressor. There are two main ways that may be used to cool the inlet air: these include (i) evaporative or fog cooling; and (ii) mechanical cooling and thermal storage. Mechanical cooling may be coil cooling system or absorption chiller cooling [10, 11, 12, 13]. Such techniques can boost the power out by about 30%, when supplying the inlet air temperature at approximately 10 °C.

In related open literature, many researchers studied different cooling methods to enhance the performance of GT plants operating at high conditions of ambient temperature. Johnson [14] presented a discussion of the theory and operation of evaporative coolers for industrial gas turbine installations. Calculations of parameters to predict the performance of evaporative cooler were discussed, in addition to installation, operation, feed water quality and the causes and prevention of water carry-over. Ondryas et al., [15] investigated the impact of using chillers at the air intake to boost gas turbines power in cogeneration plants during high ambient temperatures. Three types of chillers i.e, absorption, vapour-compression and thermal energy storage were studied. Motive energy for the chillers is steam from the GT exhaust for the absorption system and electricity for vapour-compression chillers. Description of the chilled water distribution in the inlet air system was provided and the overall economics of the power augmentation benefits was investigated. It had been reported that air chilling could be effectively used to boost power during high temperatures and the benefit from peak power production could outweigh the needed investment. In another paper by Mercer [16], it was reported that chillers utilizing thermal storage systems would increase the GT power output by 25% during peak periods. Evaporative coolers, on the other hand, give an increase of about 10-15%. Water fogging is another cooling method, which would enhance power out put by 10% to 20% [8, 10]. It was reported by researchers and published information by manufactures of such systems that a gain of 1% in the power output is attainable for every 1.5-2.0 °C drop in the inlet air temperature using water chillers. The performance of the gas turbine using an intake cooler for time varying annual climatic conditions had also been evaluated [17]. Using an evaporative cooler enhanced the plant output by 2-3%, while chilled water coolers would increase the power output by 5-7%, depending on the climatic conditions. Kolp et al., [18] presented an analysis for the effect of various forms of inlet air heating, cooling and supercharging on a 40 MW GE LM6000 gas turbine. It was found that reduction by 28 °C of inlet air temperature would increase power out put by about 30% and reduce the heat rate by approximately 4.5%. De Paepe and Dick [19] presented a technological and economical analysis of different types of condensers for water recovery in steam injected GT. It was shown that injecting steam into the cycle increases its power output and efficiency at relatively low capital costs, i.e. short pay back periods varies from 1.5 to 9.5 years depending on employed system and desired configuration. However, the high rate of water consumption is the major drawback of such systems.

In this paper, the influence of air cooling at the intake of the compressor on the performance of an actual GT engine operating at Marka Power Plant, East of Amman, has been theoretically investigated using prevailed climatic conditions during 2005 [20]. The effect of two air cooling methods, i.e, evaporative and coil cooling systems, were examined. Each of the studied two coolers modifies air temperature and humidity differently and each system has different cooling capacity that would limit the minimum

attainable temperature at the compressor inlet. It is not the aim of this paper to discuss other issues related to off-design operation, compressor or turbine design and cooling systems; rather to provide guidance information concerning the proposed cooling systems to deduce so that its overall performance can be compared with the base-case conditions without inlet air-cooling.

2. Theory and performance modelling

In their continuous planning for load growth, electricity utilities search for the most economic generation schemes. But this will be subject to a number of constraints, such as, the type of fuel available, peak-to-base demand ratio and compliance with national environmental standards. To assess the behaviour of a power plant over its expected ranges of operation, appropriate mathematical models which can predict the performance under both design-point and off-design or part-load operating conditions have been developed. In this investigation, the performance analysis of two air cooling systems is discussed and compared with the base-case scenario without inlet air cooling. For the two cooling systems, the main operating variable is the intake temperature at the inlet of compressor, while TIT and TET remain invariant. Figure 1 shows a simple sketch of the studied GT engine. The gas turbine engine consists of a compressor, a combustor and a turbine, in addition to a cooling system. Two types of air cooling systems, i.e., evaporative and cooling coil, are investigated in this study. The evaporative cooling system is taken as water spraying, modelled as an adiabatic saturator, and the used cooling coil resembles a typical refrigeration cycle. The performance of the power plant is examined with each air cooler.

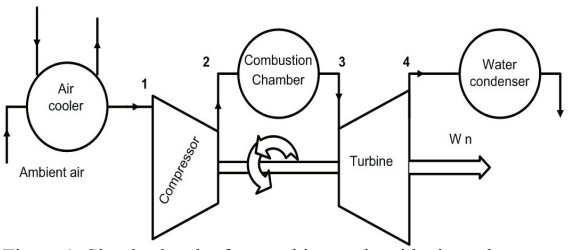

Figure 1: Simple sketch of gas turbine cycle with air cooler

The thermal power analysis of the GT plant is performed taking into consideration the compressor and turbine efficiencies., effectiveness of evaporative cooling unit and coefficient of performance of mechanical chillers. Pressure losses in the compressor intake and combustor and turbine exhaust ducts are also considered as well as the variations of the specific heats of air and combustion products. These calculations were carried out by means of a specially designed computer programme. This model is based also on energy and flow matching of the turbomachinery components, i.e., the components are aerodynamically coupled along the flow satisfying mass continuity. They are coupled by the engine shaft, so energy balance exists. The working fluid passing through the compressor is assumed to be an ideal mixture of air and water vapour, while that passing through the turbine is assumed to be an ideal mixture of combustion gases and all of which are assumed to behave as ideal gases. The main points of calculation procedure for the proposed system, reference to Figure 1, in are presented below.

3. Air Cooling Systems

The water spraying cooler is modelled as an adiabatic saturator that delivers air to the compressor with about 100% relative humidity, i.e., saturated air. The air temperature drops to the wet bulb temperature as a result of passing through the water spraying cooler. The air exit temperature is dictated by both the ambient air temperature and relative humidity. A simple sketch of the spray cooler and control system is shown in Figure 2a.

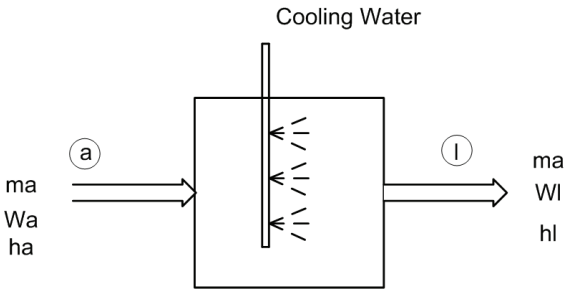

(a) Sketch of evaporative cooling system

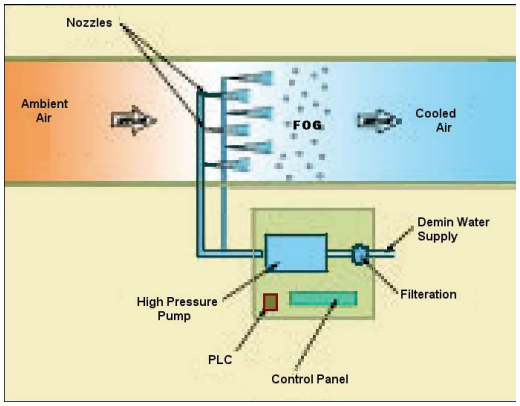

(b) PLC control of the evaporative cooling system

Figure 2: Cooling system

A typical evaporative cooling system consists of a series of high pressure pumps that are mounted on a skid, PLC based control system with temperature and humidity sensors, and an array of fog nozzles installed in the inlet air duct as shown in Figure 2b. Sensors are provided to measure relative humidity and dry bulb temperature. Special programming codes use these measured parameters to compute the ambient wet bulb temperature and the wet bulb depression, i.e. the difference between the dry bulb temperature and the wet bulb temperature. They quantify and control the amount of evaporative cooling that is possible with the ambient conditions. The system turns on or off fog cooling stages to match the ability of the ambient conditions to absorb water vapour. The control system also monitors pump skid operating parameters, such as, water flow rates and operating pressure, and provides alarms when these parameters are outside acceptable ranges.

Ambient air enters the cooler at T_a and ϕ_a. Adding an adequate quantity of water to air stream in the spray cooler raises the air moisture content and decreases its temperature. If the spray cooler is assumed large and insulated, then such cooler resembles the classical adiabatic saturation process. Analysis of this process is available in the thermal engineering literature. Applying mass and energy balances to the cooling system yields:

$$C_{pa}(T_1 - T_a) = \omega_1 h_{fg1} + \omega_a (h_{ga} - h_{l1}) \quad (1)$$

Where ω_a and ω_1 are the humidity ratios, i.e. the ratio of the mass of water vapour to the mass of air, before and after the cooler, respectively. In general, ω is related to the water vapour pressure at saturation temperature. A simple sketch of the coil cooling is shown in Figure 3. This air cooler operates in a different way than the water spray cooler; however, the temperature and relative humidity of fluid leaving the cooler depend on the coil temperature and relative humidity of ambient air. Ambient air enters the coil cooling at T_a and ϕ_a. Air passing over the outer surface of the coil experiences a drop in temperature and possibly a decrease in specific humidity, ω. The coil temperature can be adjusted to allow air to reach a certain desired temperature. In this case, the cooling load to be removed using cooling coil can be estimated; hence, the power input to the associated refrigeration system can also be evaluated.

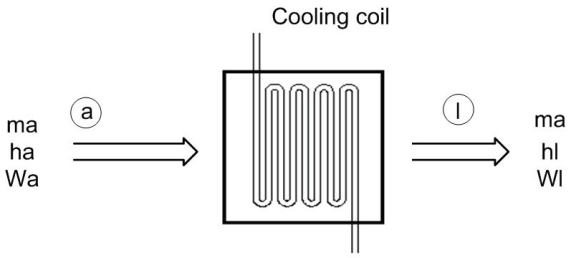

Figure 3: A Typical cooling coil

The cooling load (Q) removed from the air flowing at ambient conditions into the power plant can be estimated using the first law of thermodynamics as follows:

$$Q_{coil} = \dot{m}_a C_{pa}(T_1 - T_a) \quad (2)$$

Where C_{pa} is the specific heat of the dry air at constant pressure, and T_1 is the temperature at the compressor inlet which should not be lower than 5°C in order to avoid condensation and freezing conditions. Assuming that this load is removed using a typical refrigeration machine having a fixed coefficient of performance, the power needed to operate such machine is estimated from the following relation:

$$W_{ac} = \frac{Q_{coil}}{COP} \quad (3)$$

Where COP is the coefficient of performance of the cooling coil of the employed chiller. Then, the output net power of gas turbine will be reduced as follows:

$$W_{net} = (W_t - W_c) - W_{ac} \quad (4)$$

4. Gas turbine unit

In this study, the selected actual engine, GT 6001 B (PG 6541-B) from General Electric Power Systems, with a nominal rating of 20 MW_e, is an open cycle and a single-shaft gas turbine. This engine is owned and operated, at present as a standby and a peaking unit at Marka Power Station in Jordan, by CEGCO and firing diesel fuel. In order to undertake a design-point analysis for the chosen GT engine, a set of available practical data were used, as summarized in Table 1. Such data were taken from the technical manuals of CEGCO and GE [21, 22]. However, a standard gas turbine cycle is considered for the present analysis in order to make it easier for results comparison.

Table 1: Technical specification of selected gas turbine engine

Power plant	Marka Power Station
General electric model	PG5341
Site	Marka, Amman East
Cycle	Single shaft, simple cycle, industrial engine
Pressure ratio	12
Inlet pressure	93 kPa
Air flow rate	70 kg/s
Power output	20 MW
Altitude	735 m
Compressor	Stages: 17 Speed: 5100 rpm Type: axial flow, heavy duty
Turbine	Stages: 2 Speed: 5100 rpm
Inlet turbine temperature	1350 K
Fuel	Light distillate fuel (Diesel)

4.1. Compressor

The intake pressure drop (ΔP_{intake}) is taken to be 1 kPa, the intake temperature is the same as the ambient temperature in the base-case scenario, specific heat ratio for air $\kappa_a = 1.4$, and specific heat for air $C_{pa} = 1.005$ kJ/kg.°C. For a pressure ratio r_p, the pressure of the fluid leaving the compressor can be determined from the following equation:

$$P_2 = r_P P_1 \quad (5)$$

Where inlet pressure entering the compressor is $P_1 = P_{atm} - \Delta P_{intake}$

The compressor isentropic efficiency can be evaluated using the following empirical equation:

$$\eta_{compressor} = 1 - \frac{[0.09 + (r_p - 1)]}{300} = 0.87 \quad (6)$$

The isentropic outlet temperature leaving the compressor is determined from the following equation:

$$T_{2s} = T_1 (r_p)^{\frac{k_a - 1}{k_a}} \quad (7)$$

The isentropic temperature rise is determined from the following equation:

$$T_{sr} = T_{2s} - T_1 \quad (8)$$

The actual temperature rise in the compressor is calculated from the definition of isentropic efficiency:

$$T_{ar} = \frac{T_{sr}}{\eta_s} \quad (9)$$

Then, the actual outlet temperature leaving the compressor is:

$$T_{2a} = T_1 + T_{ar} \quad (10)$$

The actual work consumed by the compressor is given by:

$$W_c = \dot{m}_a C_{pa} T_{ar} \quad (11)$$

4.2. Combustor

At a specific heat of the flue gas $C_{pg} = 1.15$ kJ/kg.°C, outlet temperature from the combustor T_3, combustion efficiency assumed to be $\eta_{combustion} = 0.99$, and a pressure drop ($\Delta P_{combustion}$) in the combustor assumed to be 48 kPa, then, outlet pressure from the combustor is determined from the following equation:

$$P_3 = P_2 - \Delta P_{combustion} \quad (12)$$

Fuel mass flow rate is determined from the following equation:

$$\dot{m}_f = \frac{q_{in}/D_f}{\eta_{combustion}} \quad (13)$$

Where diesel fuel high heating value is assumed to be around 42 MJ/kg and fuel/air ratio (f) is determined from the following equation:

$$f = \frac{\dot{m}_f}{\dot{m}_a} \quad (14)$$

Then, heat input to the combustor can be estimated from energy balance across the combustor:

$$Q_{in} = \dot{m}_a C_{pg} (T_3 - T_{2a}) \quad (15)$$

4.3. Turbine

The power produced by the turbine is determined assuming a specific heat ratio of exhaust gas $k_g = 1.332$, invariable turbine inlet temperature T_3, inlet pressure P_3, and design back pressure $DBP = 1$ kPa. The turbine isentropic efficiency can be evaluated using following empirical equation:

$$\eta_{turbine} = 0.9 - \frac{[(T_3/P_4) - 1]}{250} = 0.86 \quad (16)$$

Outlet pressure at the turbine's exit is:

$$P_4 = P_{atm} + DBP \quad (17)$$

The expansion ratio is determined from the following equation:

$$r_{p_1} = \frac{P_4}{P_3} \quad (18)$$

The isentropic outlet temperature leaving the turbine is determined from the following equation:

$$T_{4s} = T_3 (r_{p1})^{\frac{k_g - 1}{k_g}} \quad (19)$$

The isentropic temperature drop is determined from the following equation:

$$\Delta T_{4s} = T_3 - T_{4s} \quad (20)$$

The actual temperature drop is obtained from the definition of turbine's isentropic efficiency:

$$\Delta T_{4a} = T_{4S} \eta_{turbine} \quad (21)$$

The actual outlet temperature leaving the turbine is determined from the following equation:

$$T_{4a} = T_3 - \Delta T_{4a} \quad (22)$$

The total mass flow rate is given by:

$$\dot{m}_{tot} = \dot{m}_a + \dot{m}_f \quad (23)$$

The work produced from the turbine is determined by the following equation:

$$W_t = \dot{m}_{tot} C_{pg} T_{4a} \quad (24)$$

The power output obtained from the gas turbine power plant is:

$$W_{net} = W_t - W_c \quad (25)$$

The thermal efficiency without cooling intake air before being introduced to the gas turbine unit is:

$$\eta_{th} = \frac{W_{net}}{q_{in}} \quad (26)$$

5. Results and analysis

In order to establish a systematic comparison between the effects of the two coolers, the performance of the gas turbine unit is examined for a restricted set of operational and design conditions of an operating GT unit from CEGCO, taking into account real climatic circumstances prevailed during 2005 at Marka, east of Amman, Jordan. The power plant performance characterized by the plant efficiency and net power output, as well as water mass flow rate in the case of evaporative cooling, are estimated based on actual values of given variables, i.e. temperature, relative humidity and gas turbine engine characteristics. The analysis is restricted to the design point performance of GT engine and off-design operation is not considered in this study.

Figure 4 shows the effect of ambient temperature on power output and thermal efficiency of the gas turbine power plant in the standard case.

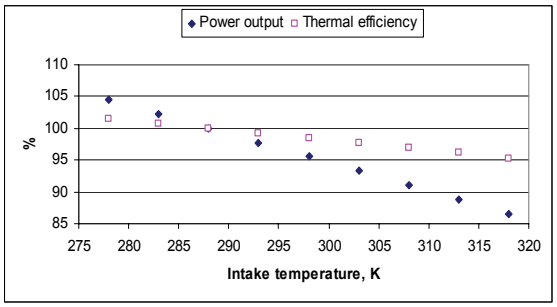

Figure 4: Thermal efficiency and power output versus intake temperature

As can be seen, thermal efficiency decreases as the inlet air temperature increases, where the drop in efficiency is significant at higher temperatures. It is clear that efficiency and power output are inversely related with intake air temperature; higher ambient temperature will result in reduced power output and, consequently, the plant's thermal efficiency shrinks. But it should be noted that temperatures of less than about 5 °C should not be allowed in the intake system in order to avoid difficulties arising from icing. Computed power output and efficiency with varying days of the year are shown in Figures 5 and 6 respectively.

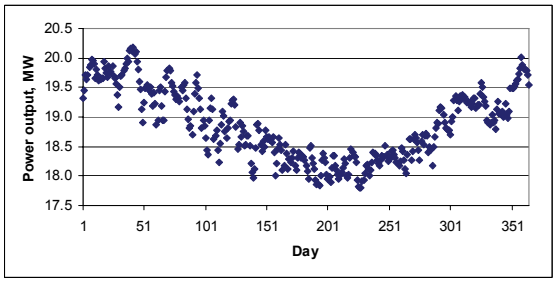

Figure 5: Power output versus day of the year

As expected, the higher the ambient temperature is the lower rate of generated power from the GT unit gets. Unfortunately, the minimum produced power is during the summer season, May-October This id (days 150-300), when peak demand occurred in Jordan. due to the increasing demand on electrical energy for air-conditioning and ventilation systems. Such case would make it more difficult for electricity providers to match the increasing demands during hot and dry summer. Thus, simple and cost-effective measures should be taken in order to meet consumers' needs. In this study, the basic assumption is that the effectiveness of the evaporative cooling system will be around 80%, which is reasonable for such large systems. According to weather data provided by the Meteorological Department, in Jordan, the average ambient temperature during hot days may exceed 35 °C with a low relative humidity ratio of about 30%. Such conditions are favourable for evaporative cooling systems. In such case, the inlet air temperature can be decreased by approximately 10-15°C to reach a wet bulb temperature of about 20-25 °C.

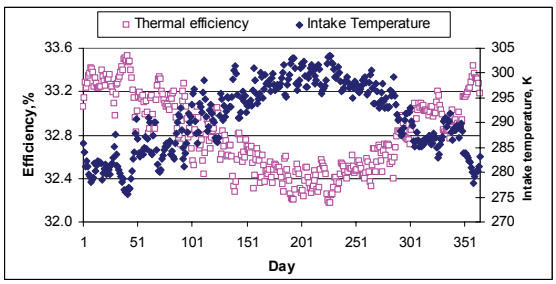

Figure 6: Thermal efficiency and intake temperature versus day of the year

The calculated thermal efficiency of the employed gas turbine engine versus the day of the year is shown in Figure 7. It is obvious that the efficiency during summer is lower than that incurred during winter, but there was a slight increase of around 1% in the obtained efficiency when compared with the results of the base case scenario for same GT engine. Increasing the effectiveness of the evaporative cooler by 10% to reach 90% would result in a slight increase in the produced power and final thermal efficiency.

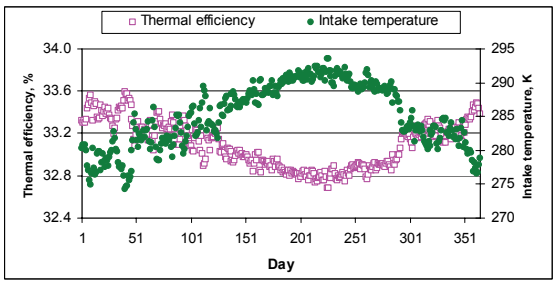

Figure 7: Thermal efficiency and intake temperature versus day of the year

Higher intake temperatures will lead to deterioration in the power output and thermal efficiency of the studied engine, which can be ratified by the increased work of compressor due to the fact that air viscosity is proportional to temperature. Thus, compressor consumes more effort to provide the same pressure rise; hence the net out put is reduced. Another important reason behind the increased power, in addition to decreasing the temperature of intake air, is the higher rates of mass flow across the engine because of added water. It is estimated that mass flow rate of water in the evaporative cooling system will range between 0.3-0.5 kg/s, i.e., less than 0.7% of the air mass flow rate. That is enough to bring the incoming air to near saturation conditions depending on climatic conditions on that particular day or time –see Fig. 8.

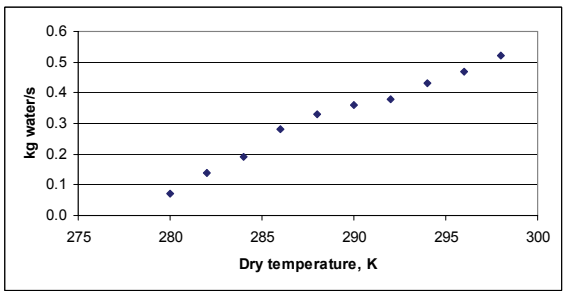

Figure 8: Water mass flow rate versus dry temperature

In the case a more effective evaporating cooling system, with effectiveness of 90% is used the water flow rate may reach an average of about 0.6 kg/s and the resultant net increase in the power out put is estimated to be around 1 MW, i.e., 5% of the rated power of the studied engine. However, it should be noted an that the function of evaporating cooling system is cooling the air by humidifying it, which is an adiabatic process. Thus, water flow rate will follow not only the dry bulb temperature, but more importantly, the relative humidity on a particular time. Thence, higher relative humidity ratios would result in lower amounts of water to reach saturation conditions, i.e., wet bulb temperature which is constant during the cooling process.

The second simulated method is the cooling coil, i.e., employing a mechanical chiller, to pre-cool air intake. It is found that it will be possible to decrease intake air temperature by about 20 °C or even more if needed during hot summer days regardless of the relative humidity ratio. Figure 9 shows the effect of using cooling coil on the temperature of the intake air; and Figure 10 illustrates the net efficiency of the gas turbine power plant on each day of the year. As mentioned earlier, lower efficiencies often incurred during summer, which makes it an attractive option to augment power by employing chillers or other means for air pre-cooling.

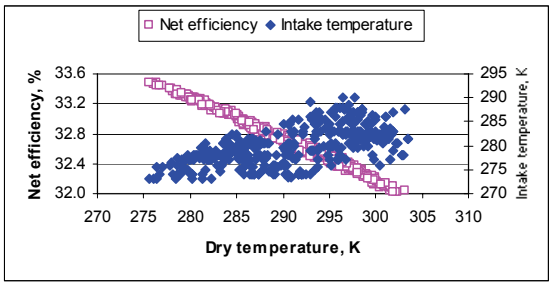

Figure 9: Net efficiency and intake temperature versus dry temperature

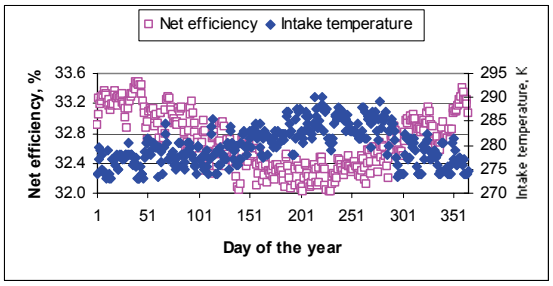

Figure 10: Net efficiency and intake temperature versus day

An actual increase in the net power produced from the plant is recorded by about 0.5-1 MW over that calculated in the base case scenario under similar operating conditions and assumed coefficient of performance (COP) of the chiller system equals two. The exact value is dependent on ambient temperature and COP of the employed chiller. For a higher COP, the augmented power and net power produced from the plant will be increased – see Figures 11 and 12. It can be seen from these figures that the effect of COP is significant at high ambient temperatures.

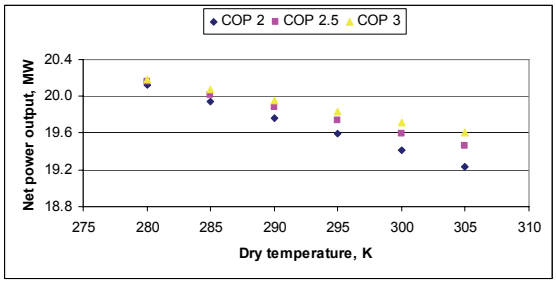

Figure 11: Net Power output versus air dry temperature for different COP

This is because a chiller with high COP will consume less energy to produce the same cooling effect, and consequently the plant's net efficiency is higher. Similar results were reported by independent researchers from different countries but not for Jordan [8,12-15,23]. Nevertheless, it is interesting to note when air temperature in the intake system is reduced, the net power output will be reduced as well, due to the fact that the employed chiller will consume more energy to bring the temperature down to the desired level.

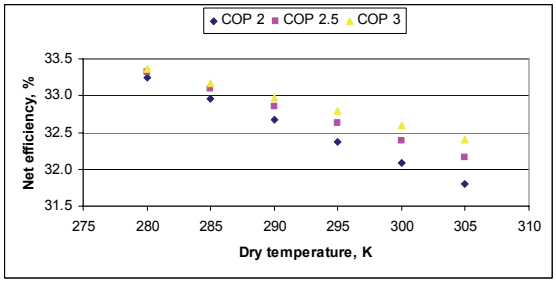

Figure 12: Net efficiency versus air dry temperature for different COP

The computed results of the different operating scenarios revealed that the net power output from the gas turbine plant varied significantly when intake air was cooled down as compared with the base case without cooling – see Fig. 13. It is obvious that there is a slight difference between the employed two cooling systems, but the basic issue here is the augmented power from the gas turbine plant as a direct result of reducing air temperature at the compressor intake.

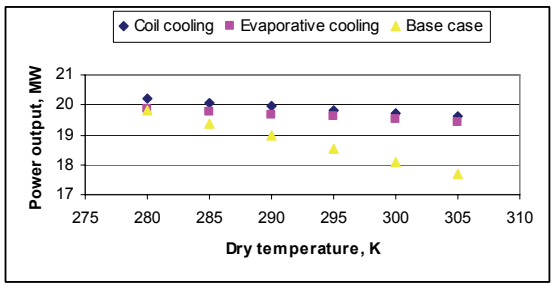

Figure 13: Estimated power output of different cooling systems (effectiveness of evaporative system is 0.8 & COP of chiller is 3)

Assuming an average dry bulb temperature of about 32 °C, and a temperature drop of about 10 and 13 °C when evaporative and coil cooling systems were used, then the augmented power would be around 1 and 1.5 MW, respectively.

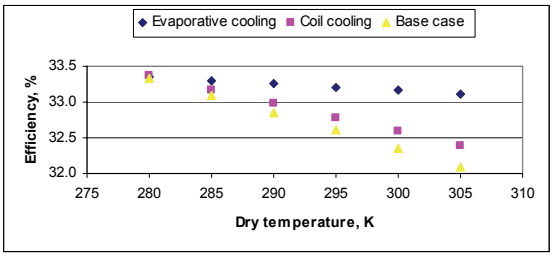

Figure 14: Predicted thermal efficiency of employed cooling systems (effectiveness of evaporative system is 0.8 and COP of chiller is 3)

This finding represents an improvement of about 5-7%, which is in full agreement with published work done elsewhere [8,12-15,23]. In terms of thermal efficiency, the evaporative cooling system is more efficient than coil cooling system as can be seen in Fig. 14. This can be attributed to the fact that in case of coil cooling system some of the generated power will be needed to run the refrigeration cycle, thus, the final efficiency of the gas turbine power plant drops slightly. But in the evaporative cooling system de-mineralized water is needed, instead of electricity to cool down the incoming air into the gas turbine, which is scarcely available in Jordan. This represents an important issue that should be taken into consideration when selecting most appropriate cooling system for particular power plant and location in Jordan or elsewhere. In the future, it is highly advisable to extend this study to include absorption cooling and thermal storage systems.

The expected annual net revenues resulting directly from excess power generation, in this study, is significant. To predict economics of such systems, a detailed cost-benefit analysis should be carried out. But at this stage, it is very difficult to estimate the required capital investment for such cooling systems due to many reasons. The most important is the size of the system and the actual site conditions. However, based on available published data in the open literature, it has been estimated that an approximate cost of simple evaporative cooling system is about 7-10 JD or 10-15 US$ per kW installed. This brings the total cost of the evaporative cooling system of between 140,000–200,000 JD. While, the approximate cost of industrial cooling coil system is about 700-1000 JD/ton Ref or 1000-1500 US$/ton Ref installed. This brings the total cost of the required chiller of between 400,000–575,000 JD. However, such capital costs are much cheaper than that required to install a new gas turbine unit with an average specific investment of about 300-500 US$ per kW [24].

Based on the previous analysis and calculated annual revenues, the predicted SPBP would be around 2 and 5 years for evaporative and cooling coil systems, respectively. A higher capital cost will lead to longer recovery periods; however, doubling the initial cost will increase the payback period by one year approximately. But it should be hated that higher temperatures will result in shorter payback periods. The obtained SPBP is considered very short from economic point of view and highly attractive for investments in such projects, especially when evaporative cooling system is considered.

To sum up, it can be said that using intake air cooling technologies for gas turbine power plants is an attractive option to increase power output and efficiency of these plants. Therefore, it is a main recommendation of this study for concerned governmental institutions and power generation companies to conduct detailed and specific studies for all gas turbine power plants in the Jordan in order to evaluate the precise costs and benefits of different cooling systems. Hence, the most appropriate cooling system can be selected and installed soon.

6. Conclusions

This article presents a detailed technical assessment for two cooling methods to cool the intake air before being introduced into the compressor. Although the performance of evaporative coolers is highly dependent on ambient temperature and humidity, they do operate efficiently during dry and hot climatic conditions such those prevailed in Jordan during summer. The obtained results shows that the evaporative cooling system appears to be capable of boosting generated power by about 5% and enhancing efficiency of the selected gas turbine unit in a way that is less expansive than a cooling coil. But providing needed water for the operation of such coolers may be a challenge in some regions, in Jordan.

Cooling coil gives a full control of the compressor inlet conditions regardless of ambient conditions; however, it demands a quite large operational power. During hot and dry conditions, the net power output produced from the GT unit increases by about 1.0-1.5 MW when cooling system is used over that calculated in the base case under similar operating conditions. The coil cooling increases the efficiency of the power plant by about 1 % or more depending on the operating conditions and the selected chiller system, because the power extracted for refrigeration must be included. Extracting this power from the gas turbine output reduces the overall plant performance, i.e., large deterioration in the efficiency occurs at high temperature due to the increasing cooling load. For a higher COP, the augmented power and hence net power, produced from the plant will be increased. Other means, such as, absorption cooling system is expected to yield more power since energy required to run the absorption cycle is taken freely from the turbine's exhaust but at a higher capital cost.

References

[1] CEGCO, Central Electricity Generating Co., 2000-2006, Annual reports 1999-2005, Amman, Jordan.

[2] J.O. Jaber, M.S. Mohsen, S.D. Probert, M. Alees, "Future Electricity Demands and Greenhouse Gas Emissions in Jordan". Applied Energy, Vol. 69, 2001, 1-18.

[3] J.O. Jaber, "Greenhouse Gas Emissions and Barriers to Implementation in the Jordanian Energy Sector". Energy Policy, Vol. 30, 2002, 385-395.

[4] J.O. Jaber, S.D. Odeh, S.D. Probert, "Integrated PV and gas turbine system for satisfying peak-demands". Applied Energy, Vol. 76, 2003, 305-319.

[5] J.O. Jaber, O.O. Badran, N. Abu-Shikhah, "Sustainable energy and environmental impact: role of renewables as clean and secure source of energy for the 21st century in Jordan". Clean Technologies and Environment Policy, Vol. 6, 2004, 174-186.

[6] J.O. Jaber, A. Al-Sarkhi, B. Akash, M. Mohsen, "Medium-range planning economics of future electrical power generation". Energy Policy, Vol. 32, 2004, 357-366.

[7] Y.S.H. Najjar, "Enhancement of Performance of the Gas Turbine Engines by Inlet Air Cooling and Cogeneration System". Applied Thermal Engineering, Vol. 16, 1996, 163-173.

[8] M.M. Alhazmy, Y.S.H. Najjar, "Augmentation of Gas Turbine Performance Using Air Coolers". Applied Thermal Engineering, Vol. 24, 2004, 415-429.

[9] Amell, F.J. Cadavid, "Influence of the Relative Humidity on the Air Cooling Thermal Load in Gas Turbine Power Plant". Applied Thermal Engineering, Vol. 22, 2002, 1529-1533.

[10] Mohanty, J. Paloso, "Enhancing Gas Turbine Performance by Intake Air Cooling Using an Absorption Chiller". Heat Recovery Systems, Vol. 15, 1995, 41-50.

[11] J.S. Andreppont, "Combustion Turbine Inlet Air Cooling, Benefits, Technology Options and Applications for District Energy". International District Energy Association (IDEA) 91st Annual Conference, Montreal, 2000.

[12] M. Ameri, K. Montaser, "The Study of Capacity Enhancement of a 37.5 MW Gas Turbine Using Chilled Water Thermal Energy Storage System". Proceedings of the 15th International Conference of Efficiency Costs, Optimization, Simulation and Environmental Impact of Energy Systems (ECOS, 2002), Berlin, Germany, 2002.

[13] M. Ameri, H. Nabati, A. Keshtgar, "Gas Turbine Power Augmentation Using Fog Inlet Air-cooling System". Proceedings of ESDA04, 7th Biennial Conference on Engineering Systems Design and Analysis, Manchester, United Kingdom, 2004.

[14] R.S. Johanson, "The Theory and Operation of Evaporative Coolers for Industrial Gas Turbine Installations". Gas Turbine and Aeroengine Congress and Exposition, June 5-9, Amsterdam, The Netherlands, Paper No. 88-GT-41, 1988.

[15] I.S. Ondryas, D.A. Wilson, M. Kawamoto, G.L. Haub, "Options in Gas Turbine Power Augmentation Using Inlet Air Chilling". Engineering for Gas Turbine and Power, Transaction of the ASME, Vol. 113, 1991, 203-211.

[16] M. Mercer, "One-Stop Shop for Inlet Cooling Systems". Diesel and Gas Turbine Worldwide, June Issue, 2002, 10-13.

[17] A.M. Bassily, "Effects of Evaporative Inlet and After-cooling on the Recuperated Gas Turbine Cycle". Applied Thermal Engineering, Vol. 21, 2001, 1875-1890.

[18] D.A. Kolp, W.M. Flye, H.A. Guidotti, "Advantages of Air Conditioning and Supercharging an LM6000 Gas Turbine Inlet". Engineering for Gas Turbine and Power, Transactions of the ASME, Vol. 117, 1995, 513-527.

[19] M. De Paepe, E. Dick, "Technological and Economical Analysis of Water Recovery in Steam Injected Gas Turbines". Applied Thermal Engineering, Vol. 21, 2001, 135-156.

[20] Meteorological Department, Amman Civil Airport, Jordan Annual Climate Bulletin 2005, Amman, Jordan.

[21] CEGCO, Central Electricity Generating Co., 2001, Performance of Gas Turbines, Report by the Planning Development Department, Amman, Jordan.

[22] GE, General Electric Service, 2002, http://www.ge.com.

[23] H. Al-Madani, "Gas Turbine Performance Enhancement by Intake Air Cooling". Int. J. Exergy, Vol. 3, 2006, 164-173.

[24] Annual Gas Turbine Handbook, Jan-Feb 2006, Gas Turbine World, Pequot Publishing Inc, CT, USA.

JJMIE

Volume 1, Number 1, Sep. 2007
ISSN 1995-6665
Pages 17 - 21

Jordan Journal of Mechanical and Industrial Engineering

A Fuzzy Monitoring System for an Extrusion Line

Mohanad Alata [a,*], Wael Masarweh [b], Said Kamal [b]

[a] Mechanical Eng. Dept., Jordan University of Science and Technology, P.O. Box 3030, Irbid-Jordan
[b] Nuqul Group, Amman- Jordan

Abstract

A monitoring system of an extrusion line was developed. Three main hydraulic pumps support the extrusion line in MODAL. Data of energy consumption was collected from the power supply of these main pumps. Clip-meters were attached to the supply wires in order to get the amount of the energy consumed; one reading is recorded every 5 seconds by a PC where the data is saved. The signatures of the billets extruded were studied to understand the signature behavior. Max-Min boundaries were found and a fuzzy system that makes use of the boundaries was built to indicate the unusual situations. The real on-line output is crisp and not fuzzy. It can be an alarm, a buzzer, a stop etc. The output is designed to give an approximate description of the situation in term of a percentage. The proposed system worked well in defining the real situation of the extruder. For future work, some recommendations were presented.

1. Introduction

1.1. Extrusion Process

Extrusion is one of the most popular metals forming processes used nowadays. The extrusion process involves forcing a billet, which is enclosed in a container, through an opening whose cross-sectional area and dimensions are smaller than those of the initial billet [1-5]. The cross section of the extruded metal will conform to that of the die opening. Principle of extrusion is shown in Figure 1.

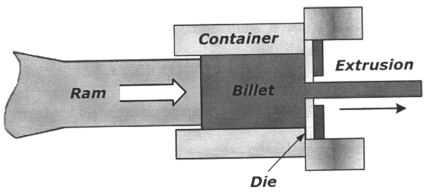

Figure 1: Principle of extrusion

Historically, extrusion was first used toward the end of the eighteenth century for producing lead pipes. It later gained widespread industrial applications for processing nonferrous metals and alloys like copper, brass, aluminum, zinc, and magnesium. Recently, with the modern developments in extrusion techniques, other metals like steel can be extruded.

Extrusion is the most used process in aluminum forming to produce different cross sections that used mainly in constructions like windows, doors frames, prefabricated houses structures and vehicles and aircraft parts and structures [6].

1.2. Fuzzy modeling

Fuzzy modeling is introduced as a practical alternative to conventional methods in solving modeling problems. Fuzzy system is recommended when a system without mathematical model or with high nonlinearity and uncertainty is to be modeled and controlled. Fuzzy system is simple in construction; it is simply a collection of linguistic IF_THEN rules. The rules can be obtained from an expert or by clustering input-output data [7]. In this paper the rules are developed through experience in extrusion process and by analyzing the data under consideration.

The Mamdani rule base is a crisp model of a system [8], i.e., it takes crisp inputs and produces crisp outputs. It does this with the use of user-defined fuzzy rules on user-defined fuzzy variables. Designing a Mamdani rule base requires three steps [8]: 1) determine appropriate fuzzy sets over the input domain and output range; 2) determine a set of rules between the fuzzy inputs and the fuzzy outputs that model system behavior; 3) create a framework that maps crisp inputs to crisp outputs. Fuzzy monitoring systems are considered in many applications in industry [9-12].

* Corresponding author. e-mail: alata@just.edu.jo

2. Experimental Setup

In order to develop an energy monitoring system for the extrusion line in MODAL (**Mod**ern **Al**uminum Industries Company), a data of energy consumption is obtained by NERC (**N**ational **E**nergy **R**esearch **C**enter) according to the signed agreement between MODAL & NERC. Three main hydraulic pumps supported the extrusion line in MODAL; data were collected from the power supply of these main three pumps. Clip-meters attached to the supply wires in order to get the amount of the energy consumed, one reading is recorded every 5 seconds by a PC where the data is saved. Data of 11 different dies was collected. Table 1 shows the dies numbers and their specifications, while Figure 2 shows sample of obtained data. In Table 1, PH stands for Port-Hole type die and F is for Flat type die.

Table 1: Extruded dies and their specifications

Die No.	No. of billets extruded	Speed (mm/sec)	Production rate (Kg/hr)	Die Type	Extrusion ratio	Specific energy (KJ/Kg)
510240-2	42	6	1284	PH	53.8	289.8
IMO-1	41	9.2	1670	PH	45	269.7
2111-B	47	9	1570	PH	46.8	277.7
1059-SR-16	127	9.2	1535	PH	53.5	279.7
1059-SR-14	126	8	1568	PH	53.5	281.2
1021-SR-12	152	8.2	1192	PH	65.2	294
0329-1	26	5.1	1022	PH	78.1	323.9
600060-2	50	5	732	PH	90.4	360.5
1009-SR-14	57	10	1677	F	35	245.7
1008-SR-7	79	7.5	1414	F	52.6	270.7
1580M	43	7.1	970	F	72.8	321.9

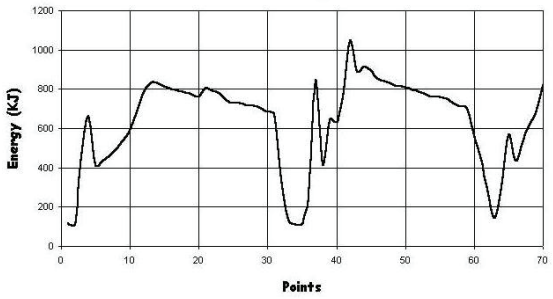

Figure 2: Sample of original data

For the die "1021 SR-12" 152 billets were extruded; two ideal maximum and minimum signatures are to be obtained. The aim is to predict unusual situations by monitoring energy consumption through the process of extrusion. For this die, the ideal extrusion speed was 8.2-mm/sec, billet length is 780-mm and ignoring the butt length, knowing that energy data was recorded every 5 sec; the expected number of readings for each billet can be computed by:

Time for each billet = billet length / extrusion speed
= 780 / 8.2 = 95.122

Number of readings for each billet = Time / time-interval
= 95.122 / 5 = 19.024 $\cong$ 19-reading.

The obtained actual number of readings is different from the ideal; Table 2 shows that billets have different extrusion time due to variation in extrusion speed. From the table, 28-billets have 27 readings and 20-billets with 26 readings; therefore, 27 readings can be used to investigate the energy consumption behavior.

Table 2: Number of billets of the same number of points

Number of points	Number of billets	Number of points	Number of billets
17	1	27	28
19	1	28	10
20	1	29	10
21	3	30	8
22	6	31	7
23	19	32	1
24	17	33	3
25	15	43	1
26	20	44	1
		All	152

3. Data Analysis

The data of the 28-billets of 27-points is used to estimate the max-min boundaries; the data of 25, 26, 28 & 29-points is modified to 27-points. First of all, the modification needs a good understanding of the signature behavior. Figure 3 shows one of the 28-billets, the signature starts at point 1 and reaches the 1st UP (upper-peak) at point 3, then it goes down to 1st LP (lower-peak) at point 4. The signature then goes up to 2nd UP at point 11. After the last peak, the signature goes down linearly to point 23, where the knee starts and it ends at point 25. The last peak, 3rd UP, occurs usually at point 26 and some times at point 25. Point 27 is the end point.

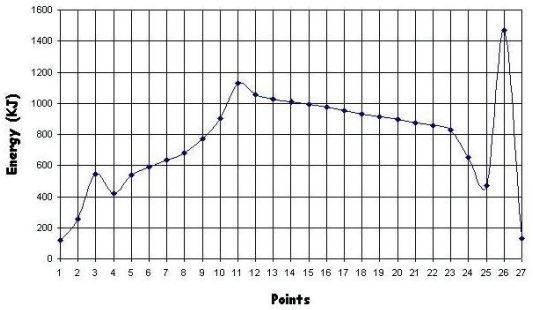

Figure 3: Sample signature of 27-points

We can clearly note that the modification can be applied to the linear region with no effect on the general scheme of the signature. Some modification can be applied to other regions to get close to ideal signature. Finally, 70 billets were modified; Table 3 shows 4 samples of the four modified ones.

For unmodified billet-58 of 25-points in Table 1, two points are added. The first one is the average of points 14 & 15 and it is inserted between them. The second one is inserted in the same way between points 19 & 20. Billet-100 of 26-points is modified like Billet-58 and one point is inserted between points 14 & 15. On the other hand, billet-15 of 28-points is modified by deleting point 15, and billet-18 of 29-points is modified by deleting points 2 & 14.

Table 3: Sample-modified signatures

Point No.	Billet-58 original	Billet-58 modified	Billet-100 original	Billet-100 modified	Billet-15 original	Billet-15 modified	Billet-18 original	Billet-18 modified
1	113	113	143.5	143.5	100.5	100.5	248.5	248.5
2	238.5	238.5	606	606	252.5	252.5	266	414.5
3	1115	1115	581.5	581.5	485.5	485.5	414.5	793.5
4	790.5	790.5	466.5	466.5	404	404	793.5	655.5
5	622.5	622.5	548	548	550	550	655.5	788.5
6	693.5	693.5	666.5	666.5	706.5	706.5	788.5	936.5
7	793.5	793.5	775	775	785	785	936.5	1043.5
8	904.5	904.5	887	887	1144	1144	1043.5	910
9	1090.5	1090.5	1070	1070	1054.5	1054.5	910	886
10	1054.5	1054.5	1118	1118	880.5	880.5	886	866.5
11	1016.5	1016.5	1065	1065	875	875	866.5	856.5
12	1037	1037	1060	1060	849.5	849.5	856.5	845.5
13	991.5	991.5	1032.5	1032.5	847.5	847.5	845.5	801.5
14	978	978	1007	1007	832	832	772.5	792
15	959	968.5	982	994.5	847.5	807	801.5	778
16	945.5	959	968.5	982	807	778.5	792	767
17	921.5	945.5	946	968.5	778.5	773.5	778	753.5
18	904.5	921.5	923.5	946	773.5	765.5	767	739.5
19	890	904.5	888.5	923.5	765.5	751.5	753.5	731.5
20	865	890	887	888.5	751.5	736	739.5	714
21	837.5	877.5	858.5	887	736	722	731.5	700.5
22	813	865	609	858.5	722	687.5	714	661
23	659.5	837.5	439.5	609	687.5	709	700.5	463
24	960	813	427	439.5	709	646	661	387
25	114	659.5	254	427	646	463	463	750.5
26	-	960	165.5	254	463	691.5	387	240.5
27	-	114	-	165.5	691.5	131.5	750.5	104
28	-	-	-	-	131.5	-	240.5	-
29	-	-	-	-	-	-	104	-

3.1. Estimating the max-min boundaries

Some of the real world distributions are normal; consider the values at each point to be distributed normally. Then, the boundaries of random sample from a normal distribution with $(1-\alpha)\times 100\%$ confidence interval will be:

$$\min < \mu < \max$$

$$x' - \frac{t_{\alpha/2} \times s}{\sqrt{n}} < \mu < x' + \frac{t_{\alpha/2} \times s}{\sqrt{n}}$$

where:

x' = sample mean

N = number of samples

$t_{\alpha/2}$ = t-value from t distribution table with $v = n - 1$ degrees of freedom, leaving an area of $\alpha/2$ to the right.

s = standard deviation;

$$s^2 = \sum_{i=1}^{n} \frac{(x_i - x')^2}{n-1}$$

In our case we have $n = 70$ and $\alpha = 0.01$ to get 99 % confidence interval. The max-min boundaries are shown in Figure 4. Based on the boundaries, the building process for the fuzzy system can begin.

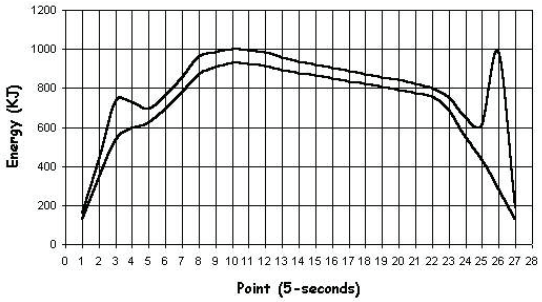

Figure 4: max-min boundaries

3.2. Fuzzy System

First of all, inputs and outputs of the system must be identified. In our case, we have two inputs (Region & Error), and one output (Situation). Figure 5 shows the standard deviation of the samples at each point of the 27-points this figure is needed in input-output identification.

1st Input: Region

From Figure 5, we can divide any signature into 3-Regions. The crisp regions are:

R1 : points from (1) to (5)

R2 : points from (5) to (22)

R3 : points from (22) to (27).

The fuzzy membership functions are shown in Figure 6.

2nd Input: Error

To indicate if the input signature exceeds the max-min boundaries or it is within range, the following input is defined as:

Error = min(max_value – input_value, input_value – min_value)

This min. function produces the error input. If the input signature exceeded any boundary, a negative input error is produced and if the input signature is within range, the input error is positive.

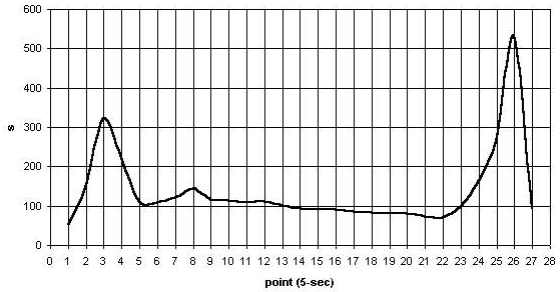

Figure 5: Standard deviation of samples

Fuzzy membership functions for the Error are shown in Figure 7. These functions are as follows:

In_range : +ve error is produced
e : accepted –ve error is produced
ee : significant –ve error is produced

The Output: Situation

The real on-line output is needed to be crisp and not fuzzy. It can be an alarm, buzzer, stop etc.; the output is designed to give an approximate description of the situation in term of percentage. The output membership functions are shown in Figure 8; the situations were selected logically to be:

Normal: nothing unusual, the situation is OK
Be_careful: keeps attention about the situation
Problem: a problem occurred

Fuzzy System Rules:

Typically, the number of rules is the product of the number of the membership functions of each input. In our case, the number of rules supposed to be 3*3 = 9-rules, but 7-rules were written for this system. The rules are:

IF (Error is in_range) **THEN** (Situation is Normal)
IF (Region is R1) and (Error is e) **THEN** (Situation is Normal)
IF (Region is R2) and (Error is E) **THEN**(Situation is be_careful)
IF (Region is R3) and (Error is e) **THEN** (Situation is Normal)
IF (Region is R1) and (Error is ee) **THEN** (Situation is be_careful)
IF (Region is R2) and (Error is ee) **THEN** (Situation is Problem)
IF (Region is R3) and (Error is ee) **THEN** (Situation is be_careful)

The first rule cancels two rules, because in_range signature in any region is safe and then the situation is normal. For regions R1 & R3 a high standard deviation can be noted and this means that the prediction is highly uncertain. Region R2 is a stable region with low standard deviation. Therefore, any significant value for error indicates, mostly, a problem.

3.3. System Examination

To examine this system, a billet of 24-points was modified to 27-points as explained above. Table 4 shows the signature and its evaluation according to the proposed fuzzy system. We can conclude from this table that the signature is within limits and there is nothing to worry about. The maximum number in the evaluation column is 50 which mean means the situation is normal or be careful according to Figure 8.

Table 4: Evaluation of the signature of billet 50

point	Billet 50	Billet 50-evaluation	point	Billet 50	Billet 50-evaluation	point	Billet 50	Billet 50-evaluation
1	116	20.3659	10	1027.5	34.7335	19	856	19.1842
2	239	19.1842	11	1013	30.5996	20	846.5	21.0078
3	962.5	50	12	998.5	28.4504	21	816	19.1842
4	759	21.6239	13	957	19.1842	22	798.5	19.1842
5	758	19.1842	14	931.5	19.1842	23	751.5	19.1842
6	879.5	26.9787	15	945.5	33.7021	24	629.25	19.1842
7	965.25	34.2143	16	917.5	26.9787	25	507	50
8	1051	41.5449	17	888.5	19.1842	26	1278	50
9	1012.5	37.0964	18	863	19.1842	27	211.5	21.4578

Figure 6: Membership functions for "Region" input

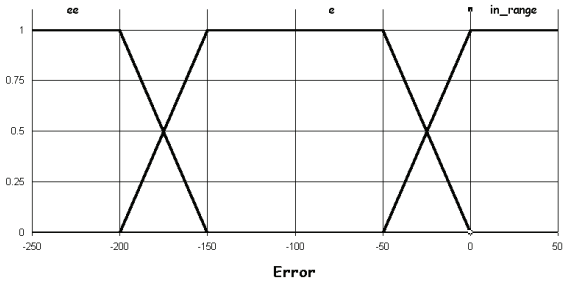

Figure 7: Membership functions for "Error" input

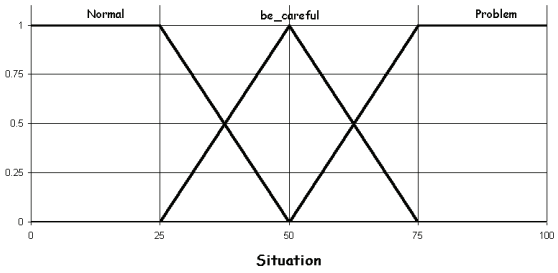

Figure 8: Membership functions for "Situation" output

4. Signature Behavior

In order to explain the signature behavior, the average of the 70 billets will be examined in Figure 9. In the first going up part of the signature, the heated billet is compressed and fills the clearance between the billet and the container by caused lateral strain. In the second going up part, a metal flow is going to overcome the static friction between the billet and the container,as well as between the metal and the die.

In the going down part in the mid of the signature, the friction becomes dynamic; the size to be extruded get decreased and the billet is heated up by the friction between atoms. The energy decreased semi-linearly. The peak at the end of the signature can be related to the impurities increasing, so the remaining metal becomes harder and stronger.

The extrusion process internally is a flow of atoms on each other. The slipping on the planes that contains impurities is harder than other pure planes and thus needs more energy. The whole signature behavior can be simply related to this principle, so that the composition of the billet and the distribution of impurities may affect the behavior.

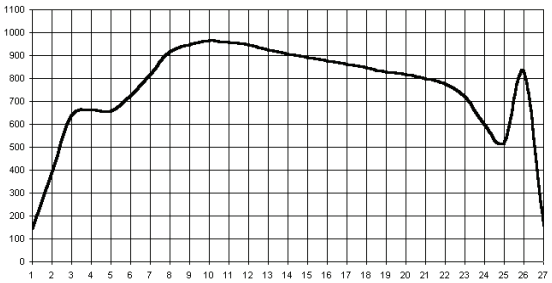

Figure 9: The average of the 70-signatures

5. Conclusions

In this work, a monitoring system of an extrusion line is developed; a data of energy consumption is collected. The signatures of the billets extruded are studied to understand the signature behavior. Max-Min boundaries are found and a fuzzy system that makes use of the boundaries is built to indicate unusual situations. The real on-line output is crisp and not fuzzy. It can be an alarm, buzzer, stop etc.; the output is designed to give an approximate description of the situation in terms of percentage. To examine this system, a billet of 27-points is chosen. The signature has been evaluated according to the proposed fuzzy system. The proposed system works well in defining the real situation of the extruder.

References

[1] Rens B. Finite element simulation of the aluminum extrusion process. PhD thesis, Technical Eindhoven University, Netherlands, 1999.

[2] Lof J. Development in finite element simulation of the aluminum extrusion. PhD thesis, University of Twente, Netherlands, 2000.

[3] Kalpakjian S. and Schmid S. Manufacturing Engineering and Technology. Prentice Hall,2001.

[4] Donati L. and Tomesani L, "The prediction of steam welds quality in aluminum extrusion". Journal of Materials Processing Technology. Vol. 153-154, 2004. 366-373.

[5] Hydro Aluminum North America. Extrusion Design Manual, 2005,USA.

[6] Altenpohl D. Aluminum viewed from within. First edition, Dusseldorf, Germany, 1982.

[7] Chiu S. "Fuzzy model identification based on cluster estimation". Journal of Intelligent and Fuzzy Systems, 1994, Vol.2,267–78.PP.267-278.

[8] Mamdani E.H and Assilian S., An experiment in linguistic synthesis with a fuzzy logic controller. International Journal of Man-Machine Studies. 1975,Vol 7,1–13.

[9] King, P. J. and Mamdani, E. H. The Application of Fuzzy Control Systems to Industrial Processes. Automatica, Vol.13, 1977, 235-242.

[10] Kickert, W.J.M. and Van Nauta Lemke, H. R. An Application of a Fuzzy Controller in a Warm Water Plant. Automatica, 1976,Vol.12,301-308.

[11] Chen, J. C. "An effective fuzzy-nets training scheme for monitoring tool breakage". Journal of Intelligent Manufacturing, 2000,Vol.11,No1,85-101.

[12] Mihaela U. and Robert M., "Integrated Analytical and Fuzzy Simulation Modeling for Monitoring and Supervision of Machinery".International Journal of Manufacturing Systems Design, 1995,101-125.

JJMIE

Volume 1, Number 1, Sep. 2007
ISSN 1995-6665
Pages 23 - 29

Jordan Journal of Mechanical and Industrial Engineering

Effect of Water Depth on the Performance Evaluation of Solar Still

Muafag Suleiman K. Tarawneh *

Mechanical Engineering Department, Faculty of Engineering, Mutah University, P.O.Box 7, Karak 61710, Jordan

Abstract

Desalination of ground brackish water by solar powered systems is a practical and promising technology for producing potable water in the regions which suffers from water scarcity especially in arid areas. In remote and arid areas in Jordan with low infrastructure and without connection to the national grid, the abundant solar radiation intensity along the year, and the available brackish water resources are two favorable conditions for using the desalination solar technology to produce the fresh water, even for domestic use. Based on these conditions, a small-scale solar powered desalination system has been constructed and operated. The present study aims to improve the solar still performance, and to increase its productivity. So it is necessary to evaluate some important parameters affecting the system productivity. The effect of water depth in the basin on the water productivity was evaluated. In the same time, the effect of the deign and operational parameters on the solar desalination process were investigated. Different depths of brackish water (0.5cm, 2cm, 3cm, and 4cm) with TDS of 5000ppm were tested under the same climatic conditions in Mutah University. A six months study showed that the still productivity is strongly dependent on the climatic, design and operational conditions. The obtained results showed that the decreased water depth has a significant effect on the increased water productivity, while the performance characteristics showed that the water productivity was closely related to the incident solar radiation intensity. The balanced conditions between the increased evaporation rate and the rapid condensation ware due to the merit contribution of the carefully applied glass cover cooling.

Keywords: Solar still; Brackish water depth; Water Productivity; Testing hours; Jordan.

1. Introduction

Desalination method has long been considered as the practical solution for the current and future demand of potable water. Desalination process is used to reduce the Total Dissolved Solids (with TDS of 5000 p.p.m and above) to an acceptable level of TDS equal to 500 p.p.m. Different desalination technologies can be applied. Desalination of ground brackish water by solar powered systems, is a practical and promising technology for producing potable water in the regions which suffers from water scarcity especially in the remote arid areas [1]. The rapid population growth, along with the expected social and economic development will increase the demand for water in such a way that the future water reserve in Jordan will not meet such a demand. Jordan in particular will face sever shortage of fresh water [2,3]. The 1998 water crisis is a good example.

In remote and arid areas in Jordan with low infrastructure and without connection to the national grid, the abundant solar radiation intensity along the year, and the available brackish water resources are two favorable conditions for using the solar powered desalination technology to produce the fresh water, even for domestic use. A small scale solar desalination technology, might to be technically and economically viable to cope with water scarcity, and it is recommended to be used in the remote and isolated communities, particularly for those areas which enjoys with abundant solar radiation intensity. Desalination of brackish water was expanded rapidly to support urban and industrial developments in the arid areas, good results were published by some researchers in the field of solar desalination [4,5].The recent sharp increase in energy prices makes the solar desalination technique a more attractive method for obtaining fresh water. Furthermore, the valuable solar radiation intensity which Jordan enjoys (5.5 kwh/m^2.day (19.8 MJ/m^2.day)), along with the high average sunshine duration (3300 hrs/year (300 days/year)), with 9-10 daylight hours for the most geographical locations encourages the use of such a solar resource. Data for the years 1960-2005 obtained from the Jordan Meteorological Department (JMD) encourages further research activities in the field of solar energy application. In order to enhance the solar stills productivity, numerous groups around the world have contributed to improve the solar desalination technology,

* Corresponding author. e-mail: tatmuf@mutah.edu.jo

by evaluating the influence of some important parameters on the system performance. The effect of climatic conditions; deign and operational conditions and geographical location on the water productivity [6,7,8,9,10, 11] were investigated. It is well known that the distillate output decreases significantly with the increase of water depth in the basin of the solar still; also, with the same solar irradiance the evaporation rate increases with the reduced mass of water on the absorber pate [12,13]. The effect of these parameters on the solar powered desalination process were evaluated before starting the experimental phase of the present work. Based on these information, the effect of water depth in the basin of solar still was evaluated. In the same time, the effect of the deign and operational parameters on the solar desalination process were investigated. Different depths of brackish water with TDS of 5000ppm (0.5cm, 2cm, 3cm, and 4cm) were tested under the same climatic conditions in Mutah University. Two greenhouse type solar stills were constructed and used. Both solar stills were utilized under the same operational conditions. The obtained results showed a significant increase in the amount of produced water especially for the tested depth of a brackish with 0.5 cm whereas; the fastest condensation rate was achieved after applying the method of cooling the glass cover.

2. System

2.1. System Description

Major handicaps which influence the still performance such as: dry spots and scale formation, air-tight conditions, glass cover inclination were investigated by different researchers; and good results were published [9,10,13,14]. The major handicaps that negatively influence the solar still productivity were taken in consideration, and some improvements on the design and operational conditions were made. In order to successfully perform the experimental investigation and to accurately evaluate the effect of water depth on the increased water productivity, it was necessary to investigate many depths of water under the same operational conditions. For that reason, two symmetrical greenhouse-type solar stills were constructed, and some improvements were made. Basically, each unit consists of the following parts as shown schematically in Figure 1:

1. The Aluminum metal is a good conductor and concentrate the heat energy at the surface layer, so the black-painted absorbing plate is made of 3 mm thick Aluminum sheet with an absorbing area of $1m^2$ (1.25*0.8), four uniformly distributed points of support are placed under the absorbing plate to provide the correct water level, as well as to prevent the tendency of deflection that can cause the formation of dry-spots.

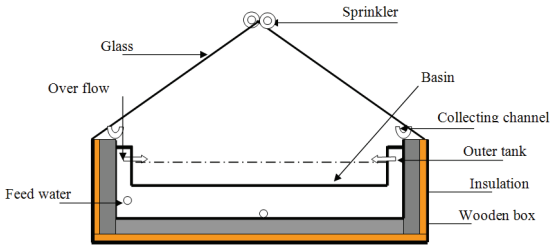

Figure 1: Schematic sketch of the testing unit (solar still) used in the present work

2. The airtight glass cover is formed of two glass sheets (4 mm thick) with an inclination of 40^o. Both sheets are supported on the steel frame and properly sealed with rubber to prevent the air leakage.
3. The insulated outer tank, in which 8 cm of rock wool is properly placed on all the basin sides and bottom, is enclosed within 2 cm wooden box and externally is surrounded by 0.3 galvanized iron-sheet.
4. In each solar still twelve thermocouples are uniformly distributed on the centerlines of the glass sheets and the basin plate in order to measure accurately the temperature variation
5. Brackish or saline water (sample of Brackish ground water collected from Al-Tanoor dam and Alkafrein-Hisban with TDS of about 5000 p.p.m). Feed water can be fed continuously or intermittently by two methods. In the first method, the feed water can be fed to the lower tank through the feed water header, after filling the lower tank, an over-flow of brackish water is fed to the upper basin through number of small drilled holes (3mm in diameter) distributed on the inside perimeter of the upper basin. While in the second method the brackish water is fed directly to the upper basin through a steel pipe that is centrally placed above the basin plate with 5 cm, the steel pipe has sufficient number of drilled hole to ensure better water distribution on the absorbing plate.
6. The collecting channel is made by PVC and placed on the base of the glass cover with an inclination of 5^o towards the collecting header in order to speed up the condensate velocity and to avoid the tendency of re-evaporation.
7. Two sprinklers are constructed and installed on the top part of each solar still in order to ease splashing method and to cool the glass cover.
8. Black plastic jackets (polyethylene) with the same dimensions of the inner basin are made in order to eliminate the maintenance cost as well as the effort of cleaning the deposited scales on the absorbing plate. The properties of selected thermoplastic polyethylene high density material (PE-HD) are indicated in Table 1

Table 1: Properties of PE-HD $[-CH_2-CH_2-]_n$

State	High density
Density [g/cm^3]	0.957
Melting temperature [º C]	130-137
Thermal conductivity [w/m.k]	0.48
Effective thermal diffusivity [mm^2/s]	0.092
Enthalpy difference [kj/kg]	650
Humidity absorption [%]	0.01

2.2. Working principle of the solar still

A small-scale hydrological cycle can be created in a well designed solar still. The air tightness and the good insulation, are two essential design parameters that should be highly considered in order to minimize the vapor leak and heat loss tendencies .

Solar stills are used to produce fresh water from brackish water by directly utilizing the sunshine. Construction and operation principle of solar stills are very simple. The black painted absorbing plate contains the brackish water which is directly exposed to the solar energy above the plate. The brackish water is completely enclosed in an air-tight conditions inside the transparent glass cover. The incident solar radiation passes through the transparent glass cover and is absorbed by the black-painted Aluminum sheet, the absorbed heat is then transferred to the water with no significant energy loss. The brackish water start heating and evaporating, the formed vapor on the water surface start moving in an upward direction as due to the created driving force (convective currents) due to the temperature difference between the water and glass cover (T_w-T_g). When the water vapor comes in contact with the condensing surface (glass cover which is externally cooled) in order to improve the condensation rate, the vapor will condense at different small-size droplets of fresh water, then the condensate starts moving down along the inclined glass cover due to the gravitational force. Finally, the condensate will be collected from the collecting channel which is connected to the collecting vessel.

2.3. Design description

Two symmetrical greenhouse solar stills were constructed, and the experimental investigation regarding the effect of water depth on the still productivity was carried out. Because the solar still productivity was strongly dependent on the design and operational conditions, the accepted thermal performance which was achieved was due to the improved design parameters and optimized operational technique.

The initial investigations were carried out in September, 2004; the negative aspects regarding the design and operational parameters were detected and treated. Practically, both stills were filled with two different brackish water depths. Each time the lower depth of 0.5 cm brackish water (above the absorbing plate) in one solar still was tested and compared with other brackish water depths (2cm, 3cm, and 3cm) in the second solar still. The solar stills were properly oriented, and directly exposed to the solar radiation. Both stills were operated during the typical days of September, 2004; the time interval of four days was sufficiently enough to execute all the necessary calibrations and adjustments. The remarkable results and visual observations during the initial investigations ware due to the accurate adjustments and calibrations. Based on these observations, the system of measurement was carefully established during the testing period, all the key quantities were carefully measured and recorded at a time interval of every 15 working minutes. The measured parameters and quantities ware; the solar radiation intensity (I), the glass temperature (T_g), the basin water temperature (T_w), and the ambient air temperature (T_a). The designed system has the following important characteristics:

1. The negative effect of scale formation on the absorption efficiency, and the increased cost of cleaning the white scale are two important causes of reducing the solar still efficiency. So, the need for using the designed black and replaceable plastic jackets having the scope of minimizing the cost of cleaning and maintenance. The plastic jackets were placed in each solar still. By using these plastic jackets, a higher absorbability can be maintained, and the scale formation become an ignored problem
2. The water surface level was precisely adjusted to avoid the dry spots, mainly at shallow water depths.
3. The proper material selection, and fabrication of the absorbing plate has a positive effect on the increased basin water temperature. In order to ensure an efficient capturing of solar irradiation, the absorbing plate is made of Aluminum sheet because of its thermal conductivity. (see Table 2)

Table 2: Thermo physical properties of Aluminum

Melting point [k]	933
Density [kg/m^3]	2706
Specific heat cp [J/kg.k]	903
Thermal conductivity [W/m.k]	237

The rapid formation of a thin vapor film on the internal sides of the glass cover was clearly observed after 25 minutes of exposing the distiller to the solar radiation. Also, the uniform distribution of the generated small size water droplets that started moving in an organized down-sliding motion to the collecting channel was observed to occur rapidly during the initial stages. The accepted thermal behavior was ensured by the last two characteristics. Unfortunately, despite the achieved performance, the water productivity was below the expected value. So, extensive efforts were made to determine the suspect reasons. Further examinations were conducted to investigate these reasons. The repeated attractive results during the start of each experiment demonstrated categorically that the design parameters had no negative effects on the reduced water productivity. The close inspection made on the data related to the measured quantities was of a great contribution in finding the suspect cause of the reduced productivity. It was observed that the sharp increase in glass temperature (T_g) because of the effect of latent heat of condensation, which having a significant role in raising the glass temperature, a temperature much higher than the ambient (T_a) and very close to the water temperature (T_w), could be the main reason of decreasing the rate of evaporation and then water productivity. Such a high temperature might have a

negative effect on the condensation process and the driving force of the convective currents. Several recent studies reported that the positive contribution of cooling the glass cover [15,16,17,18]. The role of condensing cover is very important in solar distillation systems; it has to permit solar radiation to transmit, and to dissipate the heat to the ambient to provide efficient condensation [10]. Others have found the significant effect of the increased temperature difference (T_w-T_g) on the productivity of the green house solar still during the earlier night hours. They reported about 50-60% higher productivity during the early night hours than during the daylight hours. This was attributed to the positive effect of the stored heat and the increased temperature difference (T_w-T_g) [3,19]. These observations lead to the decision of applying the glass cover cooling. Based on the visual observations (faster water droplets motion) and the inspected values of the measured quantities, the periodicity of cooling the glass cover was accurately optimized to be performed every 15 working minutes. The cooling system consisted simply of two steel pipes with sufficient number of small-drilled holes (3mm in diameter). The designed sprinklers were located on the top part of each solar still to ease splashing both glass sheets at the same time. Practically, a jet of 20 ºC of water was applied to cool the glass cover. Time duration of one minute was sufficiently enough to create an accepted temperature difference of about 8 to 10º C between the glass and brackish water temperatures. Splashing of the glass cover was applied with five minutes before taking the temperature readings. The temperature readings was taken at 15,30,45,and 60 minutes. Finally, the initial stage of inspecting the design parameters and optimizing the operational technique was successfully achieved as indicated by the accepted thermal performance. The solar still productivity could be increased when an extra heat is provided from any available source of heat. Different studies with different design arrangements showed that solar still productivity can be increased when extra heat is fed to the system [20,21]

3. Results and Discussion

Practically, a number of experimental investigations were conducted to demonstrate the overall objective of the present study. All the selected water depths were tested in Mutah University at 1050 m above the sea level. The effects of water depth operational and design parameters and geographical location were evaluated.

The lower brackish water depth of 0.5cm (mass of water above the absorber) was tested in each experiment; the results were compared in each time with those obtained from the other tested water depth in the same experiment. The testing procedure was carried out during the winter of 2004-2005 and summer of 2005 as clarified in table 3.

Consisted with the planned timetable 3, the obtained results of the tested two water depths and in each experiment were compared and evaluated. The interval of four days was sufficiently enough to explore the effect of water depth on water productivity. It should be mentioned that both testing units were operated in the first two days in each experiment without cooling the glass cover while in the last two days the glass cover cooling was applied (only during the summer months of June, July, and August/2005). The effect of different parameters was evaluated through the obtained results as follow:

3.1. Effect of design and operational parameters

The same results obtained from both testing units with a water depth of 4cm showed the same thermal performance. The experiment was conducted under the solar radiation intensity of 7.73 kwh/m^2.day (27.8 MJ/m^2.day)in which both solar stills were exposed to the solar radiation for a time interval of 10 hours, the obtained results of 4.745 and 4.733 respectively showed nearly the same thermal performance and the same effect of the design parameters.

3.2. Effect of water depth on the solar stills productivity

The experimental results have shown with no doubt that the water depth has a significant influence on the increased productivity. So, the objective of the present work have successfully achieved as shown on the performance curves.

All the experiments were conducted as conform the planned timetable, and separate thermal behavior was made for each tested depth. Figure 2 illustrated the planned timetable and the experiments were conducted under the described conditions such as the average solar radiation intensity of 7.73 kwh/m^2day (27.8 MJ/m^2.day), and operational time of 11 daylight hours.

Table 3: Time table of testing the water depths

Tested depths of ground brackish water. 0.5 in one testing solar still, and 2,3,4 cm in the other solar still	**Summer months (2005)** Average sunshine duration is of 11.8 hrs/day. Average solar radiation intensity is 7.73 kwh/m^2.day, or (27.8MJ/m^2.day)			**Winter months (2004/2005)** Average sunshine duration is of 6-hrs/ day. Operational time of 6 hrs/day (9 am-16 pm) Average solar radiation. Intensity is 3.35 kwh/m^2.day, or (12.73 MJ/m^2.day)		
Tested depths	June	July	August	December	January	February
0.5 cm, 2 cm	15-18	10-13	3-6	5-8	9-12	10-13
0.5 cm, 3 cm	20-23	15-18	3-11	10-13	14-17	15-18
0.5 cm, 4 cm	25-28	20-23	15-18	17-20	21-24	20-23

Results are shown for all the tested water depths. It can be seen from Fig.2 that each tested depth has two values: the first value represents the obtained productivity before applying the cooling method in which the productivity from the lower water depth has 8% higher than that obtained from the tested depth of 2 cm. the same increase of 12% higher than that obtained from the depth of 3 cm, and an increase of 14%in water productivity than that obtained from the depth of 4 cm.

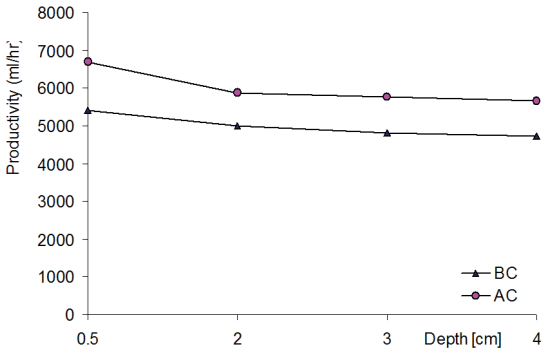

Figure 2: Productivity versus water depth before cooling (BC) and after cooling (AC)

3.3. Effect of cooling the glass cover

In comparison with the previous results which obtained before cooling the glass cover The significant effect of cooling the system is strongly observed on the increased productivity. The effect of cooling the glass cover shows an increase on the water productivity with about 17-23%. The increased productivity is achieved for all the tested depths under the effect of cooling. In each experiment, the lower depth was observed with the higher output than the other tested depths. Also Figure 2 shows the results before and after cooling for all the tested depths. The lower depth as compared with the other depths has 14% higher than that of 2 cm, 16% than that of 3 cm, and 18% higher than that obtained from the tested depth of 4cm, To explore the merit contribution of the applied cooling method, a comparative evaluation was made separately for each water depth as shown in figures (3,4,5, and 6). The obtained results before and after cooling the glass cover are tabulated in table 4.

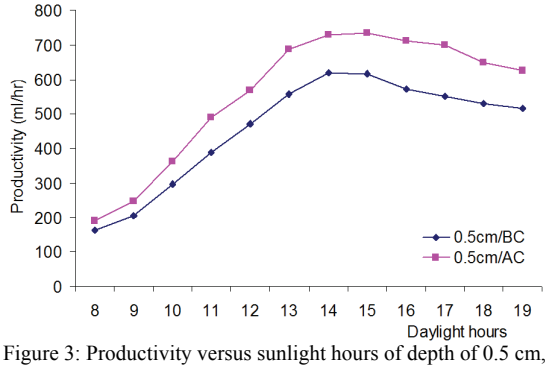

Figure 3: Productivity versus sunlight hours of depth of 0.5 cm, with 5.400 Lit/day before cooling and 6.693 Lit/day after cooling (an increase of 23%)

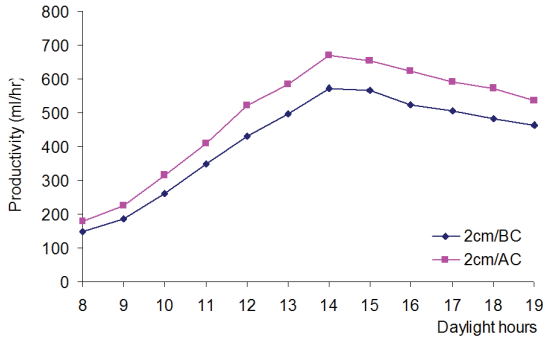

Figure 4: Productivity vs. sunlight hours of the depth of 2 cm, with 4.990 Lit/day before cooling and 5.883 Lit/day after cooling (an increase of 18%)

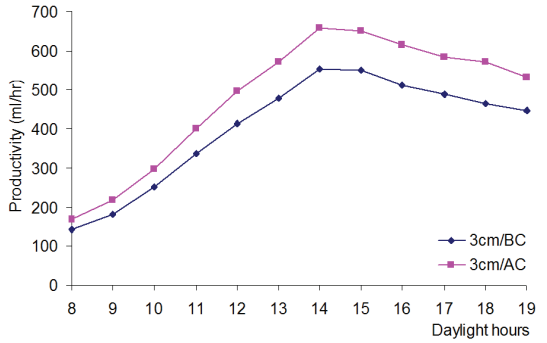

Figure 5: Productivity vs. sunlight hours of the depth of 3 cm with 5.756 Lit/day after Cooling and 4.817 Lit/day before cooling (an increase of 19%)

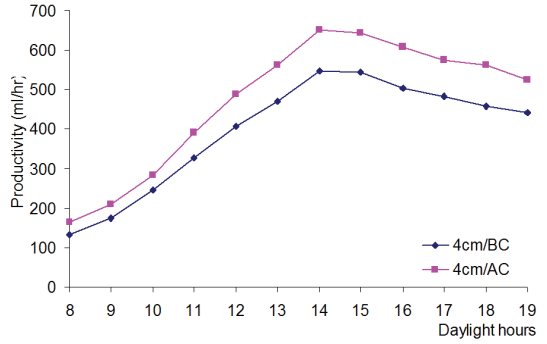

Figure 6: Productivity vs. sunlight hours of the depth 4 cm with 5.660 Lit/day after cooling and 4.733 Lit/day before cooling (an increase of 19%)

Table 4: water productivity before and after cooling for each water depth

	Water depth [cm]	Productivity before cooling [lit/day]	Productivity after cooling [lit/day]	Percentage of increase [%]
Figure 3	0.5 cm	5.400	6.693	23
Figure 4	2 cm	4.990	5.883	18
Figure 5	3 cm	4.817	5.756	19
Figure 6	4 cm	4.733	5.660	19

The tabulated data gives a clear image about the effect of the decreased depth on the increased productivity. The

same observations can be made on the positive effect of cooling the glass cover and the resulting increase on the temperature difference (T_w-T_g).

The increased productivity from the lower depth (small mass) is directly related to the increased evaporation rate as well as the faster condensation which is due to the cooling effect. The merit contribution of the cooling method is strongly observed on the increased temperature difference (T_w-T_g) which is nearly 10 ºC after cooling instead of 4 ºC before cooling. A separate thermal behavior is made to show the increased (T_w-T_g) for each tested water depth, and the results are properly represented on the time-temperature curves as shown in Figure 7, (0.5 in comparison with 2cm). The results show the positive effect of cooling the glass cover as indicated by the increased temperature difference (T_w-T_g), and nearly the same increase is obtained for all the tested depths. The last figure (Fig.8) shows a clear image of the created difference after cooling as well as before cooling for all the tested depths. Figure 8 shows the time temperature variation before and after cooling for both tested depths of 0.5 and 2 cm. The ambient temperature, glass temperature and water temperature before and after cooling were measured for every 15 minutes. The obtained results were used to compute the temperature difference for each tested depth and plotted in Figure 7.

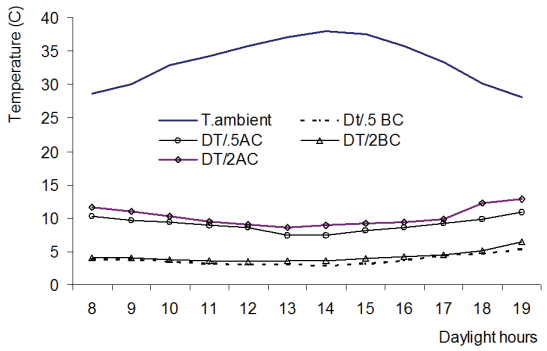

Figure 7: Temperature difference (T_w-T_g) vs. the sunlight hours, for the depths of 0.5 and 2 cm before and after cooling

Actually the thermal performance of the other tested depths are nearly the same, but with different values. Practically, figure 8 can be considered as a sample for the other time-temperature variation regardless the other tested depths.

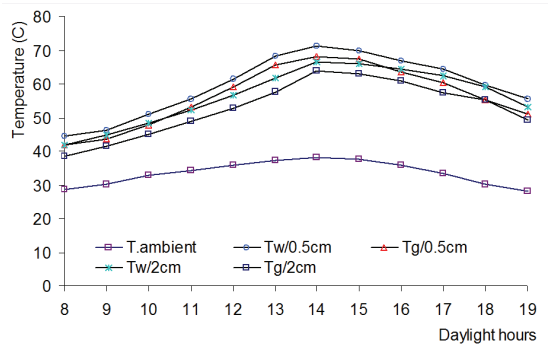

Figure 8: The time vs. temperature variation of ambient, water and glass temperature (before and after cooling) for the depths 0.5 and 2 cm

The obtained productivity from the lower depth with 6.699 Lit/Day shows an accepted agreement with the theoretical productivity of 8.6 lit/day that can be produced under the available climatic conditions. Dividing the experimental output of the lower depth by the theoretical one, the efficient percentage efficiency of solar utilization comes to be about 75%.

4. Conclusions

The major interesting results of the present work can be summarized in the following points:

1. The accepted thermal performance of the constructed solar still with an increased evaporation rate and the faster condensation was achieved due to the appreciated contribution of the improved design parameters and the operational.
2. The merit contribution of using the plastic jackets had a significant role for minimizing the effort of cleaning the deposited scale (by using a new jacket when needed) and maintaining efficient capturing of solar irradiation.
3. The deciding role of cooling the glass cover was strongly observed on the increased temperature difference (T_w-T_g) as well as on the increased water productivity. Higher attention must be spent to the times of applying the cooling method.
4. The concept of using the greenhouse solar stills was found to be very attractive method for obtaining the fresh water even for a small-scale demands, because of several economic and technical advantages such as, the inexpensive technology including the material prices and manufacturing.
5. An efficient utilization of the solar energy could minimize the need for using the expensive conventional sources of energy and meet the energy saving requirements.
6. The efficient utilization of the solar energy with a percentage of 70% was reached and demonstrated by the good agreement between the obtained productivity of 6.7 Lit/day and the theoretical productivity of 9.5 Lit/day that could be obtained under the available climatic conditions.
7. The possibility of increasing the water productivity could be reached by lowering the water depths on the basin- absorbing plate. It is necessary to investigate the effect of all the operational parameters before taking the decision of installing the solar distillation plant.
8. It was found that the geographical location may having a significant positive effect on the increased water productivity, especially for those locations with an abundant solar irradiation and situated at higher elevations above the sea level, where the reduced boiling point of water and the corresponded saturation pressure are below the standard atmosphere.

Reference

[1] G.R. Lashkaripour, M. Zivadar, Desalination of brackish water in Zahedan city in Iran, Desalination Vol177.2005,1-5.

[2] Gleick, P.H., Water, War, and Peace in the Middle East, Environment,Vol.36 1994,6 – 42

[3] United Nations, Comprehensive Assessment of the fresh water resources of the world, 1997.

[4] Bchiar Bouchekima, A small solar desalination plant for the production of drinkable water in remote arid areas of southern Algeria, Desalination, Vol. 159 ,2003, 197-204.

[5] J. Joseph, R. Saravanan, S. Renganarayanan. Studies on a single-stage solar desalination system for domestic applications, Desalination, Vol.173,2005, 77-82.

[6] AL-Hinai H., AL-Nassiri M.S., and Jubran B.A., Parametric investigation of a double effect solar still in comparison with a single-effect solar still, Desalination, Vol.150, 2002, 75-83

[7] Akash B., Naifeh W., and Mohsen M., Energy Conversion and Mgmt, Vol.41, 2000, 883

[8] Duffie J.A., and Beckman W.A., Solar Engineering of Thermal Processes, John Willey and suns 1980

[9] M. Boukar, A. Harmim, Parametric Study of a vertical solar still under desert climatic conditions, Desalination, Vol.168, 2004, 21-28

[10] Anil Kr., G.N. Tiwari, Effect of the condensing cover's slope on internal heat and mass transfer in distillation: an indoor simulation, Desalination, Vol.180, 2005, 73-88.

[11] Hikmet S. Ayber, Mathematical modeling of an inclined solar water distillation system, Desalination, Vol.190, 2006, 63-70.

[12] Rajesh Triphathi, G.N. Tiwari, Effect of water depth on internal mass transfer for active solar distillation, Desalination, vol.173, 2005, 187-200.

[13] A.A. El-Sebaii, Thermal performance of a triple-solar still, Desalination, vol.174, 2005, 23-37.

[14] H.S. Aybar, F.Egelioglu and U. Atikol, An experimental study on an inclined solar distillation system, Desalination, Vol.180, 2005, 285-289.

[15] Abu-Arabi M.K., Zurigat Y.H., and AL-Hinai H, Modeling and performance analysis of a solar desalination unit with double glass cover cooling, Desalination, Vol.143, 2002,173-182.

[16] Tiwari G.N., and Garg H.P., Effect of water flow over the glass cover of a single basin solar still with intermittent flow of waste flow of waste hot water, Energy Conversion and Mgmt., Vol. 25, 1985, 315-322

[17] Lawrence S.P., and Tiwari G.N., Effect of heat capacity on the performance of solar still with water flow over the glass cover, Energy Conv. and Mgmt, Vol.30, 1990, 277-285

[18] Malik G.N., and Sodha M.S., The effect of geographical location on the solar distillation efficiency, Solar Distillation, Pergamon press, Oxford 1982.

[19] Voropoulos K., Mathiolakis E., and Belessiotis V., Experimental investigation of a solar still coupled with solar collector, Desalination, Vol.138, 2001, 103-110.

[20] Carmen Esteban, Judith Franco, Construction and performance of an assisted solar distiller, Desalination, Vol.173, 2007, 249-255.

[21] V. Velmurugan, K. Srithar, Solar stills integrated with a mini solar pond, analytical simulation and experimental validation, Desalination, vol. 216, 2007, 232-241

JJMIE

Volume 1, Number 1, Sep. 2007
ISSN 1995-6665
Pages 31 - 41

Jordan Journal of Mechanical and Industrial Engineering

A Nonlinear Torsional Dynamic Model of Multi-Mesh Gear Trains Having Flexible Shafts

Ahmad Al-Shhyab [a,*], Ahmet Kahraman [b]

[a] *Department of Mechanical Engineering, Hashemite University, P.O. Box 330127, Zarqa 13133, Jordon*
[b] *Department of Mechanical Engineering, The Ohio State University, 650 Ackerman Road, Columbus, OH 43202, USA*

Abstract

A non-linear time-varying dynamic model is developed to study torsional dynamic behavior of a typical multi-mesh gear train. The physical system consists of M shafts ($M \geq 2$) coupled to each other by $M-1$ gear pairs. The discrete dynamic model includes the gear backlash clearance, gear mesh stiffness fluctuations, and torsional flexibilities of the shafts. In addition, the gear tooth modifications and typical manufacturing errors are included in the form of periodically time-varying displacement functions applied at gear meshes. A multi-term Harmonic Balance formulation is used in conjunction with discrete Fourier Transforms and a Parametric Continuation technique to obtain the steady-state period-n motions. Direct numerical integration results are used to demonstrate the accuracy of the harmonic balance predictions. Effects of key system parameters are also studied.

Keywords: Gear ;HBM; Multi-mesh; Time-varying; Discrete Fourier; Torsional;

Nomenclature

List of Symbols:

b	half length of backlash
c	damping coefficient
e	gear transmission error
f	external force
g	discontinuous displacement function
HBM	Harmonic Balance Method
I	polar mass moment of inertia
J	Jacobian matrix
k	gear mesh stiffness
M	Monodromy matrix
m	mass, frequency multiplier
p	relative gear mesh displacement
Q	number of discrete time points
q	discrete time interval
R	number of harmonic components considered in the solution
r	base radius
S	matrix form of non-linear algebraic equation set
T	torque
t	time
u	displacement harmonic amplitude
U	displacement vector
Z	number of gear teeth
δ	kronecker delta
Λ	dimensionless frequency
κ	dimensionless mesh stiffness
θ	rotational displacement
ω	frequency
Ω	nominal angular velocity
ζ	damping ratio

Subscripts:

c	characteristic quantity
eq	equivalent
i	gear or shaft index
i,n	natural mode I
m	mesh
s	shaft

Superscripts:

rms	root-mean-square value
T	matrix transpose

* Corresponding author. e-mail: alshyyab@hu.edu.jo

1. Introduction

Gear system dynamics has been a major research topic for the last two decades since both fatigue life and noise behavior of a gear set are impacted by its dynamic behavior. The dynamic response of the gear system shown in Figure 1 will be studied in this paper. The system is formed by M parallel shafts, coupled to each other by $M-1$ gear meshes formed by $2M-2$ gears. Input and output shafts are connected to rigid inertias representing prime mover (input) and output inertias, respectively. This configuration can be found in a wide range of automotive (manual, automatic and continuously variable transmissions), aerospace (rotorcraft drive trains), marine, wind turbine and industrial applications.

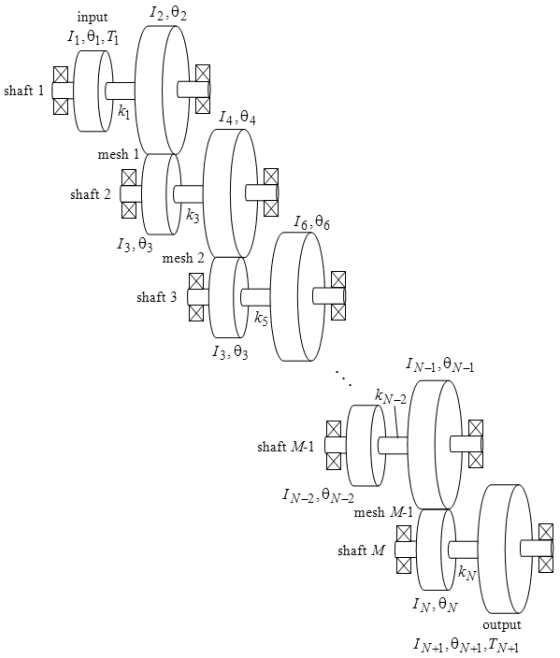

Figure 1: An M-shaft gear train configuration considered in this study

A number of dynamic models were proposed in the past to describe the dynamic behavior of multi-shaft gear system. Most of these models were linear time-invariant type as the gear backlash and mesh stiffness fluctuations were both ignored [1-10]. Such simplifications allowed a larger number of degrees of freedom to be included in the models since Eigen Value and Modal Summation formulations were suitable. Shaft and bearing flexibilities and combined transverse-torsional motions of gears were all included in these models to study larger scale gear-shaft-bearing systems. In some cases, the case deflections were also included in the form of a case stiffness matrix [10]. While these models offered guidelines towards the design of gear systems with favorable shaft and bearing arrangements, they brought limited insight to the behavior at the gear mesh. Another group of models [11-14] included the mesh stiffness fluctuations in the form of a parametric excitation while still assuming no tooth separations. These studies focused on the instabilities caused by parametric excitations and predicted primary and parametric resonances, resulting in regions of unstable motions with infinitely large amplitudes. These models as well were not capable of describing the non-linear behavior observed in recent experimental data [9,15-18] due to backlash-induced tooth separations.

Models of Kahraman and Blankenship [16,17] included both the gear backlash and mesh stiffness fluctuations on a single spur gear pair, and exhibited a softening type nonlinear behavior for a single gear pair due to apparent tooth separations. They also demonstrated that their single gear pair model correlates well with experimental data. Most recently, these authors [19,20] proposed a nonlinear time-varying dynamic model of the system shown in Figure 1 for a case of three shafts and two gear pairs. The system was reduced to a two degree of freedom definite model by using the relative gear mesh displacements as the coordinates and assuming rigid shafts. Dimensionless equations of motion were solved for the steady state period-1 motions [19] and period-n sub-harmonic motions [20] by using a multi-term Harmonic Balance method (HBM) in conjunction with discrete Fourier transforms and a parametric continuation scheme. These solutions were shown to compare well with the direct numerical integration solutions. Floquet theory was applied to determine the stability of the steady state solutions. An example gear train was used to investigate the influence of key system parameters including alternating mesh stiffness amplitudes, gear mesh damping, and torque transmitted.

These earlier models [19,20] were limited in several aspects: (i) they considered only a 3-shaft, 2-gear pair configuration, (ii) the torsional flexibilities of the shafts were not included in the model resulting in same vibration amplitudes for two gears mounted on the same shaft, and (iii) the input and output inertias were not included. This paper aims at generalizing these previous models [19,20] by considering any number of shafts, and including both the torsional shaft flexibilities and input/output inertias. The model will include $N+1$ inertia elements ($N+1$ degrees of freedom) where $N=2M-1$, with I_1 and I_{N+1} representing input and output inertias, respectively. The multi-term HBM that was used successfully for the three-shaft system [19,20] will be extended here as well as for the steady state periodic solutions of this M-shaft system including both period-1 and period-n sub-harmonic motions.

2. Dynamic Model Formulation

A dynamic model of a segment of the M-shaft gear train of in Figure 1 is shown in Figure 2. Equations of motion of the overall system are given as:

$$I_1\ddot{\theta}_1(t)+c_1\dot{\bar{p}}_1(t)+k_1\bar{p}_1(t)=T_1(t) \qquad (1a)$$

$$I_2\ddot{\theta}_2(t)-c_1\dot{\bar{p}}_1(t)-k_1\bar{p}_1(t)+r_2c_2\dot{\bar{p}}_2(t)+r_2k_2(t)\bar{g}_2(t)=0 \qquad (1b)$$

$$\vdots$$

$$I_N\ddot{\theta}_N(t)+c_N\dot{\bar{p}}_N(t)+k_N\bar{p}_N(t)+r_Nc_{N-1)}\dot{\bar{p}}_{(N-1)}(t)+r_{(N-1)}k_{(N-1)}(t)\bar{g}_{(N-1)}(t)=0 \qquad (1c)$$

$$I_{N+1}\ddot{\theta}_{N+1}(t)-c_N\dot{\bar{p}}_N(t)-k_N\bar{p}_N(t)=T_{N+1}(t) \qquad (1d)$$

where $N = 2M - 1$, an overdot denotes differentiation with respect to time $\bar{t}$, and

$$\bar{p}_n(\bar{t}) = \begin{cases} \theta_n(\bar{t}) - \theta_{n+1}(\bar{t}), & n = odd, \\ r_n\theta_n(\bar{t}) + r_{n+1}\theta_{n+1}(\bar{t}) + \bar{e}_n(\bar{t}), & n = even. \end{cases} \quad (2)$$

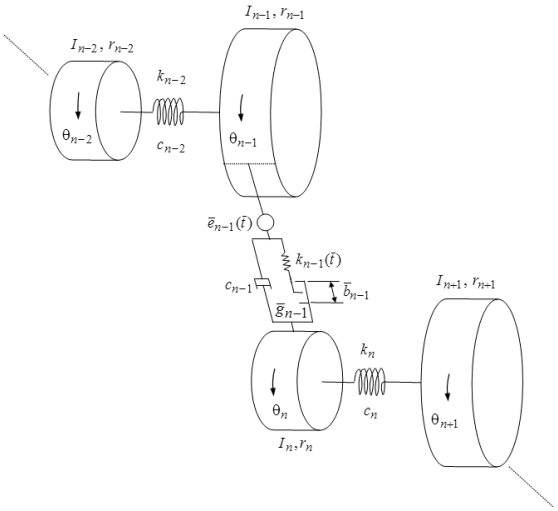

Figure 2: Torsional dynamic model of a segment of the the gear train shown in Figure 1

Here, $\bar{p}_n(\bar{t})$ with $n = odd$ represents torsional shaft deflections between two gears (or a gear and a rigid disk) and $\bar{p}_n(\bar{t})$ with $n = even$ represents relative displacements at a gear mesh formed by gear inertias n and $n+1$ along the line of action. r_n and r_{n+1} are the base circle radii of the gear pair formed by gears n and $n+1$. Torsional shaft flexibilities are represented by the torsional stiffness and damping coefficients, k_n and c_n ($n = odd$) as shown in Figure 2. The flexibility of a gear mesh is modeled by a periodically time-varying mesh stiffness $k_n(\bar{t})$ ($n = even$) that is subjected to a nonlinear displacement function $\bar{g}_n(\bar{t})$ representing the gear backlash clearance

$$\bar{g}_n(\bar{t}) = \begin{cases} \bar{p}_n(\bar{t}) - \bar{b}_n, & \bar{p}_n(\bar{t}) > \bar{b}_n \\ 0, & |\bar{p}_n(\bar{t})| \le \bar{b}_n \\ \bar{p}_n(\bar{t}) + \bar{b}_n, & \bar{p}_n(\bar{t}) < -\bar{b}_n \end{cases}, \quad n = even. \quad (3)$$

In addition, c_n and $2\bar{b}_n$ are the gear mesh damping coefficient and amount of backlash at the gear mesh n (formed by gear inertias n and $n+1$, $n = even$), respectively. Finally, $\bar{e}_n(\bar{t})$ in Figure 2 and equation (2) represents the so-called static transmission error excitation at the mesh of gears n and $n+1$ that accounts for intentional gear tooth profile modifications and manufacturing errors.

The system shown in Figure 2 is semi-definite with a zero-valued natural frequency. This rigid body mode can be eliminated by using $\bar{p}_n(\bar{t})$ as the coordinates. Also defining a characteristic length b_c and a characteristic frequency ω_c such that

$$p_n(\bar{t}) = \begin{cases} \bar{p}_n(\bar{t}), & n: odd, \\ \bar{p}_n(\bar{t})/b_c, & n: even, \end{cases} \qquad e_n(\bar{t}) = \bar{e}_n(\bar{t})/b_c \quad (4a,b)$$

and a dimensionless time $t = \omega_c\bar{t}$, dimensionless form of equations (1) can be written as

$$\ddot{p}_1(t) + 2\zeta_{11}\omega_{11}\dot{p}_1(t) - 2\zeta_{12}\omega_{12}\dot{p}_2(t) + \omega_{11}^2 p_1(t) - \omega_{12}^2\kappa_2(t)g_2(t) = f_1(t) \quad (5a)$$

$$\ddot{p}_2(t) - 2\zeta_{21}\omega_{21}\dot{p}_1(t) + 2\zeta_{22}\omega_{22}\dot{p}_2(t) + 2\zeta_{23}\omega_{23}\dot{p}_3(t) - \omega_{21}^2 p_1(t) + \omega_{22}^2\kappa_2(t)g_2(t) + \omega_{23}^2 p_3(t) = \ddot{e}_2(t) \quad (5b)$$

$$\ddot{p}_n + 2\zeta_{n(n-1)}\omega_{n(n-1)}\dot{p}_{(n-1)} + 2\zeta_{nn}\omega_{nn}\dot{p}_n - 2\zeta_{n(n+1)}\omega_{(n)(n+1)}\dot{p}_{(n+1)} + \omega_{n(n-1)}^2\kappa_{(n-1)}(t)g_{(n-1)} + \omega_{nn}^2 p_n - \omega_{n(n+1)}^2\kappa_{(n+1)}(t)g_{(n+1)} = 0, \quad n = 3,5,\cdots,N-3 \quad (5c)$$

$$\ddot{p}_n - 2\zeta_{n(n-1)}\omega_{n(n-1)}\dot{p}_{(n-1)} + 2\zeta_{nn}\omega_{nn}\dot{p}_n + 2\zeta_{n(n+1)}\omega_{n(n+1)}\dot{p}_{(n+1)} - \omega_{n(n-1)}^2 p_{(n-1)} + \omega_{nn}^2\kappa_n(t)g_n + \omega_{n(2n+1)}^2 p_{(n+1)} = \ddot{e}_n(t), \quad n = 4,6,\ldots,N-2 \quad (5d)$$

$$\ddot{p}_N(t) + 2\zeta_{N(N-1)}\omega_{N(N-1)}\dot{p}_{(N-1)}(t) + 2\zeta_{NN}\omega_{NN}\dot{p}_N(t) + \omega_{N(N-1)}^2\kappa_{(N-1)}(t)g_{(N-1)}(t) + \omega_{NN}^2 p_N(t) = f_N(t). \quad (5e)$$

Here, dimensionless mesh stiffness functions are defined as $\kappa_n(\bar{t}) = 1 + \hat{k}_n(\bar{t})/\bar{k}_n$ ($n = even$) where $\bar{k}_n$ and $\hat{k}_n(\bar{t})$ are the mean and alternating components, respectively. An overdot denotes derivative with respect to *t*. The other dimensionless parameters are defined as:

$$f_1(t) = T_1(t)/(\omega_c^2 I_1), \; f_N(t) = T_{N+1}(t)/(\omega_c^2 I_{N+1}), \quad (6a,b)$$

$$g_n(t) = \begin{cases} \bar{g}_n(t), & n = odd, \\ \bar{g}_n(t)/b_c, & n = even, \end{cases} \quad (6c)$$

$$\omega_{n(n-1)}^2 = \begin{cases} \dfrac{r_n\bar{k}_{n-1}b_c}{I_n\omega_c^2}, & n = odd, \\ \dfrac{r_n\bar{k}_{n-1}}{I_n\omega_c^2 b_c}, & n = even, \end{cases}$$

$$\omega_{nn}^2 = \begin{cases} \left(\dfrac{1}{I_n} + \dfrac{1}{I_{n+1}}\right)\dfrac{\bar{k}_n}{\omega_c^2}, & n = odd, \\ \left(\dfrac{r_n^2}{I_n} + \dfrac{r_{n+1}^2}{I_{n+1}}\right)\dfrac{\bar{k}_n}{\omega_c^2}, & n = even, \end{cases} \quad (6d,e)$$

$$\omega_{n(n+1)}^2 = \begin{cases} \dfrac{r_{n+1}\bar{k}_{n+1}b_c}{I_{n+1}\omega_c^2}, & n = odd, \\ \dfrac{r_{n+1}\bar{k}_{n+1}}{I_{n+1}\omega_c^2 b_c}, & n = even, \end{cases}$$

$$\zeta_{n(n-1)}=\begin{cases}\dfrac{r_n c_{n-1} b_c}{2I_n \omega_{n(n-1)} \omega_c}, & n=odd,\\ \dfrac{r_n c_{n-1}}{2I_n \omega_{n(n-1)} \omega_c b_c}, & n=even,\end{cases} \qquad (6f,g)$$

$$\zeta_{nn}=\begin{cases}\frac{1}{2}(\dfrac{1}{I_n}+\dfrac{1}{I_{n+1}})\dfrac{c_n}{\omega_{nn}\omega_c}, & n=odd,\\ \frac{1}{2}(\dfrac{r_n^2}{I_n}+\dfrac{r_{n+1}^2}{I_{n+1}})\dfrac{c_n}{\omega_{nn}\omega_c}, & n=even,\end{cases}$$

$$\zeta_{n(n+1)}=\begin{cases}\dfrac{r_{n+1} c_{n+1} b_c}{2I_{n+1}\omega_c\,\omega_{n(n+1)}}, & n=odd,\\ \dfrac{r_{n+1} c_{n+1}}{2I_{n+1}\omega_c\,\omega_{n(n+1)} b_c}, & n=even.\end{cases} \qquad (6h,i)$$

3. Multi-term Harmonic Balance Solution

The multi-term Harmonic Balance method is based on the assumption that the external excitations $f_n(t)$ and $e_n(t)$, time-varying coefficients $\kappa_n(t)$, the steady-state solutions $p_n(t)$ and nonlinear functions $g_n(t)$ are all periodic. These functions are given in Fourier series form as:

$$\kappa_n(t)=1+\sum_{h=1}^{K}[\kappa_{2h}^{(n)}\cos(hm_n\Lambda t)+\kappa_{2h+1}^{(n)}\sin(hm_n\Lambda t)], \quad n=even, \qquad (7a)$$

$$e_n(t)=E_1^{(n)}+\sum_{r=1}^{\Gamma}[E_{2r}^{(n)}\cos(rm_n\Lambda t)+E_{2r+1}^{(n)}\sin(rm_n\Lambda t)], \quad n=even, \qquad (7b)$$

$$f_n(t)=f_1^{(n)}+\sum_{\ell=1}^{L}[f_{2\ell}^{(n)}\cos(\ell\Lambda t)+f_{2\ell+1}^{(n)}\sin(\ell\Lambda t)], \quad n=1,2\ldots,N, \qquad (7c)$$

$$p_n=u_1^{(n)}+\sum_{r=1}^{R}[u_{2r}^{(n)}\cos(\frac{r\Lambda t}{\eta})+u_{2r+1}^{(n)}\sin(\frac{r\Lambda t}{\eta}),\qquad n=1,2,\ldots,N \qquad (7d)$$

$$g_n=v_1^{(n)}+\sum_{r=1}^{R}[v_{2r}^{(n)}\cos(\frac{r\Lambda t}{\eta})+v_{2r+1}^{(n)}\sin(\frac{r\Lambda t}{\eta}), \quad n=even \qquad (7e)$$

Here, $\Lambda=Z\Omega/\omega_c$ is the fundamental dimensionless frequency of the stiffness (tooth pass frequency) of a chosen gear mesh, where Z and Ω are the number of teeth and rotational frequency of one of the gears forming the mesh, and the integer multipliers m_n ($n=even$) are defined to include commensurate stiffness frequency ratios of the various gear meshes. In equation (7d), $\mathbf{u}=[u_1^{(1)}\ u_{2r}^{(1)}\ u_{2r+1}^{(1)}\ \cdots, u_1^{(n)},\ u_{2r}^{(n)},\ u_{2r+1}^{(n)}\ \cdots\ u_1^{(N)}\ u_{2r}^{(N)}\ u_{2r+1}^{(N)}]^T$ are unknown coefficients of the assumed solution, and η is the sub-harmonic index required to find sub-harmonic motions. Defining $\theta=\Lambda t/\eta$, substituting equations (7) into equation (6), and enforcing harmonic balance, the following set of $N(2R+1)$ non-linear coupled nonlinear algebraic equations are obtained:

$$\mathbf{S}(\mathbf{u},\mathbf{v},\Lambda)=\mathbf{0} \qquad (8)$$

where vectors **u**, **v** and **S** have dimension $N(2R+1)$. For $n=odd$, the elements of **S** vector are given as ($r\in[1,R]$)

$$S_1^{(n)}=\omega_{n(n-1)}^2[v_1^{(n-1)}+\tfrac{1}{2}\sum_{h=1}^{H}\varphi_h^{(n-1)}]+\omega_{nn}^2u_1^{(n)}-\omega_{n(n+1)}^2[v_1^{(n+1)}+\frac{1}{2}\sum_{h=1}^{H}\varphi_h^{(n+1)}]-f_1^{(n)}, \qquad (9a)$$

$$\begin{aligned}S_{2r}^{(n)}=&-(\frac{r\Lambda}{\eta})^2u_{2r}^{(n)}+2\zeta_{n(n-1)}\omega_{n(n-1)}\frac{r\Lambda}{\eta}u_{2r+1}^{(n-1)}\\&+2\zeta_{nn}\omega_{nn}\frac{r\Lambda}{\eta}u_{2r+1}^{(n)}-2\zeta_{n(n+1)}\omega_{(n)(n+1)}\frac{r\Lambda}{\eta}u_{2r+1}^{(n+1)}\\&+\omega_{nn}^2u_{2r}^{(n)}-f_{2r/\eta}^{(n)}+\omega_{n(n-1)}^2[\Phi_{2r}^{(n-1)}\\&+\frac{1}{2}\sum_{h=1}^{H}(\kappa_{2h}^{(n-1)}\psi 2_{rh}^{(n-1)}+\kappa_{2h+1}^{(n-1)}\psi 1_{rh}^{(n-1)})]\\&-\omega_{n(n+1)}^2[\Phi_{2r}^{(n+1)}+\frac{1}{2}\sum_{h=1}^{H}(\kappa_{2h}^{(n+1)}\psi 2_{rh}^{(n+1)}+\kappa_{2h+1}^{(n+1)}\psi 1_{rh}^{(n+1)})],\end{aligned} \qquad (9b)$$

$$\begin{aligned}S_{2r+1}^{(n)}=&-(\frac{r\Lambda}{\eta})^2u_{2r+1}^{(n)}-2\zeta_{n(n-1)}\omega_{n(n-1)}\frac{r\Lambda}{\eta}u_{2r}^{(n-1)}\\&-2\zeta_{nn}\omega_{nn}\frac{r\Lambda}{\eta}u_{2r}^{(n)}+2\zeta_{n(n+1)}\omega_{(n)(n+1)}\frac{r\Lambda}{\eta}u_{2r}^{(n+1)}\\&+\omega_{nn}^2u_{2r+1}^{(n)}-f_{2r+1}^{(n)}\\&+\omega_{n(n-1)}^2[\Phi_{2r+1}^{(n-1)}+\frac{1}{2}\sum_{h=1}^{H}((\kappa_{2h}^{(n-1)}\psi 3_{rh}^{(n-1)}+\kappa_{2h+1}^{(n-1)}\psi 4_{rh}^{(n-1)})]\\&-\omega_{n(n+1)}^2[\Phi_{2r+1}^{(n+1)}+\frac{1}{2}\sum_{h=1}^{H}((\kappa_{2h}^{(n+1)}\psi 3_{rh}^{(n+1)}+\kappa_{2h+1}^{(n+1)}\psi 4_{rh}^{(n+1)})].\end{aligned} \qquad (9c)$$

For $n=even$, the elements of **S** are given as ($r\in[1,R]$)

$$S_1^{(n)}=-\omega_{n(n-1)}^2u_1^{(n-1)}+\omega_{n(n+1)}^2u_1^{(n+1)}+\omega_{nn}^2[v_1^{(n)}+\frac{1}{2}\sum_{h=1}^{H}\varphi_h^{(n)}], \qquad (9d)$$

$$\begin{aligned}S_{2r}^{(n)}=&-(\frac{r\Lambda}{\eta})^2u_{2r}^{(n)}+(\frac{r\Lambda}{\eta})^2E_{2(r/m_n\eta)}^{(n)}-2\zeta_{n(n-1)}\omega_{n(n-1)}\frac{r\Lambda}{\eta}u_{2r+1}^{(n-1)}\\&+2\zeta_{nn}\omega_{nn}\frac{r\Lambda}{\eta}u_{2r+1}^{(n)}+2\zeta_{n(n+1)}\omega_{n(n+1)}\frac{r\Lambda}{\eta}u_{2r+1}^{(n+1)}-\omega_{n(n-1)}^2u_{2r}^{(n-1)}\\&+\omega_{n(n+1)}^2u_{2r}^{(n+1)}+\omega_{nn}^2[\Phi_{2r}^{(n)}+\frac{1}{2}\sum_{h=1}^{H}(\kappa_{2h}^{(n)}\psi 2_{rh}^{(n)}+\kappa_{2h+1}^{(n)}\psi 1_{rh}^{(n)})],\end{aligned} \qquad (9e)$$

$$\begin{aligned}S_{2r+1}^{(n)}=&-(\frac{r\Lambda}{\eta})^2u_{2r+1}^{(n)}+(\frac{r\Lambda}{\eta})^2E_{2(r/m_n\eta)+1}^{(n)}+2\zeta_{n(n-1)}\omega_{n(n-1)}\frac{r\Lambda}{\eta}u_{2r}^{(n-1)}\\&-2\zeta_{nn}\omega_{nn}\frac{r\Lambda}{\eta}u_{2r}^{(n)}-2\zeta_{n(n+1)}\omega_{n(n+1)}\frac{r\Lambda}{\eta}u_{2r}^{(n+1)}-\omega_{n(n-1)}^2u_{2r+1}^{(n-1)}\\&+\omega_{n(n+1)}^2u_{2r+1}^{(n+1)}+\omega_{nn}^2[\Phi_{2r+1}^{(n)}+\frac{1}{2}\sum_{h=1}^{H}(\kappa_{2h}^{(n)}\psi 3_{rh}^{(n)}+\kappa_{2h+1}^{(n)}\psi 4_{rh}^{(n)})].\end{aligned} \qquad (9f)$$

In equations for $S_i^{(1)}$ and $S_i^{(N)}$, $i\in(1,2R+1)$, the terms having indices less than one or larger than N, respectively, must be omitted. In addition, parameters ψi, φ and Φ in equations (9) are defined below

$$\psi 1_{rh}^{(n)} = v_{2(h\eta m_n - r)+1}^{(n)} + v_{2(h\eta m_n + r)+1}^{(n)} - v_{2(r-h\eta m_n)+1}^{(n)}, \quad (10a)$$

$$\psi 2_{rh}^{(n)} = v_{2(h\eta m_n - r)}^{(n)} + v_{2(h\eta m_n + r)}^{(n)} + v_{2(r-h\eta m_n)}^{(n)}, \quad (10b)$$

$$\psi 3_{rh}^{(n)} = -v_{2(h\eta m_n - r)+1}^{(n)} + v_{2(h\eta m_n + r)+1}^{(n)} + v_{2(r-h\eta m_n)+1}^{(n)}, \quad (10c)$$

$$\psi 4_{rh}^{(n)} = v_{2(h\eta m_n - r)}^{(n)} - v_{2(h\eta m_n + r)}^{(n)} + v_{2(r-h\eta m_n)}^{(n)}, \quad (10d)$$

$$\varphi_h^{(n)} = \kappa_{2(h/\eta m_n)}^{(n)} v_{2h}^{(n)} + \kappa_{2(h/\eta m_n)+1}^{(n)} v_{2h+1}^{(n)}, \quad (10e)$$

$$\Phi_{2r}^{(n)} = v_{2r}^{(n)} + v_1^{(n)} \kappa_{2(r/\eta m_n)}^{(n)},$$

$$\Phi_{2r+1}^{(n)} = v_{2r+1}^{(n)} + v_1^{(n)} \kappa_{2(r/\eta m_n)+1}^{(n)} \quad (10f,g)$$

In later steps, the selection of Λ as a control parameter to solve for the elements of $\mathbf{u}$ using Newton-Raphson iteration method poses difficulties The determinant of the Jacobian matrix also approaches zero near the bifurcation points. This can be avoided by switching to another unknown as the control parameter, leaving the dimensionless frequency Λ and the other elements of the solution vector $\mathbf{u}$ as unknowns to be determined. In order to implement this, $\mathbf{u}$ is expanded to $\mathbf{U} = [\mathbf{u}^T, u_{2R+2)}^{(N)}]^T$ where $u_{2R+2)}^{(N)} = \Lambda$. Accordingly, the following dummy equation is added to equation (9)

$$S_{2R+2}^{(N)} = u_j^{(i)} - u^* \quad (11)$$

where $u_j^{(i)} = u_{2R+2)}^{(N)} = \Lambda$ or the values of the indices $j \in [1, 2R+1]$ and $i \in [1, N]$ define which element is chosen as a control parameter, and u^* is a numerical value prescribed to the control parameter .

The coefficients of the nonlinear displacement functions $v_i^{(n)}$ are represented in terms of $u_i^{(n)}$ and $u_{2R+2}^{(N)}$ ($n \in [1, N]$, $i \in [1, 2R+1]$) by using Discrete Fourier transforms. The values of the $p_n(t)$ and $g_n(t)$ at the discrete time $t = q\rho$ ($q \in [0, Q-1]$) are given as

$$p_{nq} = u_1^{(n)} + \sum_{r=1}^{R} [u_{2r}^{(n)} \cos(\frac{2\pi rq}{Q}) + u_{2r+1}^{(n)} \sin(\frac{2\pi rq}{Q})], \quad (12a)$$

$$g_{nq} = \begin{cases} p_{nq}(t) - b_n, & p_{nq}(t) > b_n \\ 0, & |p_{nq}(t)| \le b_n \\ p_{nq}(t) + b_n, & p_{nq}(t) < -b_n \end{cases} \quad n = even. \quad (12b)$$

Here, $\rho = (2\pi\eta / Q\Lambda)$ where Q is the total number of the discrete points. The coefficients of $g_n(t)$ are determined by using the inverse Fourier transforms such that ($r \in [1, R]$)

$$v_1^{(n)} = \frac{1}{Q} \sum_{q=0}^{Q-1} g_{nq},$$

$$v_{2r}^{(n)} = \frac{2}{Q} \sum_{q=0}^{Q-1} g_{nq} \cos(\frac{2\pi rq}{Q}),$$

$$v_{2r+1}^{(n)} = \frac{2}{Q} \sum_{q=0}^{Q-1} g_{nq} \sin(\frac{2\pi rq}{Q}) \quad (13a\text{-}c)$$

These $v_i^{(n)}$ values and the Newton-Raphson recurrence formula

$$\mathbf{U}^{(m)} = \mathbf{U}^{(m-1)} - [\mathbf{J}^{-1}]^{(m-1)} \mathbf{S}^{(m-1)} \quad (14)$$

are used to solve equations (9) for $\mathbf{U}$, where $\mathbf{U}^{(m-1)}$ and $\mathbf{U}^{(m)}$ are the previous and the current iteration values of the vector $\mathbf{U}$, respectively, and $[\mathbf{J}^{-1}]^{(m-1)}$ is the inverse of the Jacobian matrix of the vector $\mathbf{S}$ estimated at the previous point $(m-1)$. Elements of the Jacobian matrix $\mathbf{J}$ for this model are defined in Appendix A. The Floquet theory is used to determine the stability of the steady-state motions as describe in reference [19].

4. Results

A three-shaft gear train (6-DOF semi-definite model) is considered as the example system. It consists of two gear pairs of identical dimensionless parameters connected to each other and to the prime mover and load inertias via torsionally flexible shafts. The dimensionless parameters are calculated by using equations (6) and the dimensional parameters listed in Table 1.

Table 1. Dimensional parameters of the example gear pair

Parameter	Gear 1	Gear 2	Gear 3	Gear 4
Base circle radius, m	0.05	0.10	0.05	0.10
Mass, kg	1.85	7.4	3.7	14.81
Inertia, kg – m^2	0.0023	0.037	0.0046	0.074
Average mesh stiffness, N/m	$2.5(10)^8$		$5(10)^8$	
Mesh damping coefficient, N-s/m	1360		2720	
Torsional stiffness of the input and output shafts, N-m/rad	$1.0(10)^3$			
Shaft damping ratios	0.01			
Input inertia, kg – m^2	$2.30(10)^{-7}$			
Output inertia, kg – m^2	$2.30(10)^{-7}$			

In order to limit the size of the parameter study, mostly harmonic mesh stiffness functions with amplitude $\kappa_2^{(2)} = \kappa_4^{(2)} = 0.3$ are considered ($K = 1$ in equation (7)).

This corresponds to a spur gear pair with an involute contact ratio value of 1.7. A constant external input torque of $T_1 = 150$ *N-m* ($L = 0$ in equation (7)) corresponding to $f_1(t) = f_1^{(1)} = 11{,}000$ and $f_5(t) = f_1^{(5)} = 4 f_1^{(1)}$ is considered. All gears are assumed to be free of profile errors so that all $e_i(t) = 0$. A characteristic length of $\bar{b}_c = 30\,\mu m$ is considered that represents half magnitude of the gear backlash so that $b_1 = b_2 = 1.0$. A characteristic frequency $\omega_c = 9{,}870$ rad/s is used. In addition, the fundamental mesh frequencies of both gear pairs are considered equal ($m_2 = m_4 = 1$) unless specified. The values of the mesh damping coefficients $\bar{c}_i$ ($i = 2, 4$) in Table 1 are such that

they correspond to a damping ratio of ζ_m=0.05, given $c_i = 2\zeta_m\sqrt{k_{i,m}m_{i,i+1}}$ where $m_{i,i+1} = I_i I_{i+1}/(r_i^2 I_{i+1} + r_{i+1}^2 I_i)$. Similarly, the values of shaft damping coefficient $\bar{c}_i$ ($i = 1,3,5$) correspond to a shaft damping ratio of ζ_s=0.01.

The results in the following sections will be presented in the form of $p_2^{(rms)}$ and $p_4^{(rms)}$ versus the dimensionless frequency Λ. Here $p_i^{(rms)}$ is the root-mean-square (rms) amplitude to $p_i(t)$ defined as $p_i^{(rms)} = \{\sum_{r=1}^{R}[A_r^{(i)}]^2\}^{1/2}$ where $A_r^{(i)} = \{[u_{2r}^{(i)}]^2 + [u_{2r+1}^{(i)}]^2\}^{1/2}$ is the r-th harmonic amplitude. $p_2^{(rms)}$ and $p_4^{(rms)}$ are of primary interest here since these parameters represent gear mesh displacements that are directly proportional to dynamic gear mesh forces.

4.1. Multi-term Harmonic Balance versus Numerical Integration

Figure 3 shows period-1 ($\eta = 1$ in equation (7)) HBM solution $p_2^{(rms)}$ and $p_4^{(rms)}$ as a function of Λ for a system having $\kappa_2^{(2)} = \kappa_2^{(4)} = 0.3$, $f_1^{(1)} = 11000$, and $k_3 = 1.0(10)^8$ N-m/rad. The thick and thin solid lines denote the stable and unstable harmonic balance motions for $R = 6$. Figure 3 also shows the stable and unstable HBM solutions for the corresponding linear time-varying system ($b_1 = b_2 = 0$) as thick and thin dashed lines, respectively. In addition, the direct numerical integration results for both nonlinear and linear systems are represented by square symbols. As shown in Figure 3, the 6-term HBM solutions match well with the numerical integration solutions for both the nonlinear and linear cases. The range of Λ includes primary resonances at $\Lambda = \omega_{a,n} = 0.96$ and $\Lambda = \omega_{b,n} = 1.86$ as well as a super-harmonic resonance $\Lambda = \omega_{an}/2 = 0.48$, where $\omega_{a,n}$ and $\omega_{b,n}$ are two of the natural frequencies.

Both the nonlinear and the corresponding linear models result in the same vibration amplitudes at frequencies where tooth contact is maintained all the time and hence, the gear backlash nonlinearity is not a factor. As Λ approaches natural frequencies $\omega_{a,n} = 0.96$ and $\omega_{b,n} = 1.86$, primary resonances with characteristic softening-type nonlinear curves are obtained. This is solely because the teeth loose contact during a portion of the meshing cycle [19,20]. The softening upper branch of the primary resonance at $\omega_{a,n} = 0.96$ also exhibits a hardening type curve sloped to the right. This corresponds to the back collisions (contact at the unloaded tooth flank) in addition to tooth separations, which is more clear for $p_4^{(rms)}$. It is also noted in Figure 3 is that there is a range of Λ in which no stable period-1 motions are found. This corresponds to the parametric resonance at $\Lambda = 2\omega_{a,n}$. As it will be illustrated later, this range is dictated by period-2 sub-harmonic motions.

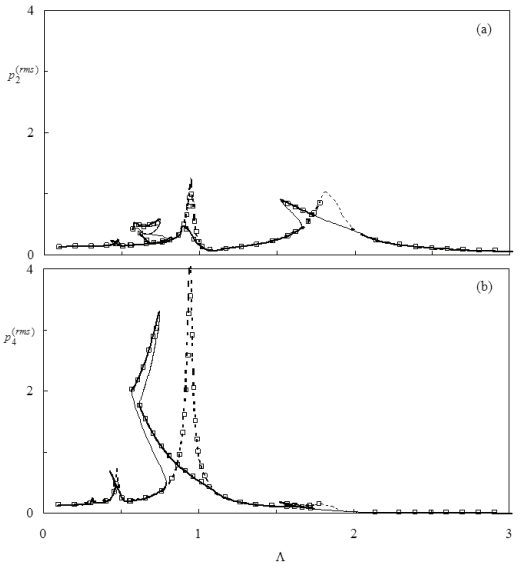

Figure 3: Comparison of period-1 multi-term HBM ($R = 6$) and numerical integration results for $K = 1$, $\kappa_2^{(2)} = \kappa_2^{(4)} = 0.3$, $f_1^{(1)} = 11{,}000$, and $k_3 = 10^8$ N-m/rad. (—) Stable and (——) unstable solutions of the nonlinear model, (- - -) stable and (- - -) unstable solutions of the corresponding linear model, and (□) numerical integration solutions. (a) $p_2^{(rms)}$ and (b) $p_4^{(rms)}$

4.2. Influence of Torsional Shaft Flexibility

In Figure 4, effect of k_3 on period-1 $p_i^{(rms)}$ is illustrated. In order to understand this figure better, the variation of the natural frequencies of the corresponding linear time-invariant system are plotted in Figure 5 against the torsional stiffness k_3 of the shaft connecting the gear pairs to each other.

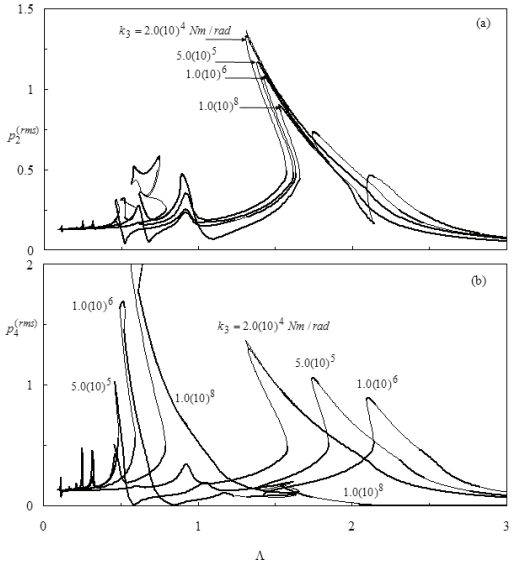

Figure 4: Influence of the shaft stiffness k_3 on period-1 HBM solutions for $K = 1$, $\kappa_2^{(2)} = \kappa_2^{(4)} = 0.3$ and $f_1^{(1)} = 11{,}000$; (a) $p_2^{(rms)}$ and (b) $p_4^{(rms)}$. (—) Stable and (——) unstable HBM solutions

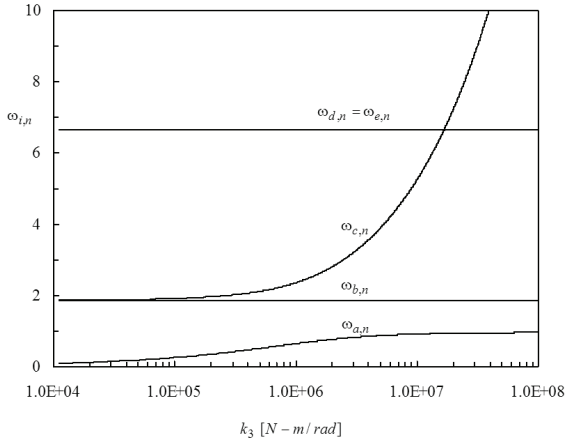

Figure 5: Variation of natural frequencies $\omega_{i,n}$ ($i = a,b,\ldots,e$) of the corresponding linear time-invariant system with k_3

Two of the natural frequencies are $\omega_{d,n} = \omega_{e,n} = 6.65$ regardless of the value of k_3. For the system defined in Table 1, these modes are dominated by the deflections of the shafts connecting the prime mover and load inertias to the respective gears and $\omega_{d,n} \approx \sqrt{k_1 / I_1}/\omega_c$ and $\omega_{e,n} \approx \sqrt{k_5 / I_6}/\omega_c$ where k_1 and k_5 are torsional stiffnesses of these shafts, and I_1 and I_6 are the inertias of the prime mover and the load. For smaller values of k_3, say $k_3 < 10^5$ N-m/rad, the two gear pairs are dynamically uncoupled and each gear pair acts independently as single gear pairs. In this case, $\omega_{a,n} \approx 0$, $\omega_{b,n} \approx \sqrt{\bar{k}_4 / m_{34}}/\omega_c$ and $\omega_{c,n} \approx \sqrt{\bar{k}_2 / m_{12}}/\omega_c$, where m_{12} and m_{34} are equivalent masses of the first and second gear pairs, and $\bar{k}_2$ and $\bar{k}_4$ are the average mesh stiffness values. Since both gear pairs of the example system have the same dimensionless parameters, $\omega_{b,n} \approx \omega_{c,n} \approx 1.86$ for small values of k_3. On the other hand, for $k_3 > 10^8$ N-m/rad, the two gear pairs are connected almost rigidly and $\omega_{a,n} = 0.96$ and $\omega_{b,n} = 1.86$ while $\omega_{c,n}$ is clearly outside that frequency range of interest ($\Lambda \in [0,3]$). Finally, at intermediate shaft stiffness values, say $k_3 = 5(10)^5$, all three natural frequencies $\omega_{a,n}$, $\omega_{b,n}$ and $\omega_{c,n}$ are non-zero and within the frequency range considered. Therefore, resonance peaks should be expected at these frequencies. Figure 4 considers four different k_3 values, $2(10)^4$ N-m/rad (very soft), $5(10)^5$ and 10^6 N-m/rad (intermediate), and 10^8 N-m/rad. (very stiff). When $k_3 = 2(10)^4$ N-m/rad, the two gear pairs are dynamically uncoupled, and since both gear pairs of the example system have identical dimensionless parameters, $p_2^{(rms)} = p_4^{(rms)}$ both having primary resonance peaks at $\omega_{b,n} \approx \omega_{c,n} = 1.86$. On the other hand, a stiffness value of $k_3 = 10^8$ N-m/rad is large enough to provide an almost rigid connection between gears 2 and 3 such that $\theta_3(t) \approx \theta_4(t)$. According to Figure 4, the first gear mesh natural frequency is approximately twice the second natural frequency $\omega_{b,n} \approx 2\omega_{a,n} = 1.86$. As a result, two primary resonances at $\Lambda = \omega_{a,n} = 0.96$ and $\Lambda = \omega_{b,n} = 1.86$ as well as a super-harmonic resonance $\Lambda = \omega_{a,n} / 2 = 0.48$ are evident in Figure 4 when $k_3 = 10^8$ N-m/rad. For the other two values $k_3 = 5(10)^5$ and 10^6 N-m/rad, the primary resonances are observed at $\Lambda \approx \omega_{a,n}$, $\Lambda \approx \omega_{b,n}$ and $\Lambda \approx \omega_{c,n}$. The $p_4^{(rms)}$ resonances are more significant at $\Lambda \approx \omega_{a,n}$ and $\Lambda \approx \omega_{c,n}$ while $p_2^{(rms)}$ exhibits a large softening-type resonance near $\Lambda \approx \omega_{b,n}$. Super-harmonic peaks at one-half of the natural frequencies are also present. In addition, the period-1 solutions are unstable in certain Λ ranges, most of which correspond to the parametric instabilities due the gear mesh stiffness fluctuations.

4.3. Influence of Other System Parameters

Influence of the mean force transmitted by the gear train on the steady state period-1 response is shown in Figure 6. The values of the constant dimensionless forces $f_1^{(5)} = 4 f_1^{(1)}$, where $f_1^{(1)}$=11,000, 7400 and 3700 correspond to input torque values of $T_1 = 150$, 100 and 50 N-m, respectively. The response curves are in agreement with previous observations on single gear pairs [15,16,17], and three-shaft system results [19,20]. Increasing the constant torque applied does not prevent tooth separations from occurring. Larger $f_1^{(1)}$ and $f_1^{(5)}$ values result in higher amplitudes of $p_2^{(rms)}$ and $p_4^{(rms)}$. The primary resonant peak at $\omega_{a,n} \approx 0.96$ exhibits only a softening type behavior for $f_1^{(1)} = 3{,}700$ while the amplitudes are significantly larger for the other two torque values to initiate back collisions and a hardening type curve following the typical softening behavior.

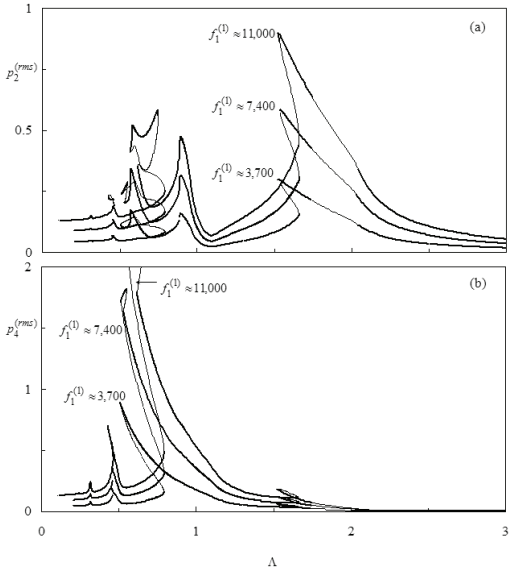

Figure 6: Influence of mean load transmitted on period-1 HBM solutions for $K = 1$, $\kappa_2^{(2)} = \kappa_2^{(4)} = 0.3$ and $k_3 = 10^8$ N-m/rad; (—) Stable and (——) unstable HBM solutions. (a) $p_2^{(rms)}$ and (b) $p_4^{(rms)}$

Likewise, the super-harmonic resonance amplitudes at $\Lambda = \omega_{a,n} / 2 = 0.48$ in Figure 6(b) and at $\Lambda = \omega_{b,n} / 2 = 0.93$ in Figure 6(a) are increased significantly when the torque

is increased. The parametric instability regions near $\Lambda = 2\omega_{a,n}$ and the jump-up frequencies are not influenced by the values of $f_1^{(1)}$ and $f_1^{(5)}$ values. Figure 7 illustrates the influence of the gear mesh stiffness amplitudes on period-1 motions. The mesh stiffness harmonic amplitudes of a spur gear pair depend primarily on the involute contact ratio (a parameter representing the average number of engaged tooth pairs). Four values of harmonic mesh stiffness amplitudes $\kappa_2^{(2)} = \kappa_4^{(2)} = 0.42$, 0.3, 0.2 and 0.1 are considered in Figure 7 corresponding to involute contact ratios of 1.5, 1.7, 1.8 and 1.9, respectively. In this figure, the mesh stiffness amplitudes appear to influence the period-1 response in several ways. (i) Increased $\kappa_2^{(2)} = \kappa_4^{(2)}$ values result in increased response amplitudes as well. This influence is more significant than the one shown in Figure 6 as not only the amplitudes but also the degree of nonlinear behavior is influenced. When $\kappa_2^{(2)} = \kappa_4^{(2)}$ values are low, say 0.1, a minor softening type resonance peak is observed near $\Lambda = \omega_{a,n} = 0.96$ in Figure 7(a) while the primary resonance peak near $\Lambda = \omega_{b,n} = 1.86$ is linear. For $\kappa_2^{(2)} = \kappa_4^{(2)} = 0.2$, both primary resonance peaks become non-linear (tooth separations). For $\kappa_2^{(2)} = \kappa_4^{(2)} \geq 0.3$, back collisions are also initiated near $\Lambda = \omega_{a,n} = 0.96$. (ii) The super-harmonic resonances at $\Lambda = \omega_{a,n}/2 = 0.48$ in Figure 7(b) and at $\Lambda = \omega_{b,n}/2 = 0.93$ in Figure (7a) become significantly larger when $\kappa_2^{(2)} = \kappa_4^{(2)}$ is increased. (iii) Larger $\kappa_2^{(2)} = \kappa_4^{(2)}$ amplitudes are observed to enhance the parametric resonances as well. While there is no unstable region of period-1 motions for $\kappa_2^{(2)} = \kappa_4^{(2)} = 0.1$, a wide band of unstable motions is observed for $\kappa_2^{(2)} = \kappa_4^{(2)} = 0.42$ within $\Lambda \in [1.65, 2.15]$.

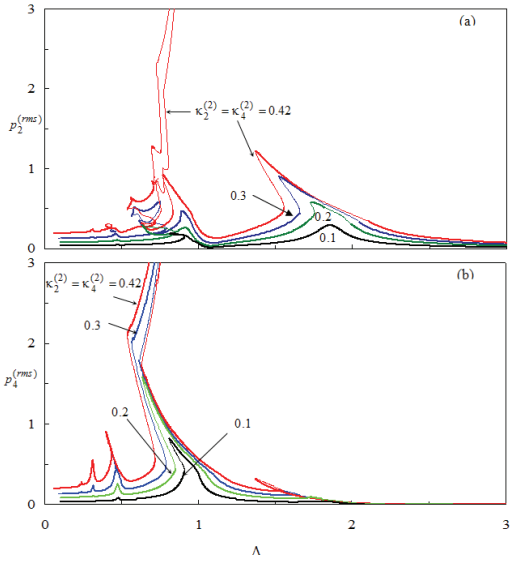

Figure 7: Influence of harmonic mesh stiffness amplitude on period-1 HBM solutions for $k_3 = 10^8$ N-m/rad and $f_1^{(1)} = 11{,}000$; (—) Stable and (——) unstable HBM solutions. (a) $p_2^{(rms)}$ and (b) $p_4^{(rms)}$

Next, higher harmonic amplitudes of the periodic mesh stiffness functions in equation (7a) are also considered to illustrate their influence on the steady-state period-1 motions. In Fig.(8), the five Fourier harmonics of the mesh stiffness functions $\kappa_2(t)$ & $\kappa_4(t)$ are considered to represent an involute contact ratio of 1.5. It was shown in reference [18] that a mesh stiffness function could be approximated to a rectangular waveform which becomes a square wave for an involute contact ratio of 1.5. In this case, even harmonic amplitudes are zero and the first three non-zero harmonics are $\kappa_2^{(2)} = \kappa_2^{(4)} = 0.42$, $\kappa_6^{(2)} = \kappa_6^{(4)} = -0.141$, & $\kappa_{10}^{(2)} = \kappa_{10}^{(4)} = -0.085$ ($K = 5$ in equation (7). In this case, the rms response curves exhibit not only the primary resonances near $\Lambda = \omega_{a,n}$ and $\Lambda = \omega_{b,n}$ and super-harmonic resonance near $\Lambda = \omega_{a,n}/2$ and $\Lambda = \omega_{b,n}/2$ as discussed earlier, but also additional resonance peaks at $\Lambda = \frac{1}{3}\omega_{a,n}, \frac{1}{3}\omega_{b,n}, \frac{1}{5}\omega_{a,n}$ and $\frac{1}{5}\omega_{b,n}$ due to the higher harmonic terms of the mesh stiffness ($\kappa_6^{(2)} = \kappa_6^{(4)} = -0.141$ and $\kappa_{10}^{(2)} = \kappa_{10}^{(4)} = -0.085$).

Influence of gear mesh damping ratio ζ_m is investigated next in Figure.9. The steady-state period-1 solutions are shown for $\zeta_m = 0.05, 0.03$ and 0.01. The value of the gear mesh damping is observed to affect the response amplitudes, level of nonlinear[19] behavior exhibited and the width of parametric instability frequency bands. The system with low damping values demonstrates larger amplitudes, dominant primary & super-harmonic resonances as well as wider frequency ranges of instability.

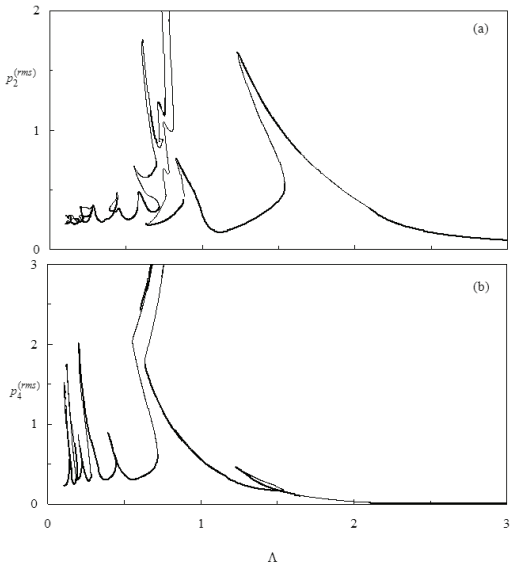

Figure 8: Period-1 HBM solutions for periodic ($K=5$) mesh stiffness amplitudes $\kappa_2^{(2)}=\kappa_2^{(4)}=0.42$, $\kappa_6^{(2)}=\kappa_6^{(4)}=-0.141$, and $\kappa_{10}^{(2)}=\kappa_{10}^{(4)}=-0.085$ for $f_1^{(1)}=11{,}000$ and $k_3=10^8$ N-m/rad; (—) Stable and (——) unstable HBM solutions. (a) $p_2^{(rms)}$ and (b) $p_4^{(rms)}$

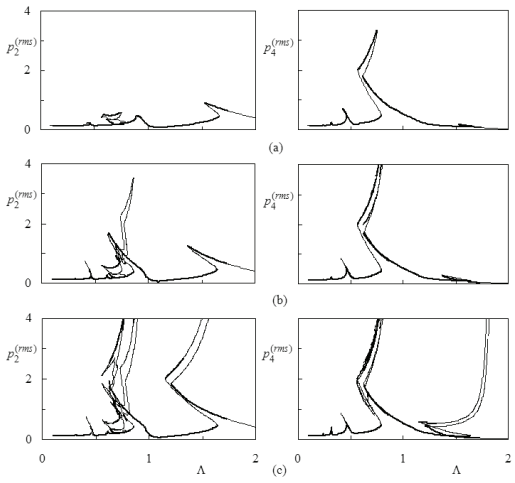

Figure 9: Influence of mesh damping ratio ζ_m on period-1 HBM solutions for $k_3=10^8$ N-m/rad and $f_1^{(1)}=11{,}000$; (—) Stable and (——) unstable HBM solutions. (a) $\zeta_m=0.05$ (b) $\zeta_m=0.03$ and (c) $\zeta_m=0.01$

The dimensionless mesh (tooth pass) frequency was defined in equation 7(a) as $m_i\Lambda$, where m_i is a multiplier introduced to handle the cases when the mesh frequencies of individual gear pairs are not equal. The results shown up to this point considered $m_2=m_4=1$ indicating that the gear mesh frequencies of both gear pairs are identical. This implies gears 2 and 3 that are connected by the shaft of stiffness k_3 have the same number of teeth, but different modules. In general, however, this may not be the case. Two different situations are illustrated in Figures 10 and 11 to demonstrate the changes in steady state response when $m_2\neq m_4$.

In Figure.10, the response is shown for the case when $m_2=1$ and $m_4=2$ where the primary resonances are near the frequencies $\Lambda\approx\omega_{a,n}/m_2=0.96$, $\Lambda\approx\omega_{a,n}/m_4=0.48$, $\Lambda\approx\omega_{b,n}/m_2=1.86$ and $\Lambda\approx\omega_{b,n}/m_4=0.93$. As two of the primary resonance frequencies coincide, $\omega_{a,n}/m_2\approx\omega_{b,n}/m_4$, the period-1 response curves near this frequency include several jump discontinuities. In addition, back collisions are evident at the first two resonance frequencies. As the second example, consider a system having $m_2=3$ and $m_4=2$ whose response is shown in Figure 11. In this case, the primary resonance frequencies are at $\Lambda\approx\omega_{a,n}/m_2=0.32$, $\Lambda\approx\omega_{a,n}/m_4=0.48$, $\Lambda\approx\omega_{b,n}/m_2=0.65$ and $\Lambda\approx\omega_{b,n}/m_4=0.98$. Since these four resonance peaks are spaced closely within narrow frequency range, the response curves become rather complex with several bifurcations and stable and unstable regions.

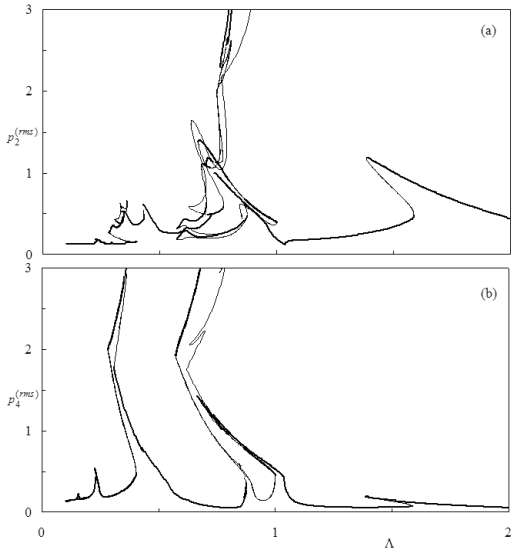

Figure 10: Period-1 HBM solutions due harmonic ($K=1$) mesh stiffness amplitudes $\kappa_2^{(2)}=\kappa_2^{(4)}=0.3$ for $m_2=1$, $m_4=2$, $f_1^{(1)}=11{,}000$ and $k_3=10^8$ N-m/rad; (—) stable and (——) unstable HBM solutions. (a) $p_2^{(rms)}$ and (b) $p_4^{(rms)}$

4.4. Sub-harmonic Resonances and Period-n Motions

Several of the forced response curves shown earlier included regions of unstable period-1 motions at the parametric resonance frequency, $\Lambda\approx 2\omega_{a,n}=1.92$. Although it was not shown in these figures, the same is true for $\Lambda\approx 2\omega_{b,n}=3.92$ as well. In reference [20], period-1 motions were shown to lose their stability at the boundaries of these regions of instability to yield stable period-2 motions. In Figure.12, stable and unstable period-2 motions are shown near $\Lambda\approx 2\omega_{a,n}$ and $\Lambda\approx 2\omega_{b,n}$. These motions are obtained by setting $\eta=2$ in equation (7d,e) and (9).

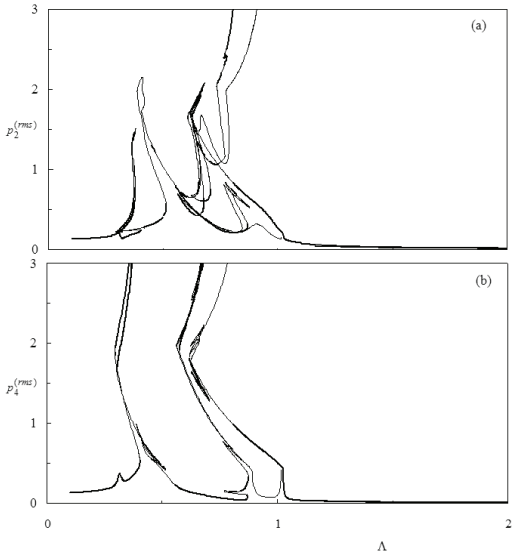

Figure 11: Period-1 HBM solutions due to harmonic ($K=1$) mesh stiffness amplitudes $\kappa_2^{(2)}=\kappa_2^{(4)}=0.3$ for $m_2=3$, $m_4=2$, $f_1^{(1)}=11{,}000$ and $k_3=10^8$ N-m/rad; (—) stable and (——) unstable HBM solutions. (a) $p_2^{(rms)}$ and (b) $p_4^{(rms)}$

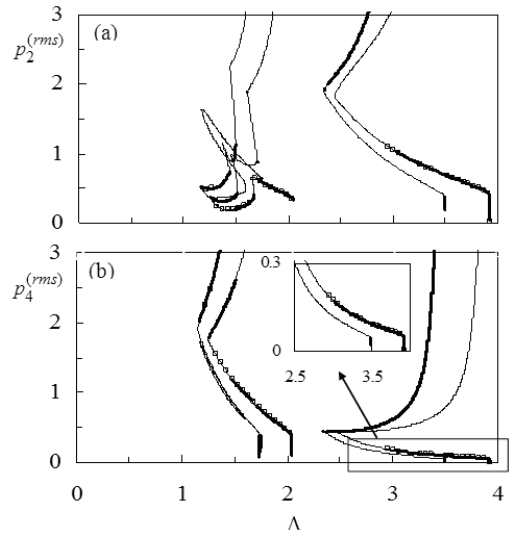

Figure 12: NI and Period-2 sub-harmonic HBM solutions due to harmonic ($K=1$) mesh stiffness amplitudes $\kappa_2^{(2)}=\kappa_2^{(4)}=0.3$ for $f_1^{(1)}=11{,}000$ and $k_3=10^8$ N-m/rad; (—) stable and (——) unstable HBM solutions, (∑) NI solution. (a) $p_2^{(rms)}$ and (b) $p_4^{(rms)}$

The amplitudes of the motions are very large such that back collisions are also obtained in the form of period-2 motions. As these stable period-2 motions cover the entire ranges of unstable perod-1 motions, any catastrophic increases of amplitudes in these ranges are prevented solely due to the gear backlash nonlinearity. Similarly, in Figure.13, period-3 sub-harmonic motions are found to exist near the parametric resonance frequency $\Lambda \approx 3\omega_{a,n}$ by setting $\eta=3$. These motions coexist with stable period-1 motions. However, they form isolated islands which are not connected to the period-1 motions, suggesting that the system may not exhibit such motions unless disturbed drastically.

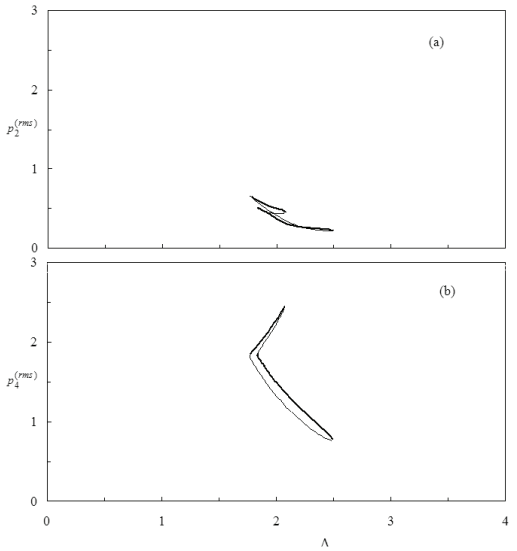

Figure 13: Period-3 sub-harmonic HBM solutions due to harmonic ($K=1$) mesh stiffness amplitudes $\kappa_2^{(2)}=\kappa_2^{(4)}=0.3$ for $f_1^{(1)}=11{,}000$ and $k_3=10^8$ N-m/rad; (—) stable and (——) unstable HBM solutions. (a) $p_2^{(rms)}$ and (b) $p_4^{(rms)}$

5. Conclusions

A non-linear time-varying torsional dynamic model of multi-mesh gear train formed by *M* shafts coupled to each other by $M-1$ gear pairs. The dynamic model included the gear backlash nonlinearity allowing tooth separations and back collisions, the gear mesh stiffness fluctuations, and torsional flexibilities of the shafts. A multi-term Harmonic Balance formulation in conjunction with discrete Fourier Transforms and a Parametric Continuation technique were proposed to obtain the period-n, steady-state motions. The accuracy of solution method was demonstrated through a comparison to the direct numerical integration results.

A three-shaft, two gear-pair example gear train was used to study the influence of the key system parameters. The torsional stiffness of the shaft connecting the gear pairs was shown to influence not only modal characteristics of the system, but also the nonlinear response. It was also shown that the gear mesh stiffness amplitude, gear mesh damping ratio, the torque transmitted and the ratio of the gear mesh frequencies all influenced the forced response significantly. In addition to primary and super-harmonic resonances of period-1 motions, the sub-harmonic resonances of period-2 and period-3 motions were also shown to exist foe the example system considered.

Acknowledgements

The authors thank Hashemite University, Jordon, for supporting the authors during this study.

References

[1] H. Vinayak, R. Singh, and C. Padmanabhan, Linear dynamic analysis of multi-mesh transmissions containing external rigid gears, Journal of Sound and Vibration, Vol.185 ,1995, 1-32.

[2] S. H. Choi, J. Glienicke, D. C. Han, and K. Urlichs, Dynamic gear load due to coupled lateral, torsional and axial vibrations in a helical geared system, Journal of Vibration and Acoustics, Vol. 121, 1999, 141-148.

[3] T. C. Lim, and J. Li, Dynamic analysis of multi-mesh counter-shaft transmission, Journal of Sound and Vibrations, Vol.219, 1999, 905-918.

[4] A. Kahraman, Dynamic analysis of a multi-mesh helical gear train, Journal of Mechanical Design, Vol.116,1994, 706-712.

[5] H. Iida, A. Tamura, K. Kikuchi, and H. Agata, Coupled torsional-flexural vibration of a shaft in a geared system of rotors (1st report), Bulletin of the JSME, Vol.23, 1980, 2111-2117.

[6] H. Iida, A. Tamura, and M. Oonishi, Coupled torsional-flexural vibration of a shaft in a geared system (3rd report), Bulletin of the JSME, Vol.28,1985, 2694-2698.

[7] H. Iida, A. Tamura, and H. Yamamoto, Dynamic characteristics of a gear train system with softly supported shafts, Bulletin of the JSME, Vol.29 ,1986),1811-1816.

[8] T. Iwatsubo, S. Arii, and R. Kawai, Coupled lateral-torsional vibration of rotor system trained by gears, Bulletin of the JSME, Vol.27,1984, 271-277.

[9] K. Umezawa, T. Ajima, and H. Houjoh, Vibration of three axis gear system. Bulletin of JSME, Vol.29,1986, 950-957.

[10] M. Kubur, A. Kahraman, D. Zini, and K. Kienzle, Dynamic analysis of multi-mesh helical gear sets by finite elements, in press, Journal of Vibration and Acoustics, 2004.

[11] M. Benton, M. and A. Seireg, Simulation of responses and instability conditions in a pinion-gear system, Journal of Mechanical Design, Vol.100,1978, 26-32.

[12] M. Benton and A. Seireg, Factors influencing instability and resonances in geared systems, Journal of Mechanical Design, Vol.103,1981, 372-378.

[13] W. Mollers, Parametererregte Schwingungen in einstufigen Zylinderradgetrieben, Ph.D. Dissertation, Rheinisch-Westfalischen Technischen Hochschule Aachen, 1982.

[14] T. Nakada and M. Utagawa, The dynamic loads on gears caused by the varying elasticity of the mating teeth, Proc. of the 6th Japan National Congress for Applied Mechanics,1956, 493-497.

[15] A. Kahraman and G. W. Blankenship, Experiments on nonlinear dynamic behavior of an oscillator with clearance and periodically time-varying parameters, Journal of Applied Mechanics, Vol.64,1997, 217-226.

[16] G. W. Blankenship and A. Kahraman, Steady state forced response of a mechanical oscillator with combined parametric excitation and clearance type non-linearity, Journal of Sound and Vibration, Vol.185, 1994, 734-765.

[17] A. Kahraman, and G. W. Blankenship, Interactions between commensurate parametric and forcing excitations in a system with clearance, Journal of Sound and Vibration, Vol.194, 1996, 317-335.

[18] A. Kahraman and G. W. Blankenship, Effect of involute contact ratio on spur gear dynamics, Journal of Mechanical Design, Vol.121,1999, 112-118.

[19] A. Al-shyyab, and A. Kahraman, Non Non-Linear Dynamic Analysis of a Multi-Mesh Gear Train using Multi-term Harmonic Balance Method: Period-one Motions, in press, Journal of Sound and Vibration,2004.

[20] A. Al-shyyab, and A. Kahraman, Non-linear dynamic analysis of a multi-mesh gear train using multi-term harmonic balance method: sub-harmonic motions, in press, Journal of Sound and Vibration,2004.

JJMIE

Volume 1, Number 1, Sep. 2007
ISSN 1995-6665
Pages 43 - 55

Jordan Journal of Mechanical and Industrial Engineering

A Neural Network Based Real Time Controller for Turning Process

Bahaa Ibraheem Kazem [a,*], Nihad F. H. Zangana [b]

[a] Mechatronics Engineering Dept., [b] Mechanical Engineering Dept., University of Baghdad, Baghdad-Iraq

Abstract

In this paper, the design and implementation of an effective neural network model for turning process identification as well as a neural network controller to track a desired vibration level of the turning machine is as an example of using the neural network for manufacturing process control. Multi – Layer Perceptron (MLP) neural network architecture with Levenberg Marquardt (LM) algorithm has been utilized to train the turning process identifier. Two different strategies have been used for training turning process identifier, and for training the controller model, where there is no mathematical model till now could relate the vibration level to the input turning process parameters "feed, speed, and depth of cut". The vibration signal obtained by the experimental work has been used to train a neural network for identification and control of the turning process. The developed Neuro – controller has been checked by applying different reference vibration signals where it is found that the controller has good ability to track the reference within maximum settling time that does not exceed (4 sec for 95% of the signal); maximum overshot not exceed (30%) of the reference signal used for checking.

Keywords: Real Time Control; Neural Network; Turining.

1. Introduction

The present goal of manufacturing researches focuses on developing flexible, self –adjusting and unattended intelligent machine systems. The limited presence of operators at manned machine tools leaves the supervision, monitoring and control tasks to computer controllers. Although an unattended machining process needs almost no attendance of an operator, tasks such as sensing the effect of process variables and adjusting the conditions accordingly have to be done by appropriate sensors and associated monitors. One solution is to provide on-line adjustment of operating parameters based on sensor information. Systems which posses such capabilities are referred to as adaptive control AC systems. Actually most machining adaptive controllers are categorized in so-called adaptive control for constraints ACC systems, where the operating parameters are adjusted so as to maximize productivity while respecting process constraints like cutting force or power limits. In practice, the most important draw back of ACC is their lack of feed back on part quality where there is no measurement device that could measure part quality "surface finish" in an on line real time manner. In contrast adaptive control with optimization ACO systems adjust the operating parameters so that predefined parameters of performance index are optimized [1]. Most ACO systems assumed a detailed process model is available and complete with known analytical or empirical constant. A great draw back rise here which is the need to collect very specialized experimental and analytical data generally required for model simulation before its implementation in the feed back control scheme. To alleviate some of these problems and provide the model and the controller with more intelligence, better fit to nonlinear behaviour and capacity of adaptation over time, neural networks appear as one of the most interesting techniques.

In recent years, there was an increase interest shown in the utilization of neural networks for various research fields such as robotics, optimization, linear and non-linear programming, pattern recognition, and computer vision. This was due to the advances in neural network algorithms and also the availability of fast parallel architectures that are used to control dynamical systems such as machining systems. The aim is of using multilayered neural network composed of feed back and feed forward controllers, and several learning architectures to train the neural controller in order to provide appropriate inputs to the plant, so the desired response is obtained. In comparison with traditional adaptive controller, their results indicate that neural network approaches well in noise elimination, work for linear and non-linear systems and can be implemented

* Corresponding author. e-mail: drbahaa@uob.edu.iq

very efficiently for large-scale systems [2]. The neural network also used in wide variety of data processing applications, where real-time data analysis and information extraction is required. A great advantage of neural network approach is that most of intense computation takes place during the training process. Once the neural network is trained for particular task, operation is relatively fast and unknown samples can be rapidly identified in the field [3]. Other applications such as modeling, industrial inspection and quality control have been spread in manufacturing field [2].

Presentation and analysis for computerized numerical control CNC for manufacturing system have been introduced by Koren [4]. Two types of CNC systems referred to as Reference-Pulse and Sampled-Data are discussed. In the first system, reference pulses were generated by the computer and supplied to an external digital control loop. With the Sampled – Data technique, the computer served as a comparator of the control loop and transmitted the position error at fixed time intervals. Fig.1. represent block diagram of a Sampled-Data CNC system. Both types had been analyzed analytically and verified experimentally and the results were satisfied.

Athani and Vinod [5] proposed several changes on special type of lathe machine used for watch making. Two stepper motors used to drive the carriage and the cross slide, and low cost PC type (Sinclair ZX spectrum) used as a control platform.

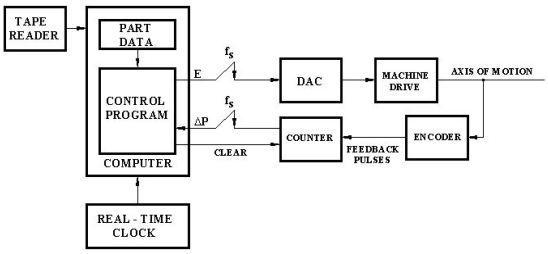

Figure 1: Block diagram of a sampled-data CNC system [4]

Achi [6] have described the utilization of microcomputer to control stepping motor –actuated hydraulic servos deriving a two axis milling machine; also a program for interpolation purpose developed and saved in an assembly language form in the memory.

Altintas and Peng [7] have made a suggestion and implementation of a program for electronically controlling of the speed and position associated to feed operation in a research milling machine. The system main consistence were DC-servomotor (actuator), encoder (for position feed back signal), and tachogenerator (for velocity feed back signal). An IBM PC and interface card controller type (DMC-230 motion controller) used. The response analysis for system analytically and experimentally were found close as follows, a (60) Hz was the frequency operation band for velocity loop, (20) ms was the settling time, and a steady state error of (0.0137fc) "fc feed velocity command". Fig.2. represent the architecture of the suggested control system.

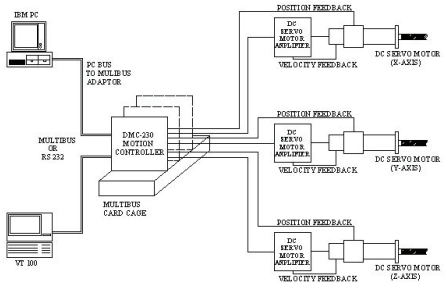

Figure 2: Architecture of speed and position control system for milling process [7]

George et al. [8] evolved a synchronizing control algorithm. This algorithm was developed to minimize the tracking error and the contouring error with stronger emphasis on contouring error. An Intel (486) based AT compatible computer had been used (applying this algorithm) to control a (Matsuura MC510V) high speed, (3-axis) vertical machining centre. A schematic diagram of the control system is shown in Fig.3.

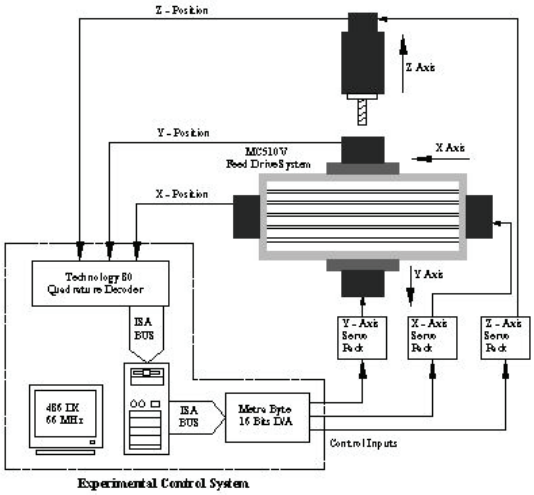

Figure 3: Schematic diagram of the control system for 3-axis vertical machining centre [8]

Jeffery et al. [9] proposed a cutting force-monitoring approach. The approach did not utilize force dynamometers but rather estimates the cutting forces based on the spindle motor current and speed as well as a model that relates these measurements to the cutting force. This method was demonstrated on a CNC lathe machine; the empirical tests showed that the static accuracy was less than (5%) for the proposed system. For large cutting forces the accuracy was. reasonable (20dB S/N ratio), while with lower cutting forces the accuracy decreased.

Khanchustambham and Zhang [10] developed an intelligent on-line monitoring system through a neural network approach. Where the monitoring system detects the cutting force produced during the machining, estimates the tool wear status and finish quality from the dynamic variation of detected cutting force signal and makes a decision for taking corrective action when it is needed .The monitor have been built on feed forward back propagation-algorithm. After the training of the network, it had been applied for cutting force and surface finish monitoring during the turning of advanced ceramic materials. Fig.4. represents a monitoring system.

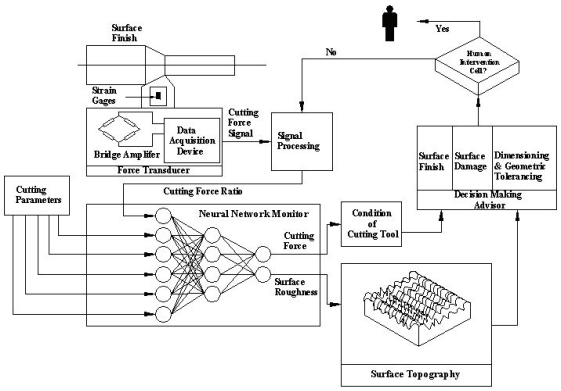

Figure 4: Nural net work Monitoring system for turning process[10]

Larsen [11] have showed that due to significant effects of friction and backlash with turning at low feed rate in nanometric positioning accuracy of machine tool axis especially with significant turning operation such as diamond turning of glass, ceramic, germanium and zinc sulfide for optical usage. A learning motion control algorithm based on the cereblller model articulation controller neural network developed for servo control; the learning controller was implemented using 'C' language on a digital signal processing based apon architecture controller or the single point diamond turning machine.

Azouzi and Guillot [12] evolved an inverse process neurocontroller implemented in multilayer feed forward neural network. On-line adjustments of feed rate and cutting speed ware carried out based on a cost/quality performance index "where the chosen performance index was reaching best quality of product within minimal cost" which were estimated from force and vibration sensor measurements. The simulation and experimental investigations demonstrated the effectiveness of neural network for controlling and optimizing of manufacturing operations. Applied to a single point turning of a typical finishing cutting process, the final dimensions and surface finishes were found to be better by (40) and (80) percent respectively, while productivity was increased by (40) percent over the conditions proposed in machining data handbooks. Fig.5. demonstrates the overall experimental installation.

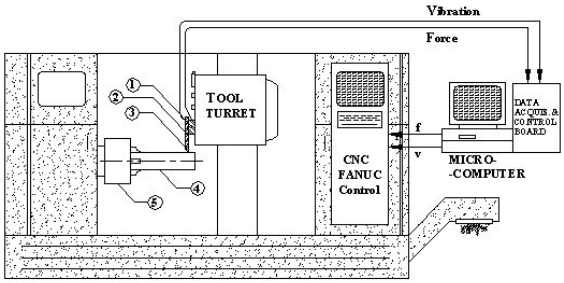

No.	Description	No.	Description
1	Dynamometer	4	Workpiece
2	Accelerometer	5	Spindle
3	Cutting Tool		

Figure 5: Overall experimental installation for on-line adjustments of feed rate and cutting speed [12]

Özel and Nadgir [13] developed two neural network models, one was the back-propagation training neural network and the other was the back-propagation prediction neural network. A trained set of back-propagation neural network algorithms used to predict flank wear of cutting tool with chamfered and honed edge preparation during the orthogonal cutting of hardened steel work pieces. The experiment showed that the neural network could estimate the flank wear progress very fast and accurately once the forces are known. The percentage error was found to be (0.59% - 15.09%) between the measured and the predicted values of flank wear.

Jing et al. [14] proposed a novel XY positioning table synchronously driven by one- side dual linear motors. The redundant drive system commonly suffers from synchronous drive precision problem at high speed and acceleration rates. In this paper, the dynamic model of dual linear motors redundant drive system along X-axis direction is given, and synchronous drive precision can be assured by using a synchronous control scheme. This scheme has two model reference adaptive controllers and a synchronous error compensator based on neural networks. Simulation results are provided to manifest the control system has better static and dynamic performance and higher synchronous drive precision at a morn than 10g ($g = 0.81$ m/ s^2) high acceleration profile motion.

In this work, an approach for using the neural network for identification and control of the vibration signal "acceleration" was utilized.

2. Vibration in Manufacturing Process

Vibration and chatter of a cutting tool are complex phenomena, which, if uncontrolled can lead to premature tool failure, bad surface finish, etc. This is particularly important with brittle tool materials such as ceramics, some carbides and diamond. In addition, vibration affects the mechanical surface and its integrity. If excessive, vibrations may even damage machine tools. Furthermore, the noise generated may be objectionable, particularly if it is at a high frequency. Basically, there are two types of vibration in machining [1].

1. Forced vibration: this type of vibration generally caused by some periodic force present in the machine such as that comes from gear drive, imbalance of the machine tool components, etc. in machining process such as milling or turning a shaft with a key way or splined shaft, forced vibrations are also caused by the periodic entry and exit of the cutting tool. The essential efforts here is to minimize the vibration amplitude, since it cause bad surface finishing of the work piece, and changing its frequency far away from the natural frequency of the system to prevent the probability of resonance occurrence. Although changing the cutting process parameters generally doesn't appear to have much influence of forced vibration, changing the cutting speed may sometimes help [15]. Changing the cutting forces especially the thrust force also can help [1].
2. Self – excited vibration: these vibrations, called "chatter", happen due to the interaction of the dynamics of the chip removal process and the structural dynamics of the machine tool. The excited vibrations are usually very high in amplitude and may cause damage to the

machine tool. Chatter typically begins with a disturbance in the cutting zone, such as lack of homogeneity in the work piece material or its surface condition and geometry or a change in a frictional condition at the tool-chip interface. The most important type of the self – excited vibration called "regenerative chatter", this results from the tool cutting a surface that has roughness or disturbances left from a previous cut. Because of the resulting fluctuations in the cutting forces the tool is subjected to vibration and the process repeated continuously, hence the term regenerative. Changing the operating parameters, which generally include feed rate, cutting speed and depth of cut, could control the chatter .

The need of making measurement of vibration has arisen mainly because of the growth of environmental testing. Specification, many a time requires that the equipment should withstand stated levels of vibrations. This could be done quantitatively only through vibration measurements. Vibration measurements are frequently carried out on rotating and reciprocating machinery for analysis, design and trouble shooting purposes. Much knowledge has been gained in the recent years and computer solutions of various vibration problems have been developed [16]. However, many a time it becomes essential to make actual measurements of vibration characteristics by test during development, either on the machine itself or on its prototype because of the fact that it is difficult to build a perfect mathematical model with all its interrelationship and complexity. The most familiar instrument used for vibration measurements is the accelerometer. This instrument is commercially available in a wide verity of types and ranges to meet corresponding diverse application requirements.

The basis for this popularity lies in the following features [17]:

1. Frequency response is from zero to some high limiting value. Steady accelerations can be measured (except in piezoelectric type).
2. Displacement and velocity can be easily obtained by electrical integration, which is much preferred to differentiation.
3. Measurement of transient (shock) motion is more readily achieved than with displacement or velocity pickups.
4. Destructive forces in machinery are related more closely to acceleration than velocity or displacement.

Piezoelectric accelerometer is widely used for shock and vibration measurements. In general, it doesn't give output for constant acceleration because of the basic characteristics of piezoelectric motion transducer, but it do have large output voltage signal, small size, and can have very high natural frequency. No damping is provided, with material hysteresis being the only source of energy loss. This result in a very low (about 0.01) damping ratio, but this is acceptable because of the very high natural frequency. The design details of piezoelectric accelerometers can emphasize selected features of performance desired for particular application; no single configuration is ideal for all situations since tradeoffs exit here just as in all engineering design. Several designs have been developed for piezoelectric accelerometer and one of the most interested design scheme is the delta shear, shear design use bolted stacks of flat plate element has been introduced recently to gain further improvement in performance [17].

3. Analysis Of Vibration Signal

One of several quantities that could be used to describe the vibration effects is peak value either it is displacement, velocity, or acceleration form of vibration, on the other hand, more complex vibrations are being studied other descriptive quantities may be preferred. One of the reasons for this is that the peak value describes the vibration in terms of a quantity, which depends only upon an instantaneous vibration magnitude regardless of the time history producing it. A further descriptive quantity that does take the time history into account is the Root Mean Square (RMS) value and could be formulated as

$$X_{RMS} = \sqrt{\frac{1}{T}\int_0^T X^2(t)dt} \qquad (1)$$

X_{RMS}: The RMS value of the vibration signal.

T: Period of vibration signal. ; t: Time (sec).

The importance of RMS value comes from its simple relationship to the power content of the vibration, even with more complex form of vibration signal such as random one; it will be suitably meaningful take the RMS value of the signal [18]. Fig.6. represents a random vibration signal.

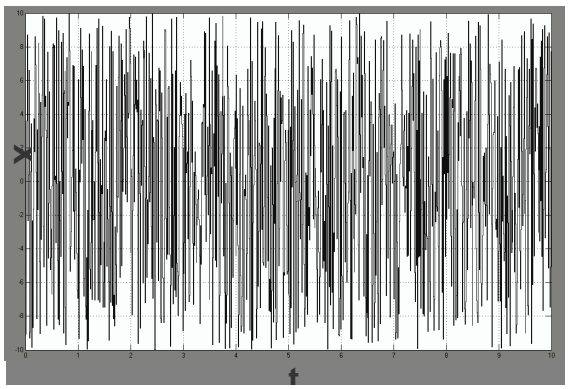

Figure 6: Random vibration signal

Some tests have been done to ensure the randomness of the vibration signal by comparing some of its statistical information with those of a periodic sin wave signal. The tests results are shown in table(1) & Fig.(7).

Table 1: sine wave and random vibration signal statistics data

Statistical data	Sine wave signal	Random signal
Mean	0.034526	0.3287
STD	7.0698	5.8071
RMS	7.0348	5.7876

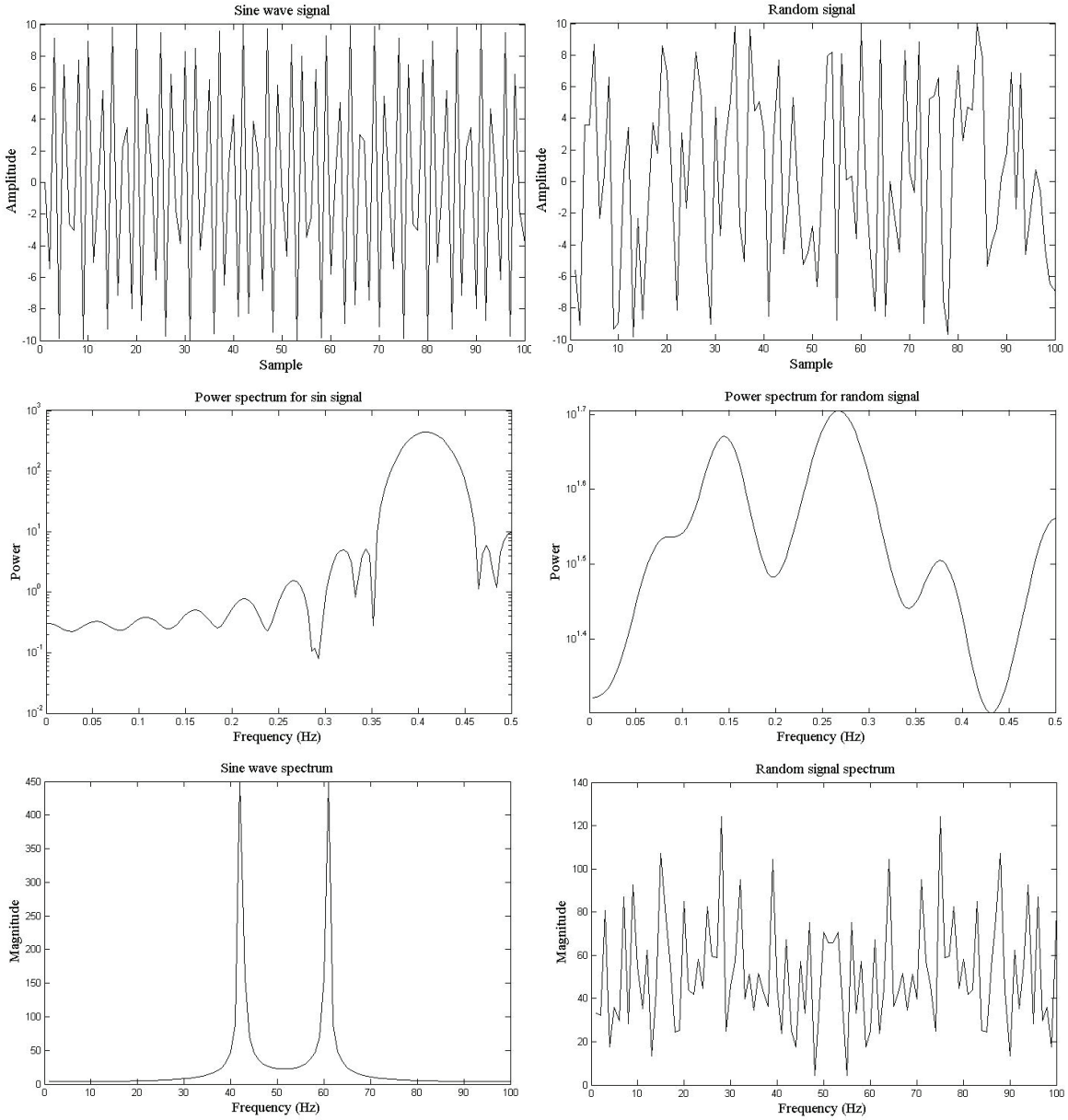

Figure 7: Sine wave and random vibration signal tests results

3.1. Vibration Signal Acquisition

It was found that the selected accelerometer type (4370) was suitable for our application since it has acceleration measurement range of (0.0002 –20000) m/s^2 and a voltage sensitivity of (8.5) mV/ms^{-2}.

3.2. Signal Amplification

Since the vibration signal produced by the accelerometer is too small to be read directly by the A/D converter and by the PC parallel port, the signal should be enlarged using a special type of amplifiers called "instrumentation amplifier". Those amplifiers have special properties such as its high input impedance, low noise, and moderate bandwidth [17]. Those properties have been satisfied using a conditioning amplifier type (2626) [19].

3.3. Calibration Process

Since the measurement system is often made up of a chain of components, each of which is subject to individual inaccuracy, it will be important to know how these inaccuracies may affect the over all system measurement precision. The most common method to do this is to find the least square criterion, which minimizes the sum of the squares of the vertical deviations of the data points from the fitted line. The algorithm explained briefly in the appendix C for single component. But for chain of components, the collected information of each individual component calibration should be taken into consideration according to a specified procedure [17].

Assume a case where a computing quantity K.

$$K = f(u_1, u_2, u_3, ..., u_n) \quad (2)$$

K :Known function of the n independent variables $u_1, u_2, u_3, ..., u_n$. The $u's$ are the measured quantities (instrument or component outputs) and are in error by $\pm\Delta u_1, \pm\Delta u_2, \pm\Delta u_3, ..., \pm\Delta u_n$, respectively. These errors will cause an error ΔK in the computed result K. The $\Delta u's$ may be considered as absolute error.

$$K \pm \Delta K = f(u_1 \pm \Delta u_1, u_2 \pm \Delta u_2, u_3 \pm \Delta u_3, ..., u_n \pm \Delta u_n) \quad (3)$$

By subtracting K in equation (2) from $K \pm \Delta K$ in equation (3), we finally obtain $\pm\Delta K$ which is needlessly time consuming procedure; however an approximate solution valid for engineering purposes may be obtained by application of the Taylor series. Expanding the function f in a Taylor series, we get

$$f(u_1 \pm \Delta u_1, u_2 \pm \Delta u_2, u_3 \pm \Delta u_3, ... u_n \pm \Delta u_n) = f(u_1, u_2, u_3, ... u_n) + \Delta u_1 \frac{\partial f}{\partial u_1} + \Delta u_2 \frac{\partial f}{\partial u_2} + \Delta u_3 \frac{\partial f}{\partial u_3} + ... + \Delta u_n \frac{\partial f}{\partial u_n} + \frac{1}{2}\left[(\Delta u_1)^2 \frac{\partial^2 f}{\partial u_1^2} + ... \right] + ... \quad (4)$$

In actual practice, the $\Delta u's$ will all be small quantities and thus terms such as $(\Delta u)^2$ will be negligible. Then equation (4) may be given approximately as

$$f(u_1 + \Delta u_1, u_2 + \Delta u_2, u_3 + \Delta u_3, ..., u_n + \Delta u_n) = f(u_1, u_2, u_3, ..., u_n) + \Delta u_1 \frac{\partial f}{\partial u_1} + \Delta u_2 \frac{\partial f}{\partial u_2} + ... + \Delta u_n \frac{\partial f}{\partial u_n} \quad (5)$$

So absolute error E_a is given by

$$E_a = \Delta K = \left|\Delta u_1 \frac{\partial f}{\partial u_1}\right|_{u_1} + \left|\Delta u_2 \frac{\partial f}{\partial u_2}\right|_{u_2} + \left|\Delta u_3 \frac{\partial f}{\partial u_3}\right|_{u_3} + ... + \left|\Delta u_n \frac{\partial f}{\partial u_n}\right|_{u_n} \quad (6)$$

When the $\Delta u's$ are considered not as absolute limits of error, but rather as statistical bounds such as $\pm 3S$ limits. The equation (6) modified to the root – sum square (rss) formula.

$$E_{arss} = \sqrt{\left(\Delta u_1 \frac{\partial f}{\partial u_1}\right)^2 + \left(\Delta u_2 \frac{\partial f}{\partial u_2}\right)^2 + \left(\Delta u_3 \frac{\partial f}{\partial u_3}\right)^2 + ... + \left(\Delta u_n \frac{\partial f}{\partial u_n}\right)^2} \quad (7)$$

the measurement system consists of two major parts. The first part (accelerometer and charge amplifier), and the second part (interface card and host PC). Our individual calibration process for parts one and two of the measurement system shows the following results.

First part curve-fitting equation

$y_1 = 0.97x$, $S = 0.00494$

Second part curve-fitting equation

$y_2 = 0.95x - 0.026$, $S = 0.146$

Where S is the standard deviation value STD

Assume $\pm 3S$ limits, E_{arss} could be evaluated as follows.

$$E_{arss} = \sqrt{(3*0.00494*0.97)^2 + (3*0.146*0.95)^2} = 0.46$$

$\cong 0.5$

Percentage inaccuracy =

$$\frac{E_{arss}}{full\ scale} * 100\% = \frac{0.5}{10} * 100\% = 5\%$$

Fig.8, and Fig.9. Show part one and part two calibration curve fitting figures respectively.

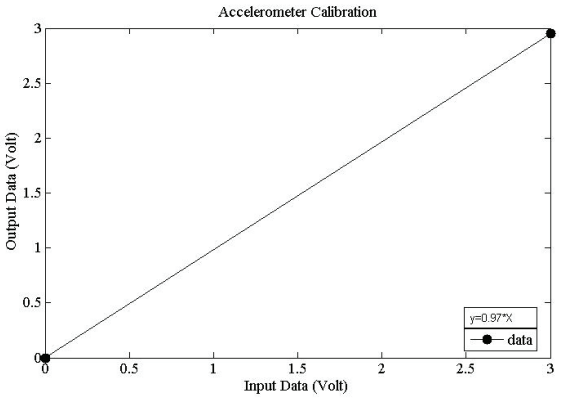

Figure 8: Accelerometer calibration

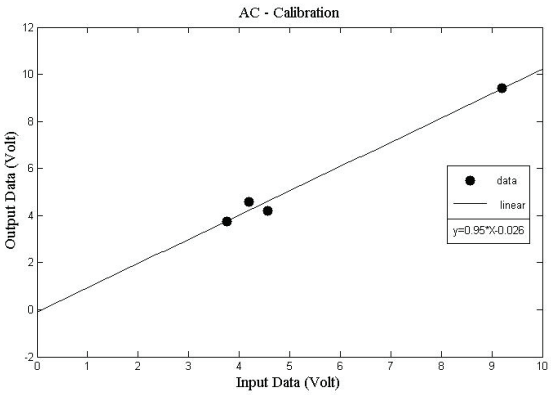

Figure 9: AC – signal calibration

4. Experimental Cutting Test

The experimental tests accomplished using turning machine, and the cutting tool used for the process was HSS with medium carbon steel as a work piece. The tests have been done with a constant depth of cut equal to (0.6mm), with no cooling fluid. Fig.10. demonstrates the experimental work layout. Table .2 . shows the statistical information obtained at each cutting process. Figs 11-14 show some experimental reading for the acceleration at cutting tests.

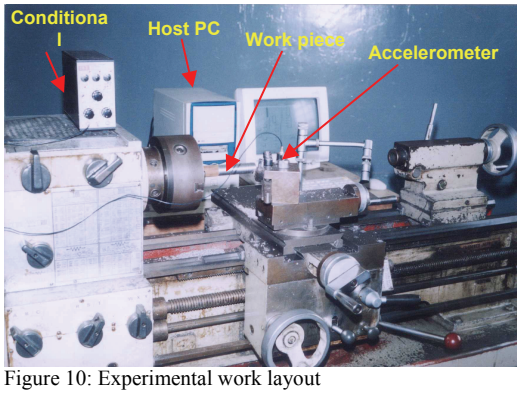

Figure 10: Experimental work layout

Table 2: Statistical information obtained by experimental work

Test	Speed (rpm)	Feed (mm/rev)	RMS	Mean	STD
1	540	0.03	4.9767	-0.0240	4.9794
2	540	0.04	4.8862	0.2680	4.8816
3	540	0.05	4.9206	-0.0444	4.9231
4	540	0.1	5.4808	0.3021	5.4756
5	540	0.06	4.7578	-0.0258	4.7604
6	260	0.06	3.7975	0.0036	3.7997
7	260	0.03	5.1199	0.2867	5.1148
8	260	0.04	5.3227	0.1029	5.3347
9	260	0.05	5.0697	0.3848	5.0579
10	260	0.08	5.3073	0.3794	5.2967
11	370	0.1	5.0680	0.1484	5.0687
12	370	0.08	4.8541	0.3651	4.8431
13	370	0.06	4.1390	0.2286	4.1350
14	370	0.04	4.4053	0.0160	4.4077
15	370	0.03	4.0282	0.3876	4.0117
16	125	0.06	3.7041	0.2813	3.6955
17	125	0.08	3.4407	0.1027	3.4411
18	125	0.1	2.9997	-0.0269	3.0013
19	125	0.04	3.3285	0.1664	3.3262
20	125	0.05	3.1207	-0.0336	3.1223
21	180	0.05	3.8133	0.0602	3.8150
22	180	0.08	3.9633	0.0463	3.9653
23	180	0.06	2.7079	-0.0342	2.7092
24	180	0.1	3.0113	0.0366	3.0128
25	180	0.04	2.6154	-0.1283	2.6137
26	180	0.03	2.9496	-0.1303	2.9484
27	85	0.1	2.3361	-0.0314	2.3372
28	85	0.08	2.1937	-0.0454	2.1945
29	85	0.06	2.2187	0.0987	2.2177
30	85	0.04	2.3136	0.1203	2.3118

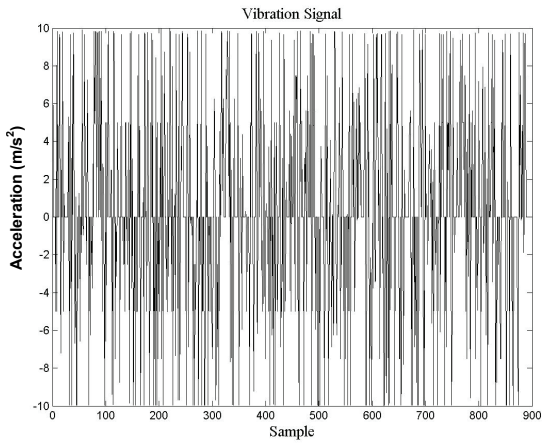

Figure 11: Test (No.4)

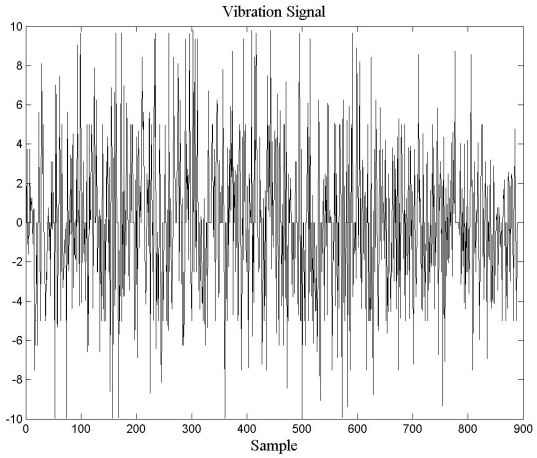

Figure 12: Test (No. 6)

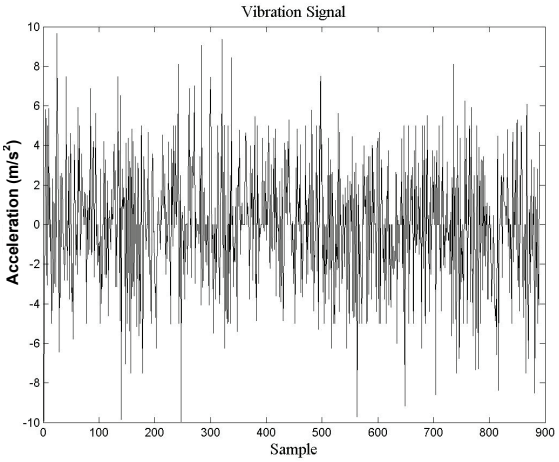

Figure 13: Test (No.20)

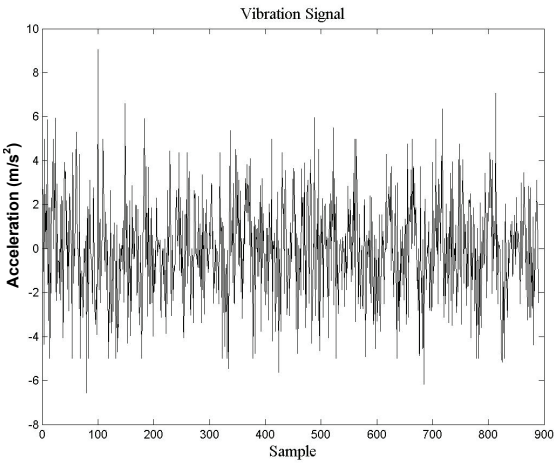

Figure 14: Test (No.27)

5. Network Architecture

Commonly one neuron, even with much input, may not be sufficient. A need for more complicated network architecture arises that serve as multi neurons operating in parallel in what is called "layer". Sometimes multi layers are more powerful than the single layer network. For instance, a two-layer network having a sigmoid transfer function in the first layer and a linear transfer function in the second layer can be trained to approximate most functions arbitrarily well [20]. For more demonstration Fig.15. shows two-layer network.

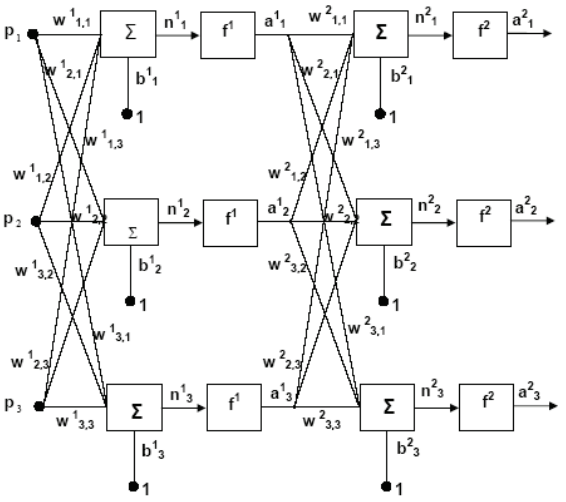

Figure 15: Two layer network arcitecture

It will be more convenient to describe the input/output mathematical relationship in matrix form, where:

$$a^2 = f^2\left(\left[w^2\right] * f^1\left(\left[w^1\right] * \{p\} + \{b^1\}\right) + \{b^2\}\right) \tag{8}$$

or

$$\begin{Bmatrix} a_1^2 \\ a_2^2 \\ a_3^2 \end{Bmatrix} = f^2\left(\begin{bmatrix} w_{1,1}^2 & w_{1,2}^2 & w_{1,3}^2 \\ w_{2,1}^2 & w_{2,2}^2 & w_{2,3}^2 \\ w_{3,1}^2 & w_{3,2}^2 & w_{3,3}^2 \end{bmatrix} * f^1\left(\begin{bmatrix} w_{1,1}^1 & w_{1,2}^1 & w_{1,3}^1 \\ w_{2,1}^1 & w_{2,2}^1 & w_{2,3}^1 \\ w_{3,1}^1 & w_{3,2}^1 & w_{3,3}^1 \end{bmatrix} * \begin{Bmatrix} p_1 \\ p_2 \\ p_3 \end{Bmatrix} + \begin{Bmatrix} b_1^1 \\ b_2^1 \\ b_3^1 \end{Bmatrix}\right) + \begin{Bmatrix} b_1^2 \\ b_2^2 \\ b_3^2 \end{Bmatrix}\right) \tag{9}$$

In spite of existence of several other network architecture, that could be useful for a lot of applications, and it has been used in this research.

6. Neural Network Training

It is important now to know how the weights and biases of a network could be determined. With complex network, having many inputs and complicated architecture, the training algorithms solve this problem. The training algorithms (learning rules) could be defined as "a procedure for modifying the weights and biases of a network in order to train the network to perform some task" [20].

6.1. General Architecture Selection

One of the problems that occur during neural network training is called overfitting. The error on the training set is driven to very small value, but when new data is presented to the network the error becomes large. The network has memorized the training examples, but it has not learned to generalize to new situation.

One method for improving network generalization is to use a network that is just large enough to provide an adequate fit. The larger the network, the more complex the functions the network can create. If we use a small network, it will not have enough power to over fit the data. Unfortunately, it is difficult to know before hand how large a network should be for a specific application .

6.2. Data Pre – Processing

Neural network can be made more efficient if certain preprocessing steps are performed on the network inputs and targets. This subsection describes some common processing techniques that could be used to make training process more effective.

6.3. Process Dependency on Min and Max of Data Values

Before training, it is useful to scale inputs and targets so that they always fall within a specified range. This process makes the data fall in the range [-1, 1]. After the completion of training process the network out put should be converted back into its original units that were used for the original targets.

6.4. Process Dependency on Mean and STD of Data Values

The original network inputs and outputs are given in the matrices p and t respectively. The normalized inputs and targets that are returned will have zero mean and unity standard deviation. Also the network outputs should be converted back to the original units of the targets.

The data pre – processing used for the data depends on normalizing it according to data's maximum and minimum values. This process carried out for both input "feed, speed" vector and output "vibration RMS" vector. Equation 10 shows the normalization equations.

$$p_n = \left(2 * \left(p - \min p\right) \Big/ \left(\max p - \min p\right)\right) - 1 \tag{10}$$

Where p : Input matrix

p_n : Normalized input matrix.

$\min p, \max p$: Minimum and maximum input value in the matrix.

6.5. Data Post – Processing Analysis

The performance of a trained network can be measured on some extent by the errors on the training. But it is often useful to investigate the network response in more detail. One option is to perform a regression analysis between the network response and the corresponding targets. The process will return three parameters. The first two parameters, (m and b), correspond to the slope and the y – intercept of the best linear regression relating targets to the network outputs. The third variable that returned by the post processing is the correlation coefficient (R – value) between the outputs and the targets. It is a measure of how well the variation in the output is explained by the targets. If this number is equal to (1), then there is perfect correlation between the targets and outputs [22].

7. Neuro – Controller

Most of the neuro –control schemes developed until now are based on the following design approaches [20]. Series control scheme: the neural network directly learns the mapping from the desired reference signal to the control inputs, which yields these signals.

Parallel control scheme: a neural network is used to compensate the control signal which is provided by conventional controller such that the plant output can track the desired output as close as possible.

Self – tuning control scheme: a neural network tunes the control parameters including the conventional controller such that the plant output follows the desired output signal as much as possible.

Emulator and controller scheme: it maximizes some measure of utility or performance over time, but can't efficiently account for noise and can't provide real – time learning for slow convergence, also known as backpropagation - through - time.

The self – tuning control scheme has been used in this research and it is explained as follows.

7.1. Self - Tuning Neuro – Control Scheme

The self – tuning neuro – control scheme is illustrated in Fig.16., where a neural network is used to tune the parameters of a conventional controller similar to adjustment made by a human operator. The process need that the human operator has a moderate amount of experience and a great knowledge on the control system, however, unlike the computer, it is rather impossible for the operator to store past data history of the system for any kind of operating condition. If one can include the experience and the knowledge of the operator into a neural network and train it based on the past data history, then the trained neural network could be used as means to tune the controller parameters in an on – line way[23].

8. Design of the Self - Tuning Neuro - Controller

Neural network has been applied very successfully in the identification and control of dynamic systems. The universal approximation capabilities of the multilayer perceptron MLP make it a popular choice for modeling nonlinear systems and for implementing general-purpose nonlinear controller The following describes the process of design of the neural network controller. There are typically two steps that involved when using neural network for control .

1. System identification.
2. Control design.

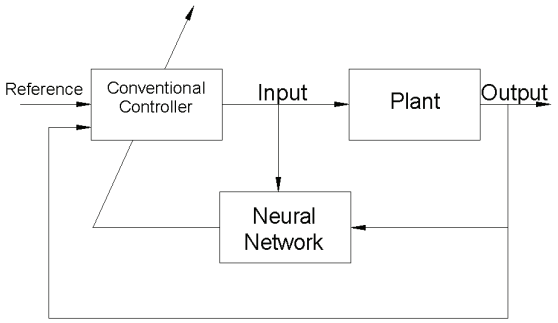

Figure 16: tuning neuro – control scheme

9. Design of the Self - Tuning Neuro - Controller

Neural network has been applied very successfully in the identification and control of dynamic systems. The universal approximation capabilities of the multilayer perceptron MLP make it a popular choice for modeling nonlinear systems and for implementing general-purpose nonlinear controller The following describes the process of design of the neural network controller. There are typically two steps that involved when using neural network for control .

1. System identification.
2. Control design.

As described previously in system identification stage, a model for the system want to be controlled should be developed. In control stage the developed model should be used in training the controller.

This controller uses a neural network model to predict future plant responses to potential control signals. An optimization process then computes the control signal that optimizes the future plant performance. The predictive control process is based on receding horizon technique. The neural network model predicts the plant response over a specified time horizon. The predictions are used by a numerical optimization process to determine the control signal that minimizes the performance criterion "equation (11)" over the specified horizon. Fig..17. demonstrates the controller optimization procedure. This controller has been designed and used for this work.

$$Z = \sum_{j=N_1}^{N_2} \left(y_r(t+j) - y_m(t+j)\right)^2 + \rho \sum_{j=1}^{N_u} \left(u'(t+j-1) - u'(t+j-2)\right)^2 \quad (11)$$

Z : Optimization performance index.

N_1, N_2, N_u : The horizons over which the tracking error and the control increments are evaluated.

u' : The tentative control signal "Tentative Feed and Speed Values".

y_r : The desired response "Desired Vibration RMS Value".

y_m : The network model response "Vibration RMS Value Developed by the Model".

ρ : Factor determines the contribution that the sum of the square of the control increments has on the performance index.

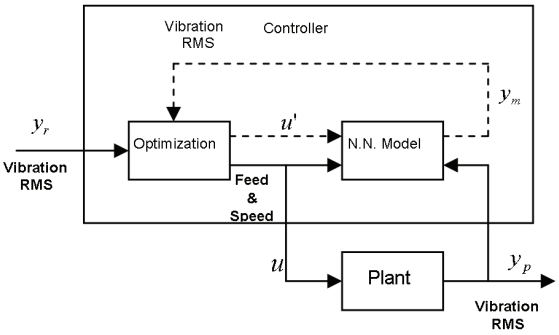

Figure 17: optimization procedure

10. Result and Discussion

The designed controller has been used to control turning process identifier by applying different reference signals to it as test inputs, to find out its ability to follow the desired response; the controller is fed by the reference signals, which were the vibration RMS values, and the responses that have been shown on the scope. The controller here is designed to generate the values of the feed and the speed and then the neural network turning process identifier maps it into vibration RMS values, the controller reads back the output signal and compare it to the signal results from its neural network model where the optimization algorithm update the control action (feed, speed) signals so that the turning process identifier follow the required reference signal. Fig18. Demonstrate the controller model training process. The learning rate (α) set to (0.75), and control process maximum error set to ($1*10^{-3}$), which make the training process reached to the specified goal at (199) epoch. The designed controller model has been trained by the backpropagation algorithm described in chapter four, it consist of two layer perceptron neural network with eight neuron in the hidden layer and one neuron at the output layer.

The controller model designed with "*tansig*" activation function in the hidden layer and "*purelin*" activation function in the output layer. Fig.19. shows the turning process controller. The optimization for process control is simulated by the flowchart shown in Fig.20. Different reference signals have been used for testing the response of the controller .The first was for input reference equal to 5, the second was for input reference 4.5 for the first two second and then the reference decreased to 3.5. The final case was the response of the controller for input reference signal started with 3.5 and then increased to 4. The sampled time used was (0.01 sec "100 sample = 1 sec").

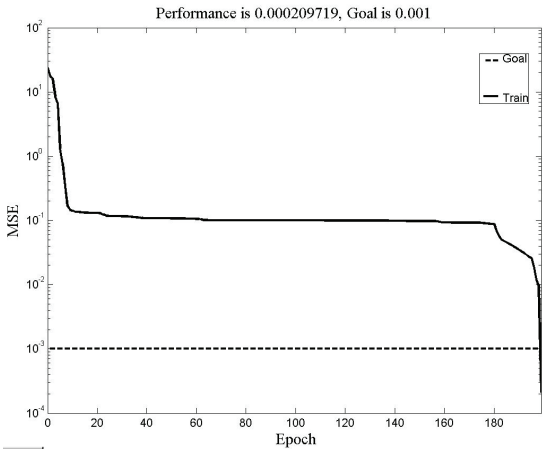

Figure 18: Controller model training process

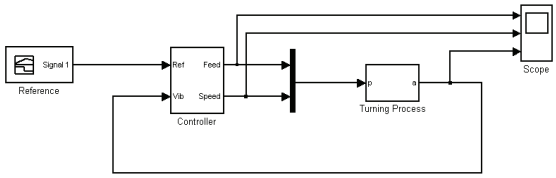

Figure 19:Turning process controller

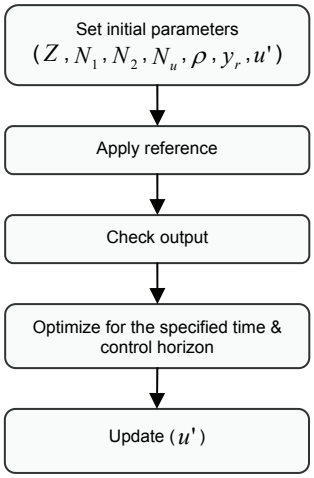

Figure 20: Optimization flowchart

The design of system identifier shows precise results with (10neuron), where the training performance index set to ($1*10^{-8}$) as MSE of the output of the neural network and the trained network met that goal since the error between the neural network output and the targets did not exceeds ($1.55*10^{-4}$). For the designed neural network controller, it is found that the controller track the reference signals set, where setting the reference signal to (5) as acceleration RMS value as shown in fig.22. made the controller after a starting with an initialization values of the feed and the speed be changed. For reference signal equal to (5) the controller adapts new feed and speed values 0.095mm/rev, and 440RPM respectively, this adaptation completes after (100samples = 1sec) "setting time" and the response progresses with a steady state error that doesn't exceeds (8%) of the reference signal due to the fluctuating speed value. Two different reference signals have been set to check the ability of the controller to track these specified

reference signals as shown in Fig.23, where setting of the reference signal to (4.5) as acceleration RMS value made the controller adapt new feed and speed values equal to 0.085 mm/rev and 440 RPM respectively, the controller reaches to the specified reference after (300 samples = 3 sec) "settling time". The new reference signal (3.5) has been tracked by the controller after (400samples = 4sec) as settling time and the adapted feed and speed values were 0.073mm/rev and 270RPM. Finally new two reference signals (3.5,4) have been set as acceleration values as shown in Fig.23., the controller changes it initial values (feed = 0.035 mm/rev, speed = 270 RPM) to 0.068 mm/rev and 330 RPM to reach the reference signal within (200samples = 2sec).

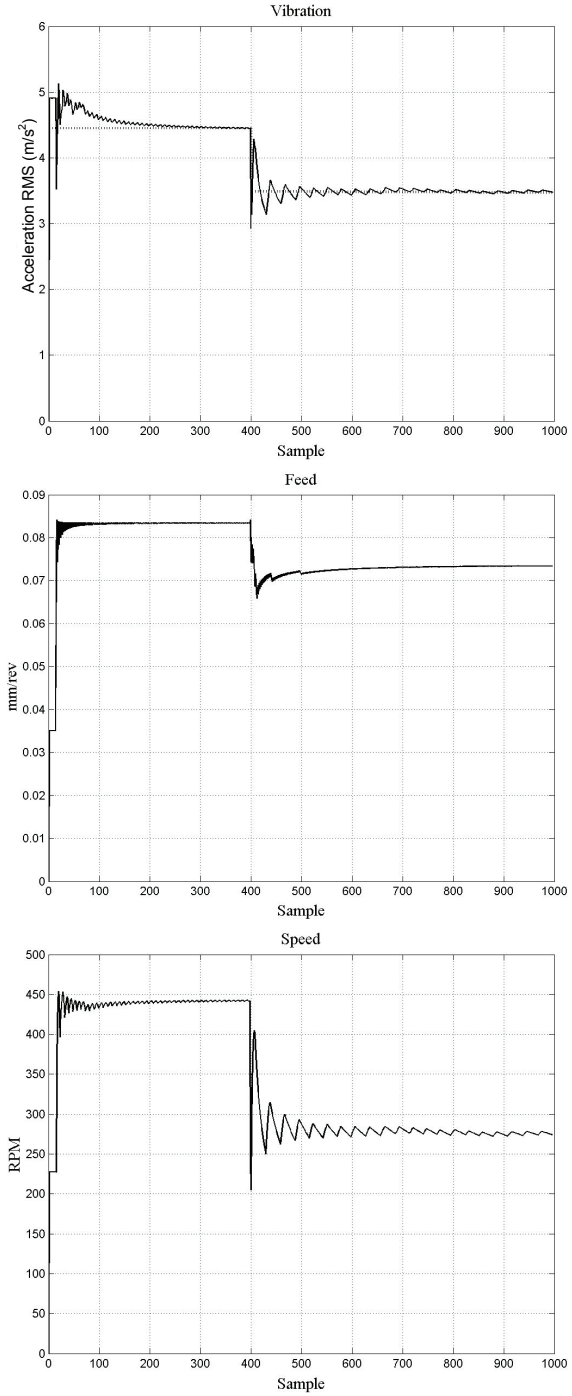

Figure 21: Controller response (input reference = 5)

Those reference signals tracking process that have been achieved by the Neuro - controller show the ability of the controller to track the reference signal with minimum settling time equals to (100samples = 1sec) and maximum settling time equals to (300samples = 3sec) and a maximum overshot for the test signals that doesn't exceeds (30%) of the reference signals. Fig.21, Fig.22, and Fig.23 show that increases the value of reference (acceleration RMS) not necessarily leads to increase the control signal (Feed, Speed) neither decrease it should decrease the control signal.

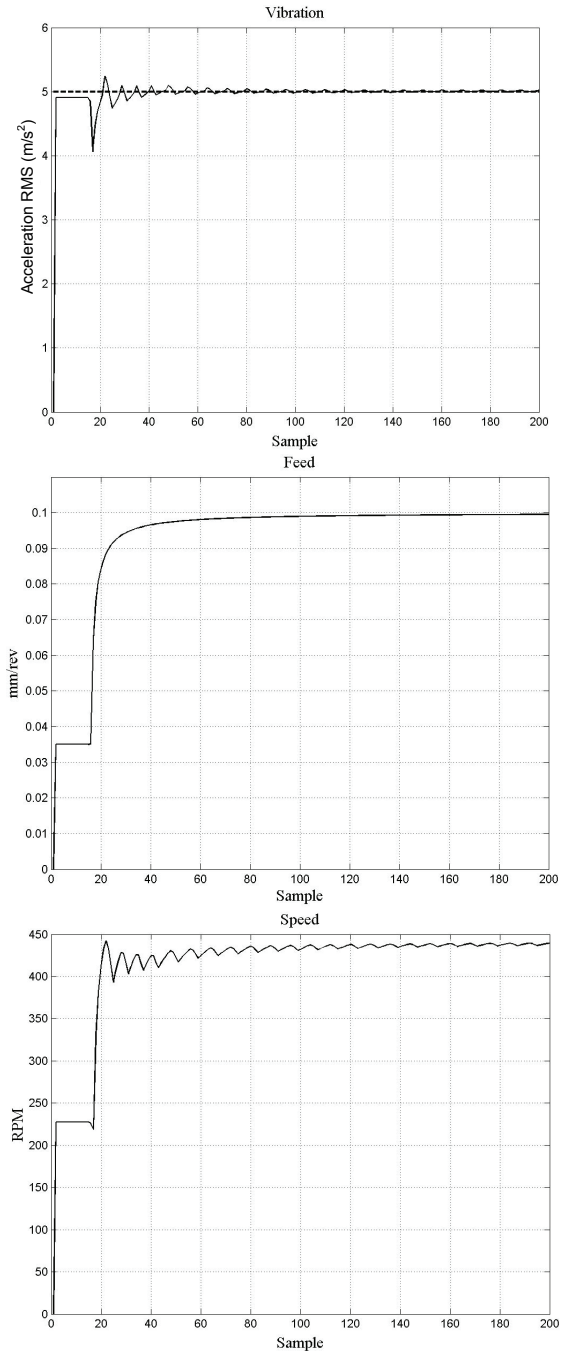

Figure 22: Controller response (input reference = 5)

11. Conclusion

In this work, the effectivness of using neural networks as identification and as an alternative to adaptive controller of metal cutting process are inverstigated. Also, using the neural network for system identification releases the controller designer from the problem of modeling complex real systems and the confusing related to selection of the least significant system variables which can be ignored.

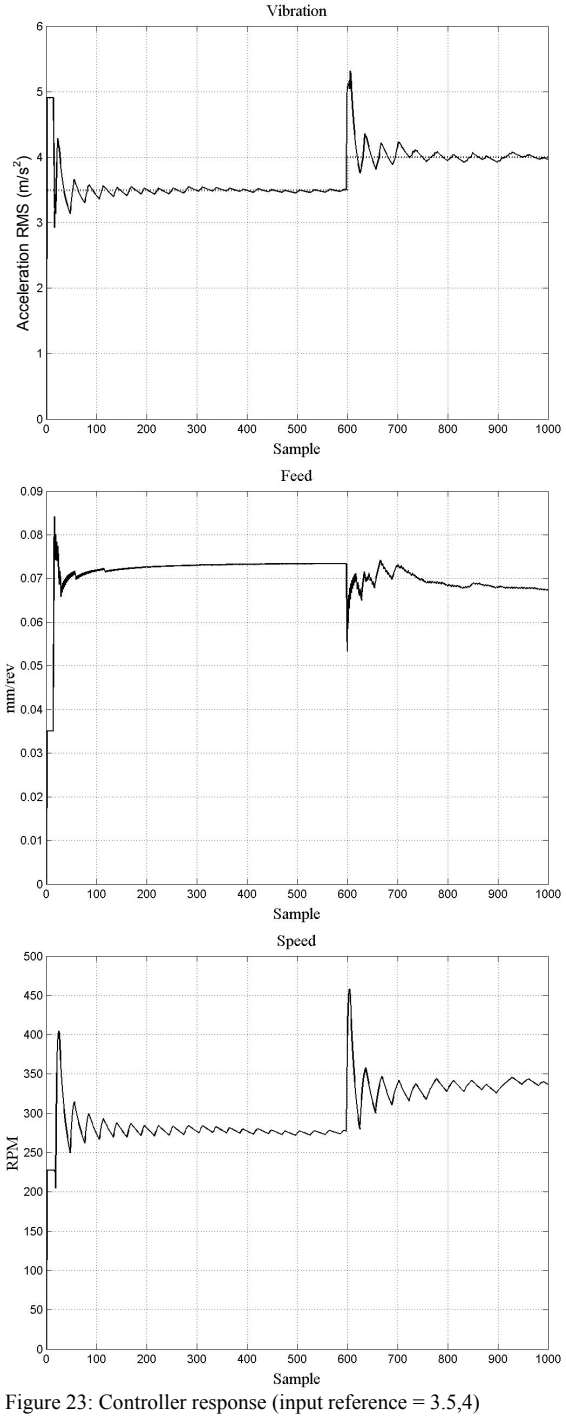

Figure 23: Controller response (input reference = 3.5,4)

The using of LM (Levenberg-Marquardt) training algorithm on the MLP network even with its property of needing to large memory is successful algorithm in minimizing the training error, which makes it good training algorithm for system identification with high degree of accuracy, while the traditional Back propagation algorithm can be used to train neural networks with greater error allowance. The controller proposed in the current work follow the desired response with control actions (Feed, Speed) not mentioned in the training data and this make the neural network has an advantage in being work as intelligent map. Few practical experiments used for training the neural network (identifier, controller) may cover the process with less error and this will minimize the efforts of achieving a lot of practical experiments if compared with the other traditional controllers.

References

[1] M. P. Groover "Fundamental of modern manufacturing process". by Prentice Hall International Inc.1996.

[2] P. Tai, H. A. Ryaciotaki, and D. Hollaway "Neural network implementation to control system". A survey of algorithms and techniques. Transaction of IEEE, Vol.25, No.3,212-217, 1991.

[3] P. E. Keller, R. T. Kouzes, L. J. Kangas, and S. Hashem "Neural network based system for manufacturing application". A paper represented at the advanced information system and technology conference in Williamsburg, VA, USA (28-30) March (1994).

[4] Y. Koren "Design of computer control for manufacturing system". Transactions of the American society of mechanical engineering (ASME), Vol.101, 1979. 326-331.

[5] V.V. Athani and H. N. Vinod"A CNC system for a lathe using a low cost PC". Computers in industry, Vol. 7, PP. 427-434, 1986.

[6] P. U. Achi "A low – cost computer numerical control machine system using LSI interfaces". IEEE transactions on industrial electronics, Vol. 34, No. 1, 1987.

[7] Y. Altintas and J. Peng "Design and analysis of a modular CNC system". Computers in industry, Vol. 13, 1990. 305-316.

[8] T. George, C. Chiu, and M. Tomizuka "Coordinated position control of multi-axis mechanical system". Journal of dynamic systems, measurement, and control, 1998. (389-393).

[9] L. Jeffery, H. Stein, and K. Huh "Monitoring cutting forces in turning: A model based – approach". Vol. 124, 2002. 26-31; ASME.

[10] R. G. Khanchustambham, and G. M. Zhang "A neural network approach to on - line monitoring of a turning process", Transaction of IEEE, Vol. 12, No.5, 1991.107-113.

[11] L.G. Alan "Neural network servo control for ultra-precision machining at extremely low feed rate". PhD Thesis, University of Illinois at Chicago, 1996.

[12] R. Azouzi and M. Guillot "On-line optimization of the turning process using an inverse process neurocontroller". Journal of Manufacturing Science and Engineering, Vol. 120, 1998,101-108.

[13] T. Özel and A. Nadgir "Prediction of a flank wear by using back- propagation neural network modeling when cutting hardened H-13 steel with chamfered and honed CBN tools" International journal of machine tools & manufacturing design research and application, 2001.

[14] Jeng Chen, Qiang Liu and Chang Qi" A Synchronous Drive Control Scheme Based on Neural Networks for a Novel XY-table" Proceedings of the IEEE International Conference on Automation and Logistics August 18 - 21, 2007, Jinan, China

[15] S. Kalpakjian "Manufacturing Engineering and technology" 4'th edition , by Prentice Hall International Inc, 2001.

[16] A. K. Sawhney "A course in mechanical measurements and instrumentation". Second edition 1995, by Dhanpat rai and sons.
[17] E. O. Doebelin "Measurement systems application and design" Fourth edition 1990, by McGraw –Hill publishing company.
[18] J. T. Broch "Mechanical vibration and shock measurements". First edition 1980, K. Larsen & Son A/S for publishing.
[19] Brüel & Kjaer corporation "Piezoelectric accelerometer and vibration preamplifier hand book". K. Larsen & Son A/S for publishing, 1978.
[20] M. T. Hagan, H. B. Demuth, and Mark Beale "Neural network design". First edition 1996, McGraw - Hill publishing company.
[21] S. Omatu, M. Khalid, and R. Yusof "Neuro – control and its applications". Springer publishing company, 1994.
[22] O. Omidvar and D.L. Elliot "Neural system for control"., Springer publishing company, 1997.
[23] D. T. Pham and L. Xing "Neural networks for identification, prediction, and control", Springer publishing company, 1997.

JJMIE

Volume 1, Number 1, Sep. 2007
ISSN 1995-6665
Pages 57 - 67

Jordan Journal of Mechanical and Industrial Engineering

A Graphical Design of an Input-Shaping Controller for Quay-Side Container Cranes with Large Hoisting: Theory and Experiments

Ziyad N. Masoud [a,*], Mohammed F. Daqaq [b]

[a] Department of Mechanical Engineering, The Hashemite University, Zarqa 13115, Jordan
[b] Department of Mechanical Engineering, Clemson University, Clemson, SC 29634, USA

Abstract

Input-shaping is a practical open-loop strategy for the control of transient and residual oscillations on cranes, especially those having predefined payload transfer paths and repeated maneuvers. In this paper double-step input-shaping control approach is developed to include maneuvers that involve large hoisting distances and speeds. The approach is based on using the graphical representation of the phase plane of the payload oscillations. The phase plane is used to derive mathematical constraints to compute the switching times of a double-step acceleration command profile that will result in minimal transient and residual oscillations. The controller design is based on a two-dimensional four-bar-mechanism model of a container crane. For the purpose of controller design, the model is reduced to a constrained double pendulum with variable length hoisting cable and a kinematic angular constraint. The generated commands were based on both a linear and a nonlinear frequency approximations of the payload oscillation period. Numerical and experimental results demonstrated that in contrast with the single-step input shaping controllers, which are very sensitive to frequency approximations, the proposed double-step controller is less sensitive to small variations in the frequency even with large commanded accelerations. Using this approach, oscillations during and at the end of transfer maneuvers can be reduced to less than 5 cm on a full size model of a 65 ton quay-side container crane.

Keywords: Input-shaping; container crane; crane control.

1. Introduction

Motion control of suspended objects has seen mounting research interest since the early 1960's. The dynamics of such systems are used to model the dynamics of the payload oscillations in many important industrial applications, such as gantry cranes, boom cranes, ship-mounted cranes, telescopic cranes, and quay-side container cranes.

A particularly important case is that of a quay-side container crane, Fig. 1. Inertial forces on the payload due to crane commanded trajectories can cause the payload to experience large sway oscillations. To avoid exciting these oscillations, crane operators resolve to slowing down the operations such that the oscillations do not cause safety concerns and possible damage of the payload. However, slowing down operations increases the cost of loading and unloading operations.

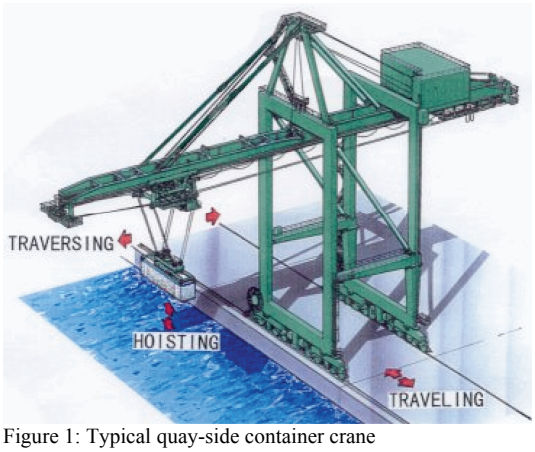

Figure 1: Typical quay-side container crane

In contrast with other types of cranes, which are usually modeled as a simple pendulum with a rigid or flexible hoisting cable and a lumped mass at its end [1–7], quay-side container cranes have a significantly different configuration. The actual hoisting mechanism of a

* Corresponding author. e-mail: zmasoud@hu.edu.jo

container crane consists typically of a set of four hoisting cables arrangement. The cables are hoisted from four different points on a trolley and are attached on the payload side to four points on a spreader bar used to lift containers.

Cargo transfer control varies according to the crane application. For example, in one application large oscillations maybe acceptable during the transfer operation, however, the settling time, overshoot, and the magnitude of residual oscillations are kept minimal at the end of the transfer maneuver to allow for accurate cargo positioning. In other applications, such as nuclear reactors, or where the space around the crane is populated, the safety requirements are very strict. Thus large oscillations are not acceptable during and at the end of a transfer maneuver.

Input-shaping control is an old but still widely used strategy to control suspended objects in general, and container cranes in particular. Its effectiveness comes from the fact that it does not require alterations to the original structure of the crane, or the installation of additional mechanical hardware. However, these controllers are not generally robust. Their performance is very sensitive to changes in system parameters, time delays, external disturbances, and they require "highly accurate values of the system parameters" to achieve satisfactory system response [8–10]. While a good design can minimize the controller's sensitivity to changes in the payload mass, it is much harder to alleviate the controller's sensitivity to changes in the hoisting cable length.

Alsop et al. [11] were the first to propose a controller based on input-shaping. The controller was used to automate an ore unloader, by accelerating the trolley in steps of constant acceleration then killing the acceleration when the payload reaches zero oscillation angle (after multiples of a full oscillation period). The trolley then coasts at constant speed along the path for a period of time necessary to complete the transfer maneuver. A replicate of the acceleration procedure is used in the deceleration stage. The switching times for the acceleration and deceleration steps were calculated using an iterative computer procedure. They also used a linear frequency approximation of a simple pendulum model. Their results demonstrated very little residual oscillations, while transient oscillation angles were of order of 10° during the acceleration/deceleration stages.

Nonlinear frequency approximation of a simple pendulum was also used to improve the performance of the single-step controllers [12, 13]. Numerical simulations demonstrated that an acceleration profile based on the nonlinear frequency approximation can dampen the residual oscillations two orders of magnitude more than that based on a linear frequency approximation. The enhanced performance was most pronounced for longer coasting distances and higher accelerations.

Alzinger and Brozovic [14] showed that a double-step acceleration profile results in significant reductions in travel time over a single-step acceleration profile. Testing on an actual crane has shown that the double-step acceleration profile can deliver both faster travel and minimal payload oscillations at the target point.

Starr [15] used a symmetric double-step acceleration shaped profile to transport a suspended object with minimal oscillations. A linear approximation of the period of the payload is used to calculate the switching times and to generate an analytical expression for the acceleration profile. This work was later extended by employing a nonlinear approximation of the payload frequency to generate single-step and double-step symmetric acceleration profiles [16].

Using a new approach, Jansen, and Noakes [17] showed analytically that input-shaping is equivalent to a notch filter applied to a general input signal and centered around the natural frequency of the payload. They applied a second-order robust notch filter to shape the acceleration input. Numerical simulation and experimental verification of this strategy on an actual bidirectional gantry crane, moving under arbitrary step accelerations and changing cable length at a very slow constant rate, showed that the strategy was able to suppress residual payload oscillation. The work was extended by developing a command shaping notch filter to reduce payload oscillation on rotary cranes excited by the operator commands. It was reported that in general, there was no guarantee that applying such filter to the operator's commands would result in excitation terms having the desired frequency content, and that it only works for low speed and acceleration commands [18]. Results were later verified experimentally [19].

Singhose et al. [20] developed four different input-shaping controllers. They reported that the best controller produced a reduction of 73% in transient oscillations over the time-optimal rigid-body commands. However, they noticed that "transient deflection with shaping increases with hoist distance, but not as severely as the residual oscillations". The numerical simulations showed that "the percentage in reduction with shaping is dependent on system parameters". As a result, the four controllers suffered significant degradation in performance when applied to crane maneuvers that involved hoisting.

Daqaq et al. [21] developed a single-step input-shaping controller for quay-side container cranes. The controller was based on a four-bar-mechanism model of the crane [22, 23]. The model was simplified to a double-pendulum model with kinematic constraints. The method of multiple scales was used to find an analytical nonlinear expression for the period of oscillation in both the acceleration and coasting modes. They reported that a single-step input shaping controller based on a simple pendulum fails when applied to quay-side container cranes. In fact their results showed that such controller may amplify the residual oscillations to large magnitudes. On the other hand, numerical simulations showed that a controller based on the nonlinear frequency approximation of the double-pendulum model of the crane results in a superior performance. To increase the controller performance robustness, they combined the shaped commands with a nonlinear delayed-position feedback at the end of the transfer operation.

In this paper, a graphical phase plane approach is used to derive geometric constraints that are used to develop a double-step input-shaping controller that accounts for large hoisting operations. The graphically derived constraints are combined with physical constraints, then solved numerically for the switching times of the acceleration profile. The controller is based on a four-bar-mechanism model of the container crane. Switching times were

calculated using both linear and nonlinear frequency approximations of this model. Experiments were conducted on a 1:10 scaled model of a 65 ton quay-side container crane with a 7 m track and 3.5 m hoisting cables.

2. Mathematical Modeling

In this section, a four-bar-mechanism is developed to model the actual hoisting mechanism of the quay-side container crane capturing all dynamic and geometrical constraints of the mechanism. This model is later transformed to a double-pendulum model with kinematic constraints equivalent to those of the four-bar-mechanism model. However, numerical simulations are performed on the full model of the crane.

2.1. Full Model

Figure.2 shows a two-dimensional side projection of a quay-side container crane. This four-bar-mechanism is developed to model the actual dynamics of the hoisting mechanism of the crane. The container is grabbed using a spreader bar, which is then hoisted from the trolley by means of four cables, two of which are shown. The cables are spaced a distance d at the trolley and a distance w at the spreader bar. The hoisting cables in the model are treated as rigid massless inextensible links with variable lengths. The specific equations of these scleronomic holonomic constraints are

$$\Phi(\mathbf{q},t)=\begin{bmatrix}\left(x+R\sin\theta-\frac{1}{2}w\cos\theta-f+\frac{1}{2}d\right)^2\\ \quad+\left(y-R\cos\theta-\frac{1}{2}w\sin\theta\right)^2-L^2\\ \left(x+R\sin\theta-\frac{1}{2}w\cos\theta-f-\frac{1}{2}d\right)^2\\ \quad+\left(y-R\cos\theta+\frac{1}{2}w\sin\theta\right)^2-L^2\end{bmatrix}=0 \quad (1)$$

where $\mathbf{q}=[x,y,\theta]^T$ is the generalized coordinates vector.

Using the Lagrange multipliers, one can write the set of differential-algebraic equations DAE's [24] as

$$\begin{bmatrix}\mathbf{M} & \Phi_{\mathbf{q}}^T\\ \Phi_{\mathbf{q}} & 0\end{bmatrix}\begin{bmatrix}\ddot{\mathbf{q}}\\ \Lambda\end{bmatrix}=\begin{bmatrix}\mathbf{Q}^A\\ \Gamma\end{bmatrix} \quad (2)$$

where $\mathbf{M}=diag[m,m,m\bar{k}^2]$ is the inertia matrix, m is the mass of the load and the spreader bar, $\bar{k}$ is the combined radius of gyration of the load and spreader bar about point Q, $\mathbf{Q}^A=[0,-mg,0]^T$ is the generalized applied force vector, Λ are the Lagrange multipliers, and

$$\Gamma=-(\Phi_{\mathbf{q}}\dot{\mathbf{q}})_{\mathbf{q}}-2\Phi_{\mathbf{q}t}\dot{\mathbf{q}}-\Phi_{tt} \quad (3)$$

where the subscripts denote partial derivatives.

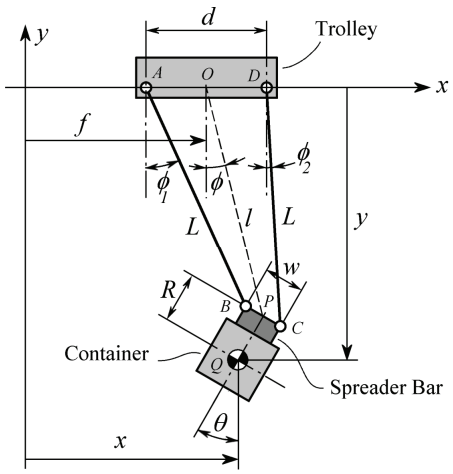

Figure 2: A schematic model of a container crane

2.2. Double-Pendulum Model

To better understand the dynamics of the system, and to derive analytical expression for the system frequency which is essential to the controller design, the four-bar-mechanism model is transformed into a double-pendulum system with a variable length cable l, a rigid body with a mass center at a distance R from the midjoint of the double pendulum, and a kinematic constraint relating the angles ϕ and θ as shown in Fig. 3.

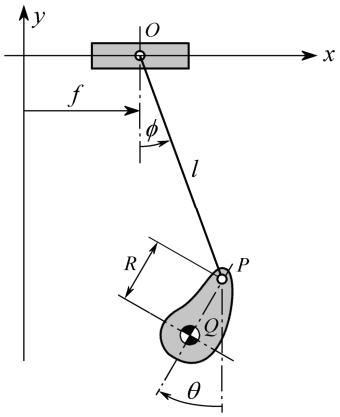

Figure 3: A schematic of a constrained double pendulum model of a container crane

Point O In Fig. 2 is the midpoint between points A and D, and point P is the midpoint between points B and C. The closing equations of the loop $ABPO$ are

$$l\sin\phi-\frac{1}{2}w\cos\theta+\frac{1}{2}d=L\sin\phi_1 \quad (4)$$

$$l\cos\phi-\frac{1}{2}w\sin\theta=L\cos\phi_1 \quad (5)$$

Similarly, the closing equations of the loop $ODCP$ can be written as

$$l\sin\phi+\frac{1}{2}w\cos\theta-\frac{1}{2}d=L\sin\phi_2 \quad (6)$$

$$l\cos\phi+\frac{1}{2}w\sin\theta=L\cos\phi_2 \tag{7}$$

Squaring and adding Eqs. (4) and (5), and squaring and adding Eqs. (6) and (7), we can eliminate L, ϕ_1, and ϕ_2 from the resulting equations and obtain the following relations

$$\theta=-\phi+\sin^{-1}\left(\frac{d}{w}\sin\phi\right) \tag{8}$$

$$l=\sqrt{L^2-\frac{1}{4}(d^2+w^2-2dw\cos\theta)} \tag{9}$$

Equation (8) represents the kinematic constraint between the angles ϕ and θ. Applying Eqs. (8) and (9) to the double-pendulum model results in a kinematic behavior identical to the four-bar-mechanism model. The position vector to the center of mass of the payload of the constrained double pendulum is

$$\mathbf{r}=(f+l\sin\phi-R\sin\theta)\mathbf{i}-(l\cos\phi+R\cos\theta)\mathbf{j} \tag{10}$$

Using Eq. (10), we write the kinetic and potential energies of the constrained double pendulum as

$$\begin{aligned}T=&\frac{1}{2}ml^2\dot{\phi}^2+\frac{1}{2}m(\bar{k}^2+R^2)\dot{\theta}^2+\frac{1}{2}m\dot{f}^2\\&-mRl\dot{\phi}\dot{\theta}\cos(\phi+\theta)+ml\dot{\phi}\dot{f}\cos\phi-mR\dot{\theta}\dot{f}\cos\theta\end{aligned} \tag{11}$$

$$V=-mg(l\cos\phi+R\cos\theta) \tag{12}$$

Substituting the constraint Eqs. (8) and (9) into Eqs. (11) and (12) results in the elimination of θ from the energy expressions of the system. To derive the equation of motion that describes the time variation of ϕ, the Euler-Lagrange equations are used which are given as

$$\frac{d}{dt}\left(\frac{\partial\mathcal{L}}{\partial\dot{\phi}}\right)-\frac{\partial\mathcal{L}}{\partial\phi}=0 \tag{13}$$

where $\mathcal{L}=T-V$. Substituting Eqs. (11) and (12) in Eq. (13) results in the full nonlinear equation of motion for the double pendulum model. Due to the lengthy expressions in this equation, only the linear first order expansion is shown as

$$\ddot{\phi}+2\mu\dot{\phi}+\omega_o^2\phi+\frac{\mu}{2\dot{L}}\ddot{f}=0 \tag{14}$$

where

$$\begin{aligned}\omega_o^2&=\frac{g(L+a^2R)-a\dfrac{dR\ddot{L}}{w}}{L^2-2aRL+a^2(\bar{k}^2+R^2)}\\\mu&=\frac{\dot{L}(L-aR)}{L^2-2aRL+a^2(\bar{k}^2+R^2)}\\a&=\frac{d-w}{w}\end{aligned} \tag{15}$$

In the above linear approximation, we assume that $l\approx L$. For small angles of oscillation ϕ, this assumption results in a maximum error of 1% in calculating the length l based on typical values of d, w, and L for container cranes.

3. Controller Design

Analyzing the dynamics involved in Eq. (14) forms a basis for designing the double-step input-shaping controller. To find the equilibrium solution, ϕ_L, we let $\dot{\phi}=\ddot{\phi}=0$ in Eq. (14) to get

$$\phi_L=-\frac{L-aR}{g(L+a^2R)-a\dfrac{dR\ddot{L}}{w}}\ddot{f} \tag{16}$$

For constant cable length operations, $\dot{L}=\ddot{L}=0$, the linearized system has a single stationary fixed-point given by

$$\phi_o=-\frac{L-aR}{g(L+a^2R)}\ddot{f} \tag{17}$$

This equilibrium solution is a marginally stable center. For constant L, the solution of Eq. (14) is illustrated in the phase portraits shown in Fig. 4(a). The figure shows that the solution is periodic with the payload exhibiting a limit cycle behavior. The center of the resulting limit cycle along the ϕ axis is determined by the amplitude and sign of the equilibrium solution ϕ_o. The radius of the resulting limit cycle is determined by the payload initial angular displacement and velocity.

For operations that involve hoisting, the dynamic behavior of the payload is qualitatively different. The variation of L causes the equilibrium solution described by Eq. (16) to vary along the ϕ axis. This kind of equilibrium solution is known as a non-stationary equilibrium point. Moreover, in the case of hoisting ($\dot{L}\neq0$) the term including $\dot{\phi}$ in Eq. (14) is no longer equal to zero. This term will act as a damping term with the sign of $\dot{L}$ determining the type of damping. The equilibrium solution of Eq. (14) is no longer a marginally stable center. The stability of this equilibrium solution is now determined by the sign of $\dot{L}$. For a positive $\dot{L}$, the damping is positive and the equilibrium solution is a stable focus (sink). On the other hand, for a negative $\dot{L}$, the damping is negative and the equilibrium solution is an unstable focus (source). The qualitative dynamic behavior of the payload around the non-stationary equilibrium solution is illustrated in Fig. 4(b) and Fig. 4(c).

Figure 5 shows a typical acceleration profile for a double-step input-shaping controller. The trolley accelerates at a constant rate of a_{max} for time t_{a1}, after which the trolley coasts at a constant velocity until time t_{c1}. The trolley then accelerates again with the same acceleration amplitude a_{max} until time t_{a2} at which the acceleration phase is concluded. Afterwards, the trolley coasts until time T, then decelerates in two steps similar to the acceleration stage. The switching times of the acceleration phase are calculated so that the trolley reaches the design velocity with zero payload oscillations. Similarly, the switching times of the deceleration phase are calculated so that the payload oscillations caused by the trolley deceleration are eliminated at the trolley stop.

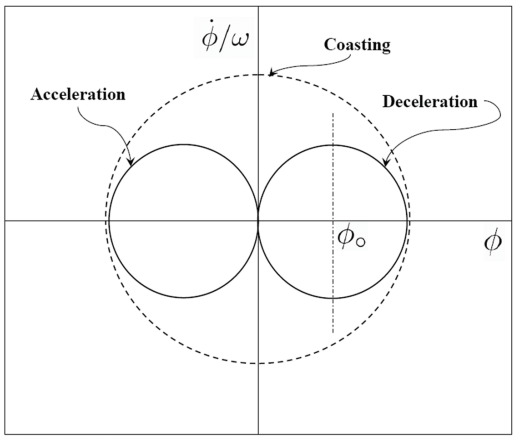

(a) $\dot{L} = 0$.

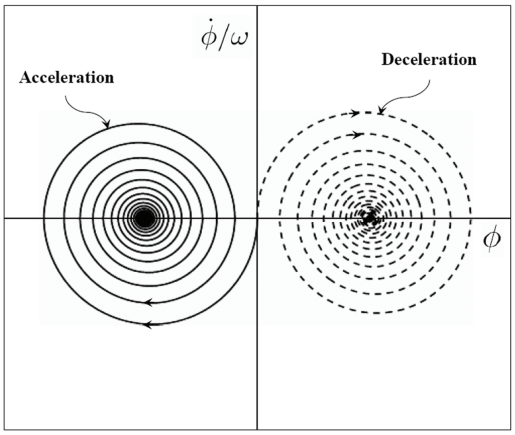

(b) $\dot{L} > 0$.

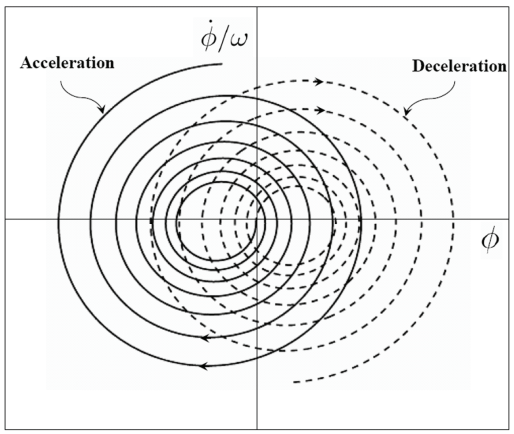

(c) $\dot{L} < 0$.

Figure 4: Phase portraits describing the dynamics of the crane payload

The shaped double-step acceleration profile like the one shown in Fig. 5 uses the maximum system capabilities (acceleration and speed) to achieve the required transfer maneuver with minimal transient and residual oscillations. To generate the required profile, the switching times are calculated such that the payload dynamics follow the phase portrait shown in Fig. 6. Ideally, this phase portrait drives the dynamics of the payload to end at the equilibrium point at the center of the phase portrait rather than a limit cycle around it.

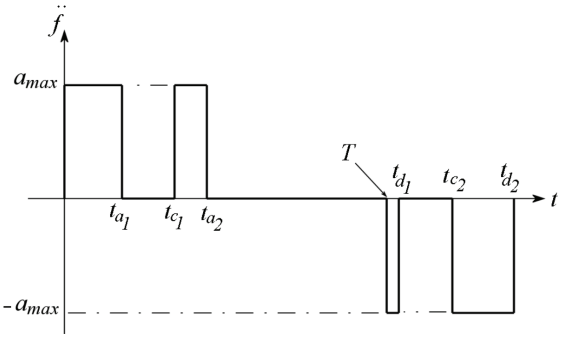

Figure 5: Typical acceleration profile of a double-step input-shaping controller

To determine the switching times for the required phase portrait, the trolley acceleration profile must satisfy two sets of constraints. The first set includes the dynamic constraints that involve the amplitudes of the response at the beginning and at the end of each acceleration step, and the physical constraints on the crane motors. The second set includes geometrical constraints derived from the phase portrait of the shaped acceleration and deceleration profiles.

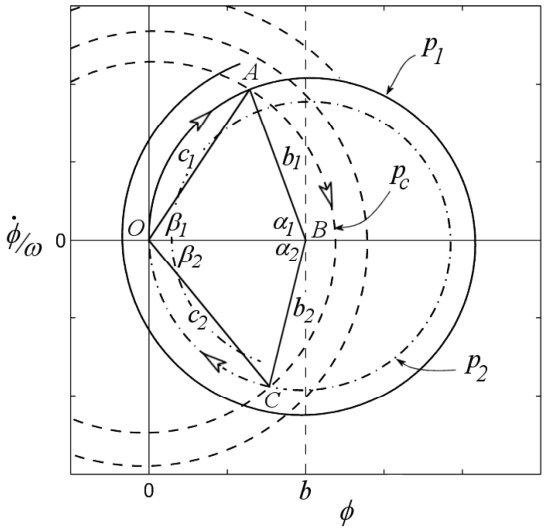

Figure 6: Graphical representation of the controller phase portrait.

Since L is slowly varying when compared to ϕ, the damping term associated with $\dot{\phi}$ can be treated as constant when analyzing the fast dynamics of the system for short periods of time. This assumption does not imply slow cable hoisting. The variation of L is only slow when compared to the fast variation of the angle ϕ. Hence, to derive these dynamic constraints, we assume that the system response is exponentially damped. Furthermore, for typical crane parameters and operating range of the hoisting cable, the equilibrium solution is assumed stationary. An average damping is used over each acceleration and coasting step as

$$\mu_{ave} = \frac{1}{t_2 - t_1} \int_{t_1}^{t_2} \mu(\tau)\, d\tau \qquad (18)$$

In the first acceleration step, the trolley accelerates so that the new equilibrium solution is at point *B*, Fig. 6. The response follows the path p_1 through a phase angle α_1 to point *A*. The amplitude of the response at that point is

$$b_1 = b\,\mathrm{e}^{\mu_{ave} t_{a1}} \tag{19}$$

The second acceleration step t_{c1} to t_{a2} is designed to force the response of the system to home at the origin of the phase portrait at the end of this acceleration step. The system response follows the path p_2 through the phase angle α_2. Going back in time, the starting amplitude of oscillation of the second acceleration step at point *C* has to satisfy

$$b_2 = b\,\mathrm{e}^{-\mu_{ave}(t_{a2} - t_{c1})} \tag{20}$$

To guarantee the continuity of the response, points *A* and *C* are required to fall on the same coasting path p_c in the phase portrait. This can be represented by the following relation

$$c_2 = c_1\,\mathrm{e}^{-\mu_{ave}(t_{c_1} - t_{a_1})} \tag{21}$$

Equations (19), (20), and (21) represent the first three equations of the dynamics set of constraints. The fourth dynamic constraint is derived from the physical limitations on the velocity and acceleration achievable by the trolley motors. This constraint can be enforced by restricting the acceleration time so that the trolley velocity does not exceed the maximum achievable velocity by the trolley motors.

$$v_{max} = a_{max}(t_{a_1} + t_{a_2} - t_{c_1}) \tag{22}$$

The second set of constraints is derived directly from the graphical representation of the controller phase portrait, Fig. 6. Graphically, the coasting phase is split into two consecutive stages: β_1 and β_2. The first phase ends when the response crosses the zero velocity axis on the phase portrait at time t_o. Considering the upper triangle *OAB*, and using the geometric laws of sines and cosines, the following geometric constraints are obtained

$$c_1^2 = b^2 + b_1^2 - 2bb_1 \cos\alpha_1 \tag{23}$$

$$c_1 = b_1 \frac{\sin\alpha_1}{\sin\beta_1} \tag{24}$$

Similarly, considering the lower triangle *OCB*, two geometric constraints are also derived as

$$c_2^2 = b^2 + b_2^2 - 2bb_2 \cos\alpha_2 \tag{25}$$

$$c_2 = b_2 \frac{\sin\alpha_2}{\sin\beta_2} \tag{26}$$

The phase angles of the controlled performance in the acceleration and coasting phases can be related to the system frequencies and switching times by the following equations

$$\alpha_1 = \int_0^{t_{a1}} \omega_a\,dt \tag{27}$$

$$\alpha_2 = \int_{t_{c1}}^{t_{a2}} \omega_a\,dt \tag{28}$$

$$\beta_1 = \int_{t_{a1}}^{t_o} \omega_c\,dt \tag{29}$$

$$\beta_2 = \int_{t_o}^{t_{c1}} \omega_a\,dt \tag{30}$$

where ω_a and ω_c are the frequency of payload oscillations in the accelerations and coasting stages, respectively. When a linear frequency approximation is used, $\omega_a = \omega_c = \omega_o$.

The constraint equations Eqs. (19) – (26) can be reduced to four equations in terms of the unknown switching times t_{a1}, t_o, t_{c1}, and t_{a2} by substituting Eqs. (19), (24), (27), and (29) into Eq. (23)

$$\mathrm{e}^{2\mu_{ave}t_{a1}} \frac{\sin^2\left(\int_0^{t_{a1}} \omega_a\,dt\right)}{\sin^2\left(\int_{t_{a1}}^{t_o} \omega_c\,dt\right)} = 1 + \mathrm{e}^{2\mu_{ave}t_{a1}} - 2\,\mathrm{e}^{\mu_{ave}t_{a1}} \cos\left(\int_0^{t_{a1}} \omega_a\,dt\right) \tag{31}$$

Similarly, Eqs. (20), (26), (28), and (30) are substituted into Eq. (25) to get

$$\mathrm{e}^{-2\mu_{ave}(t_{a2} - t_{c1})} \frac{\sin^2\left(\int_{t_{c1}}^{t_{a2}} \omega_a\,dt\right)}{\sin^2\left(\int_{t_o}^{t_{c1}} \omega_c\,dt\right)} = 1 + \mathrm{e}^{-2\mu_{ave}(t_{a2} - t_{c1})} - 2\,\mathrm{e}^{-\mu_{ave}(t_{a2} - t_{c1})} \cos\left(\int_{t_{c1}}^{t_{a2}} \omega_a\,dt\right) \tag{32}$$

Equations (19), (20), (24), (26), and (27) – (30) are also substituted into Eq. (21)

$$\mathrm{e}^{-\mu_{ave}t_{a2}} \frac{\sin\left(\int_{t_{c1}}^{t_{a2}} \omega_a\,dt\right)}{\sin\left(\int_{t_o}^{t_{c1}} \omega_c\,dt\right)} = \frac{\sin\left(\int_{t_o}^{t_{a1}} \omega_a\,dt\right)}{\sin\left(\int_{t_{a1}}^{t_o} \omega_c\,dt\right)} \tag{33}$$

The final set of four constraint equations Eqs. (22), and Eqs. (31) – (33) are then numerically solved for the switching times of the controller. This approach is used for both the acceleration and deceleration stages. The trolley coasting time between the acceleration and deceleration stages is determined by the total travel distance of the trolley.

4. Numerical Simulations

To simplify the calculations, the following simulations are designed so that the trolley acceleration stages fall within the constant hoisting speed stage. This is done to avoid discontinuities in the hoisting profile which results from the square hoist acceleration profile. This approach speeds up the calculation time to the point where it becomes feasible to implement this approach on standard PLC controllers used on quay-side container cranes. The maximum hoisting acceleration used in these simulations is 0.75 m/s^2 and the maximum hoisting velocity is 1.5 m/s. In the numerical simulations the following crane dimensions are used: d = 2.82 m, w = 1.41 m, R = 2.5 m, and $\bar{k}$ = 1.0 m. The payload mass is m = 50,000 kg.

Using the linear frequency approximation Eq. (15) a shaped double-step acceleration profile is generated for a fixed cable-length transfer operation. The resulting profile is applied to the full model equations of motion Eqs. (2). The numerically simulated response is shown in Fig. 7.

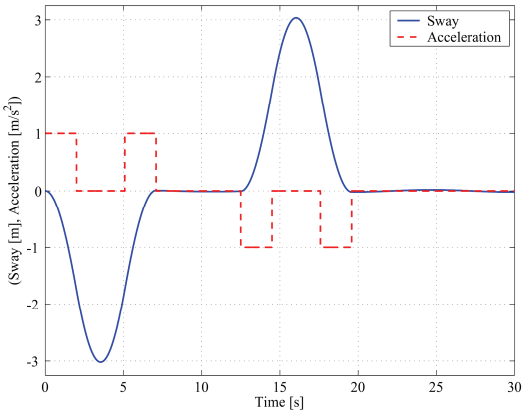

(a) Payload sway and trolley acceleration

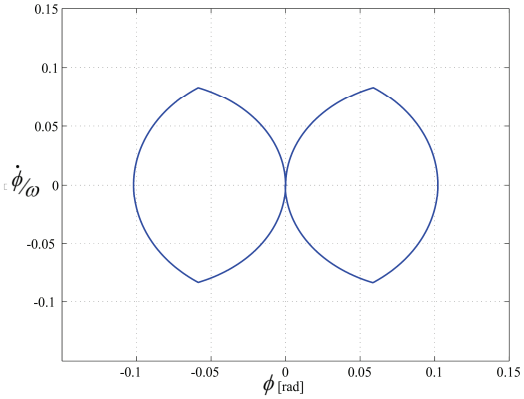

(b) Phase portrait of the response

Figure 7: Sway response of a container crane to shaped operator commands. Results are obtained for L = 32.5 m, S = 50 m

Daqaq et. al. [21] reported that for single-step input shaping control strategy, a controller based on a nonlinear frequency approximation of the payload oscillations results in a superior performance when compared to that based on a linear approximation. To check the effect of using a nonlinear frequency approximation on the performance of the double-step input-shaping controller, we will use the linear frequency approximation and the nonlinear frequency approximation developed earlier [21]. The nonlinear approximation is dependent on the oscillation amplitude and the trolley acceleration, hence $\omega_a \neq \omega_c \neq \omega_o$.

Figure. 8 illustrates a comparison between the performance of the double-step input-shaping controller using the linear and nonlinear frequency approximations. The amplitude of the residual oscillation resulting from a linear frequency approximation is larger than that resulting from a nonlinear approximation. However, in contrast with the single-step input-shaping controller where the difference is as large as 10 orders of magnitude, the difference here is very small and can be tolerated. This is due to the fact that using the double-step profile the period over which large oscillations occur is so short that the effects of the difference between the linear and nonlinear frequency approximations does not yield significant deviation from the desired system dynamics.

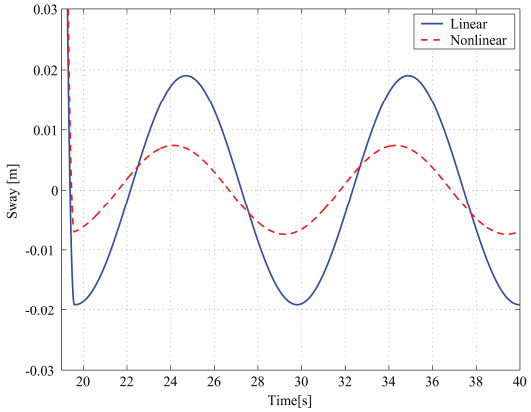

Figure 8: Residual oscillations of the payload resulting from a double-step input-shaping controller, L = 32:5 m, and S = 50 m

Several transfer maneuvers are simulated, three of which are presented here to demonstrate a hoisting up, lowering, and a combined hoisting up and lowering maneuvers. In the first simulation, the payload is transferred a distance of 50 m. During the transfer operation the payload is hoisted up 15 m starting from a position 35 m below the trolley with an acceleration of 0.75 m/s^2, after the hoist acceleration is concluded in the first two seconds, the trolley starts to accelerate with a maximum acceleration of 0.5 m/s^2 to reach a maximum velocity of 3 m/s, Fig. 9(a). The payload motion trajectory is shown in Fig. 9(b), and the controller switching times are listed in Table 1. The total payload transfer operation is conducted in 25.6 seconds. The maximum oscillation magnitude after the acceleration stage is 12.2 mm, and 15.4 mm at the end of the transfer maneuver. Figures 9(c) and 9(d) show the phase portrait of the system and the payload oscillation throughout the transfer maneuver.

Table 1: Switching times for a hoisting maneuver from L_i to L_f.

L_i (m)	L_f (m)	t_{a1} (sec)	t_o (sec)	t_{c1} (sec)	t_{a2} (sec)
35	20	2.5762	3.6751	3.9538	7.3777
20	20	3.0000	3.1859	3.3717	6.3717
20	25	3.3145	3.4186	3.9776	6.6632
20	35	3.4601	3.6677	4.7279	7.2678

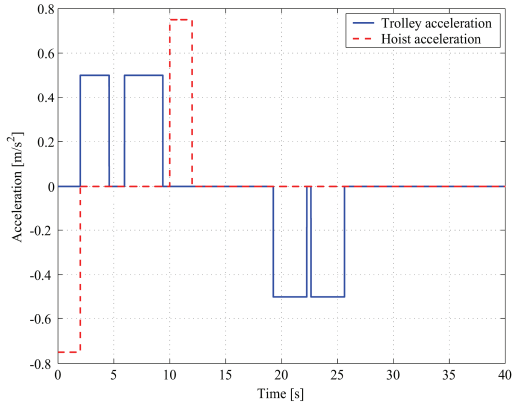

(a) Trolley and hoist accelerations

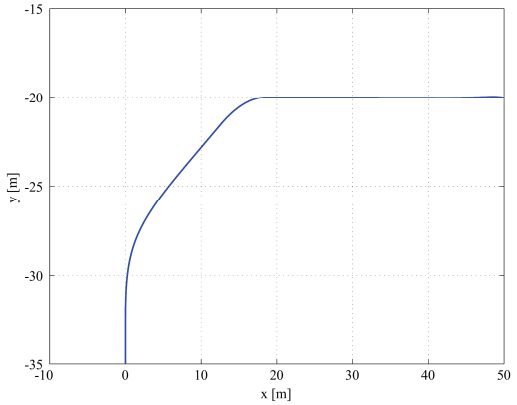

(b) Motion profile

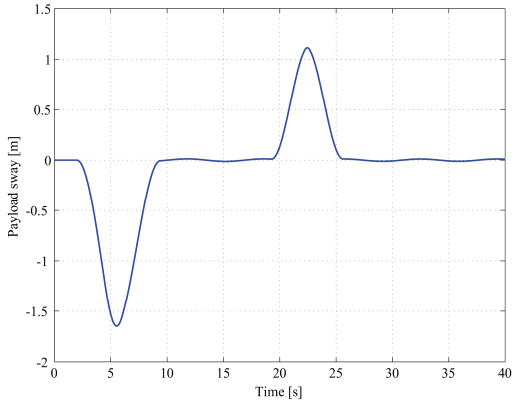

(c) Payload sway

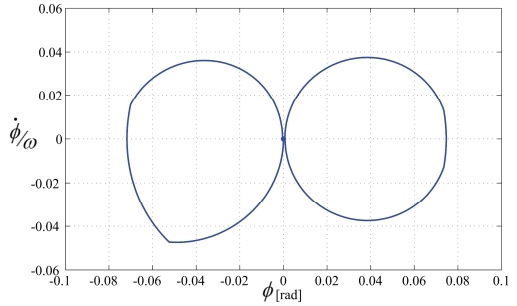

(d) Phase portrait

Figure 9: A transfer operation involving a 15 m hoisting

In the second simulation, the payload is transferred 50 m starting from a position 20 m below the trolley. During the transfer operation the payload is lowered 15 m with an acceleration of 0.75 m/s^2, Fig. 10(a). The payload motion trajectory is shown in Fig. 10(b). The system performance is shown in Fig. 10(c) and Fig. 10(d). The total transfer operation is concluded in 26.3 seconds. The magnitude of the resulting payload oscillations after the acceleration stage is 12.5 mm and 11.4 mm at the end of the transfer maneuver.

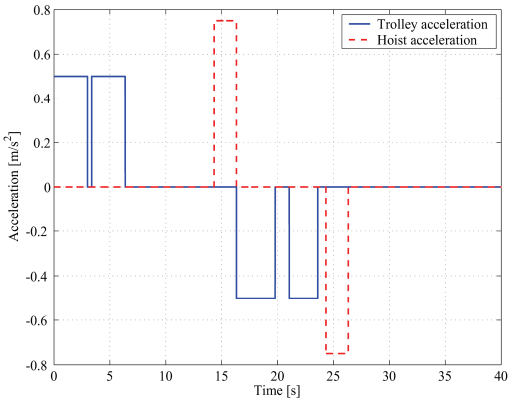

(a) Trolley and hoist accelerations

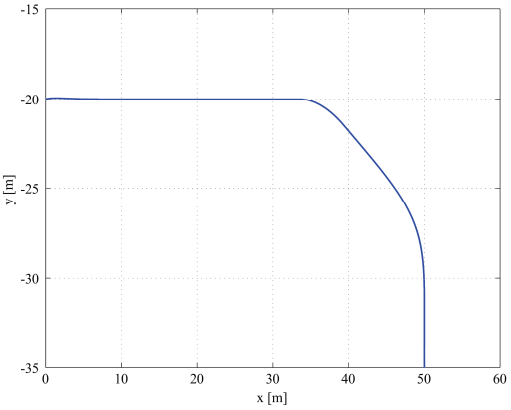

(b) Motion profile

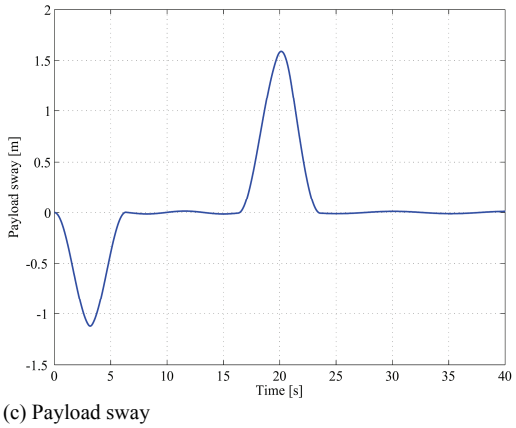

(c) Payload sway

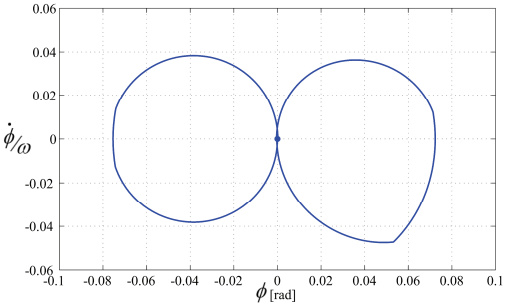

(d) Phase portrait

Figure 10: A transfer operation involving a 15 m lowering

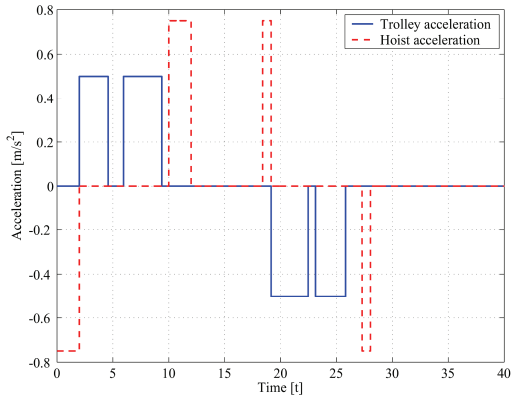

(a) Trolley and hoist accelerations

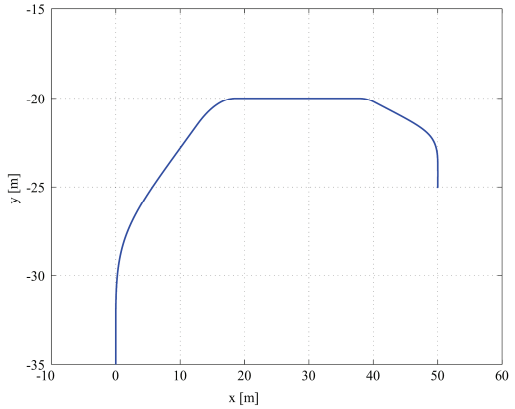

(b) Motion profile

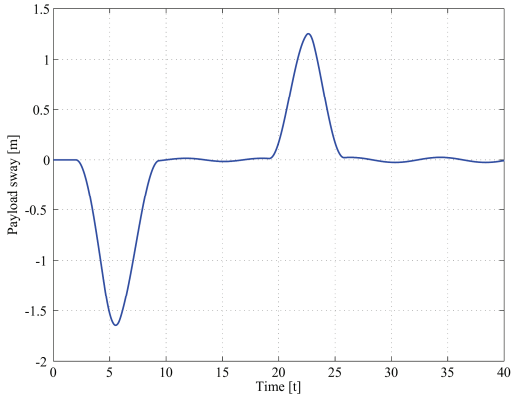

(c) Payload sway

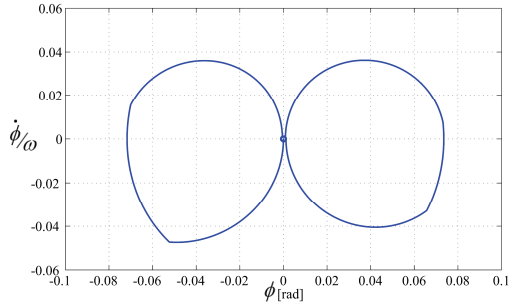

(d) Phase portrait

Figure 11: A transfer operation involving a 15 m hoisting and a 5 m lowering

In the third simulation, the payload is transferred 50 m starting from a position 35 m below the trolley. During the transfer operation the payload is hoisted up 15 m then lowered 5 m, Fig. 11(b). The system performance is shown in Fig. 11(c) and. 11(d). The total transfer operation is concluded in 28 seconds. The magnitude of the resulting payload oscillations after the acceleration stage is 15.4 mm and 25 mm at the end of the transfer maneuver.

5. Experimental Testing

To validate the controller design approach and the numerical simulations, a 1:10 scale model of a 65 ton quay-side container crane was constructed, as shown in Fig. 12. The support mechanism consists of two 7 m tracks and a trolley driven by a DC brushless servomotor. The motor has a 4000 *rpm* rated speed, 510 N.m continuous torque, and 1.5 *hp* rated power. The hoist mechanism consists of four steel cables connected to four aluminum pulleys on the trolley and to four points on the spreader bar. The spreader bar is attached to a 1:10 scale model of a standard 20 ft container. The four pulleys are driven using two DC brushless servomotors.

Several tests were conducted. Two tests are presented here. Two performance factors are used as measures for the controller performance. The first is that the controller incorporates the maximum crane speeds and accelerations, which guarantees the conclusion of the transfer maneuver in minimal time. The second is that the magnitude of the residual oscillations is less than 5 mm (equivalent to 50 mm on the full scale crane) at the end of the transfer maneuver.

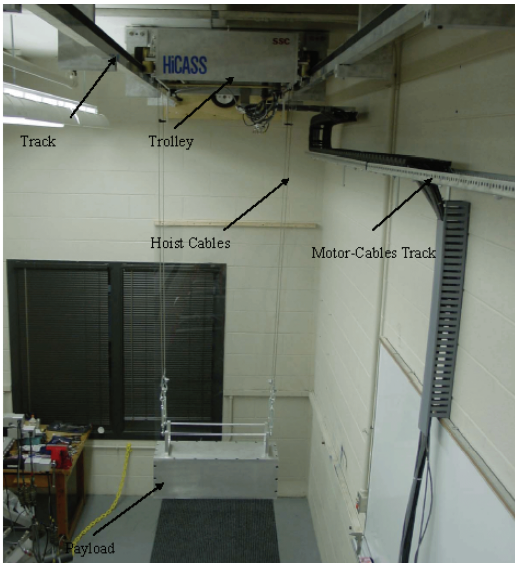

Figure 12: A 1:10 scale model of a 65-ton quay-side container crane

In the first test, the trolley travels a distance of 5 m. During the transfer maneuver, the payload is lowered 1.5 m starting from a position 2 m below the trolley with an acceleration of 0.5 m/s^2. The payload motion trajectory is shown in Fig. 13(a). The trolley starts to accelerate with a maximum acceleration of 0.5 m/s^2 to reach a maximum velocity of 1 m/s, Fig. 13(b). The total transfer maneuver is concluded in 8.4 seconds. At the end of the acceleration phase of the maneuver, the maximum magnitude of oscillations was less than 4 mm. When the transfer

maneuver was concluded, the maximum magnitude of the residual oscillations was less than 4.5 mm. Figure 13(c) illustrates the payload sway throughout the transfer maneuver.

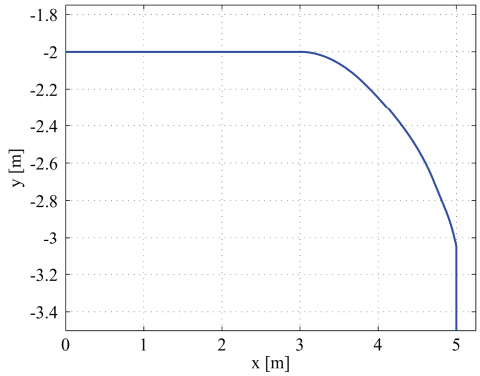

(a) Motion profile

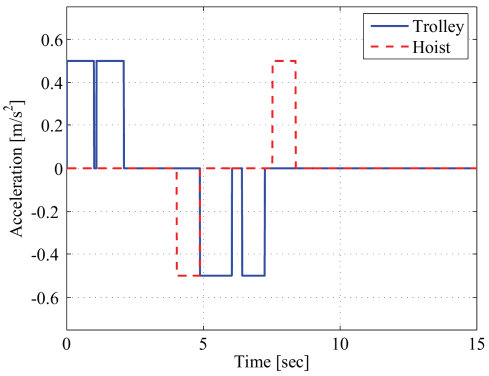

(b) Trolley and hoist accelerations

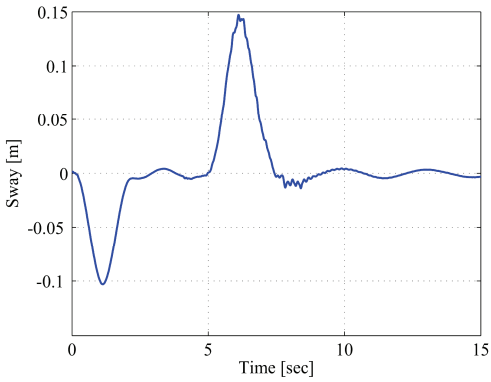

(c) Payload sway

Figure 13: A 5 m payload transfer operation involving a 1.5 m lowering

In the second test, the payload is moved a distance of 5 m. During the transfer maneuver, the payload is first hoisted up 1.5 m starting from a position 3.5 m below the trolley, travels for a short time, and is then lowered 1.5 m. The payload motion trajectory is shown in Fig. 14(a). The trolley starts to accelerate with a maximum acceleration of 0.5 m/s^2 to reach a maximum velocity of 1 m/s and the payload is hoisted and lowered with a maximum acceleration of 0.5 m/s^2 to reach a maximum speed of 1 m/s, Fig. 14(b). The total transfer maneuver is concluded in 9.2 seconds. The maximum magnitude of oscillations was less than 4.2 mm at the end of the acceleration stage and less than 4.5 mm at the end of the transfer maneuver. Figure 14(c) illustrates the payload sway throughout the transfer maneuver.

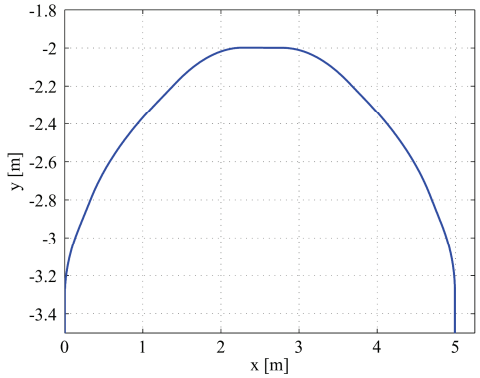

(a) Motion profile

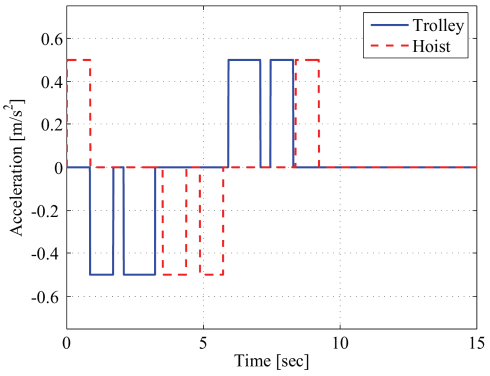

(b) Trolley and hoist accelerations

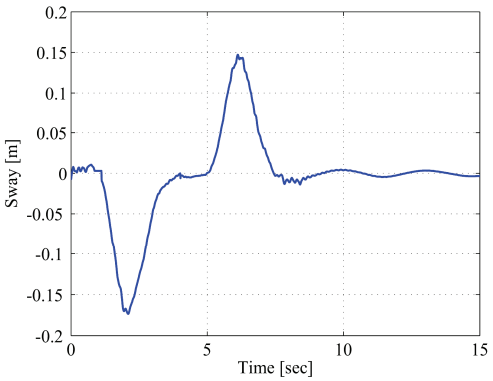

(c) Payload sway

Figure 14: A 5 m payload transfer operation involving a 1.5 m hoisting then 1.5 m lowering

Many other tests were conducted involving different hoisting and lowering maneuvers. In all cases, the residual oscillations were less than 5 mm in magnitude.

6. Conclusions Remarks

A double-step input-shaping controller is developed for sway oscillation control of quay-side container crane operations that involve large hoisting maneuvers. This approach is based on the graphical representation of the phase portrait that describes the response of the payload of a container crane to a double-step acceleration profile.

During operations involving large hoist speeds and distances, the quasi-static approach to system modeling fails, especially for open-loop control systems, which require accurate and proper system identification. The hoisting speed has a significant effect on the system frequency and the dynamic response of the payload. Hoisting can either excite or dampen oscillations depending on the direction of the hoisting action.

Double-step input-shaping controllers are less sensitive to the nonlinearity of the frequency approximation. The short acceleration times made possible by the ability of the controller to utilize the maximum crane acceleration and speed makes using a linear approximation of the frequency sufficient for switching times calculations. However, simple pendulum frequency approximation is far from the actual frequency of quay-side container cranes. In fact, the frequency approximation must be based on a model that includes the multi-cable hoisting mechanism of the crane. The approximation used in this work was derived using a four-bar-mechanism model of the hoisting system of the crane and carried sufficient accuracy for input-shaping control design purposes.

The performance predicted by the numerical simulations of this work was validated experimentally on a 1:10 scaled model of a 65 ton quay-side container crane. Negligible differences in the amplitudes of the residual oscillations in the simulations and experiments were observed due to unmodeled friction and the fact that the hoisting cables are wrapped around pulleys rather than attached to “points” on the trolley.

Both numerical and experimental tests satisfied the shipping industry standard of less that 50 mm of sway for accurate container positioning.

References

[1] Abdel-Rahman, E. M., Nayfeh, A. H., and Masoud, Z. N., Dynamics and Control of Cranes: A Review, Journal of Vibrations and Control, 44, 2003, 863-908.

[2] d'Andrea-Novel, B., Boustany, F., and Conrad, F., Control of an Overhead Crane: Stabilization of Flexibilities, in Boundary Control and Boundary Variation: Proceedings of the IFIP WG 7.2 Conference, Sofia Antipolis, France, 1990, 1-26.

[3] d'Andrea-Novel, B., Boustany, F., Conrad, F., and Rao, B. P., Feedback stabilization of a hybrid PDE-ODE system: Application to an overhead crane, Mathematics of Controls, Signals, and Systems, 7, 1994, 1-22.

[4] d'Andrea-Novel, B., Boustany, F., Control of an Overhead Crane: Feedback Stabilization of a Hybrid PDE-ODE System: in Proceedings of the 1st European Control Conference: ECC 91, Grenoble, France, 1991, 2244-2249.

[5] Joshi, S. and Rahn, C. D., Position Control of a Flexible Cable of a Gantry Crane: Theory and Experiment, in Proceedings of the American Control Conference, Seattle, WA, 1995, 301-305.

[6] Martindale, S. C., Dawson, D. M., Zhu, J., and Rahn, C. D., Approximate Nonlinear Control for a Two Degree of Freedom Overhead Crane: Theory and Experimentation, in *Proceedings of the American Control Conference,* Seattle, WA, 1995, 301-305.

[7] Rahn, C. D., Zhang, F., Joshi, S., and Dawson, D. M., Asymptotically Stabilizing Angle Feedback for a Flexible Cable Gantry Crane, *Journal of Dynamic Systems, Measurement, and Control, 15*, 1999, 563-566.

[8] Zinober, A. S. I., The Self-Adaptive Control of an Overhead Crane Operations, in *Proc. of the 5th IFAC Symposium on Identification and System Parameter Estimation,* Darmstadt, East Germany, 1979, 1161-1167.

[9] Virkkunen, J. and Marttinen, A., Computer control of a loading bridge, in *Proceedings of the IEE International Conference: Control '88,* Oxford, UK, 1988, 484-488.

[10] Yoon, J. S., Park, B. S., Lee, J. S., and Park, H. S., Various control schemes for implementation of the anti-swing crane, in *Proceedings of the ANS 6th Topical Meeting on Robotics and Remote Systems,* Monterey, CA, 1995, 472-479.

[11] Alsop, C. F., Forster, G. A., and Holmes, F. R., Ore Unloader Automation - A Feasibility study, in *Proc. of IFAC Workshop on Systems Engineering for Control Systems,* Tokyo, Japan, 1965, 295-305.

[12] Jones, J. F. and Petterson, B. J., Oscillation damped movement of suspended objects, in *Proc. of the IEEE International Conference on Robotics and Automation,* Philadelphia, PA, 1988, 956-962.

[13] Dadone, P. , and Vanlandinham, H. F., Load Transfer Control for a Gantry Crane with Arbitrary Delay Constraints, *Journal of Vibration and Control, 7*, 2001, 135-158.

[14] Alzinger, E., and Brozovic, V., Automation and Control System for Grab Cranes, *Brown Boveri Review,Vol. 7*, 1983, 351-356.

[15] Starr, G. P., Swing-free transport of suspended objects with a path-controlled robot manipulator, *Journal of Dynamic Systems, Measurement, and Control, 107*, 1985, 97-100.

[16] Strip, D. R., Swing-free transport of suspended objects: A general treatment, *IEEE Transactions on Robotics and Automation, 5(2)*, 1989, 234{236.

[17] Kress, R. L., Jansen, J. F., and Noakes, M. W., Experimental implementation of a robust damped-oscillation control algorithm on a full-sized, two-degree-of-freedom, AC induction motor-driven crane, in *Proceedings of the 5th International Symposium on Robotics and Manufacturing: Research, Education, and Applications: ISRAM'94,* Maui, HI, 1994, 585-592.

[18] Parker, G. G., Groom, K., Hurtado, J., Robinett, R. D., and Leban, F., Command shaping boom crane control system with nonlinear inputs, in *Proceedings of the IEEE International Conference on Control Applications, 2*, Kohala Coast, HI, 1999, 1774-1778.

[19] Parker, G. G., Groom, K., Hurtado, J. E., Feddema, J., Robinett, R. D., and Leban, F., Experimental verification of a command shaping boom crane control system, in *Proceedings of the American Control Conference, 1*,San Diego, CA, 1999, 86-90.

[20] Singhose, W. E., Porter, L. J., and Seering, W. P., Input shaped control of a planar crane with hoisting, in *Proceedings of the American Control Conference,* Albuquerque, NM, 1997, 97-100.

[21] Daqaq, M. F., Masoud Z. N., and Nayfeh, A. H., Nonlinear Modeling and Control of Quay-Side Container Cranes, in *Proceedings of The IMAC-XXIII Conference and Exposition on Structural Dynamics,* Orlando, Fl, 2005.

[22] Masoud, Z., and Nayfeh, A. H., Sway Reduction on Container Cranes Using Delayed Feedback Controller, in *Proceedings of the AIAA,* Denver, CO, 2002.

[23] Masoud, Z., and Nayfeh, A. H., Sway Reduction on Container Cranes Using Delayed Feedback Controller, *Nonlinear Dynamics, 34 (3-4)*, 2003, 347-358.

[24] Blajer, W., and Kolodziejczyk, A., A geometric approach to solving problems of control constraints: theory and a DAE framework, in *Multibody Syst. Dyn.Vol.11,No.4*, 2004, 343-364.

التقديم

إنه لمن دواعي سروري أن أكتب هذه المقدمة بمناسبة صدور العدد الأول من المجلد الأول من المجلة الأردنية للهندسة الميكانيكية والصناعية (Jordan Journal of Mechanical and Industrial Engineering)، وهي مجلة علمية عالمية محكمة و مفهرسة، تصدر أربع مرات في العام عن اللجنة العليا للبحث العلمي في وزارة التعليم العالي والبحث العلمي في المملكة الأردنية الهاشمية. ويشرف على إعداد و نشر هذه المجلة عمادة البحث العلمي والدراسات العليا في الجامعة الهاشمية.

تحرص هيئة التحرير للمجلة الأردنية للهندسة الميكانيكية والصناعية أن تكون مرجعاً مهماً للدارسين والباحثين، يستنيرون بما ستتضمنه من بحوث أكاديمية أصيلة ودراسات علمية عميقة في شتى موضوعات الهندسة الميكانيكية والصناعية. وتسعى هيئة التحرير ومن خلال دعم وزارة التعليم العالي والبحث العلمي والجامعات الأردنية كافة المتواصل أن تصل هذه المجلة إلى مرتبة متقدمة ضمن المجلات العلمية العالمية المتخصصة في هذا المجال.

إننا نتمنى أن تشكل هذه المجلة قاعدة أساسية ترفد عملية النشر والبحث العملي في قطاعات الهندسة الميكانيكية والصناعية المتعددة، وتضع آخر ما توصلت إليه الأبحاث العلمية في متناول أيدي الباحثين والمتخصصين. وتنشر المجلة مقالات البحوث العلمية التي تتسم بالجدة والأصالة، إضافةً إلى الملاحظات الفنية و التقنية ومقالات المراجعة لموضوعات حيوية و تهم الدارسين و الباحثين و المهندسين العاملين في مختلف حقول الهندسة الميكانيكية و الصناعية. ويجري تحكيم مقالات البحوث والملاحظات التقنية من قبل ثلاثة محكمّين من ذوي الاختصاص والخبرة، وتشجع المجلة الباحثين على اقتراح أسماء بعض المحكمّين الأكفاء.

يشتمل العدد الأول على سبعة مقالات أبحاث أصيلة تعالج جوانب متعددة في الهندسة الميكانيكية والصناعية (1) دراسة أثر العوامل المختلفة على خشونة السطح خلال عمليات الخراطة النهائية، (2) تقييم الطاقة المستفادة من محطات التوربينات الغازية عند استخدام أنظمة تبريد مختلفة للهواء الداخل، (3) نظام مراقبة عشوائي لعملية البثق، (4) أثر عمق طبقة الماء على اداء مقطره شمسية، (5) نموذج غير خطي ديناميكي لمجمعة تروس مع أعمدة مرنة، (6) الشبكة العصبية المعتمدة على الوقت الحقيقي للتحكم بعملية الخراطة، (7) التصميم الجرافيكي لنظام تحكم لرافعات الحاويات الكبيرة: النظرية و التجارب. حيث تراوحت منهجية البحث في هذه المقالات ما بين التحليل العلمي والتشبيه الرياضي والتجارب والدراسات العملية.

أتقدم بالشكر العميق لأعضاء هيئة التحرير وأعضاء الهيئة الاستشارية الدولية للمجلة الذين قدموا النصح والمشورة لإصدار هذا العدد من المجلة. كما أتقدم بالشكر والعرفان للزملاء الذين قاموا بتحكيم الأبحاث على الوقت و الجهد الذي بذلوه في مراجعة وتحكيم هذه الأبحاث. وكذلك أتقدم بالشكر لكافة الزملاء للذين تقدموا بأبحاثهم للمجلة، سواء ما تم قبوله منها أو من لم يقبل، حيث أن أبحاثهم هي العنصر الأساسي في إصدار هذه المجلة.

وختاما، و بالنيابة عن هيئة التحرير و بالأصالة عن نفسي، أرجو أن أكون قادراً على تقديم كل ما هو مفيد لكافة الباحثين والعاملين في قطاعات الهندسة الميكانيكية والصناعية المختلفة من خلال هذه المجلة، آملاً من القراء الكرام عدم التردد في المساعدة وإرسال مساهماتهم واقتراحاتهم واستفساراتهم للارتقاء بهذه الدورية العلمية المتخصصة لما فيه مصلحة الجميع . والله ولي التوفيق.

أ.د. موسى محسن
رئيس هيئة التحرير
الجامعة الهاشمية

المملكة الأردنية الهاشمية

الجامعة الهاشمية

المجلة الأردنية
للهندسة الميكانيكية والصناعية

JJMIE

مجلة علمية عالمية محكمة

http://jjmie.hu.edu.jo/

ISSN 1995-6665

المجلة الأردنية للهندسة الميكانيكية والصناعية

مجلة علمية عالمية محكمة

المجلة الأردنية للهندسة الميكانيكية والصناعية: مجلة علمية عالمية محكمة أسستها اللجنة العليا للبحث العلمي، وزارة التعليم العالي والبحث العلمي، الأردن، وتصدر عن عمادة البحث العلمي والدراسات العليا، الجامعة الهاشمية، الزرقاء، الأردن.

ترسل البحوث إلى العنوان التالي:

رئيس تحرير المجلة الأردنية للهندسة الميكانيكية والصناعية

عمادة البحث العلمي والدراسات العليا

الجامعة الهاشمية

الزرقاء - الأردن

هاتف : 3903333 5 00962 فرعي 4147

Email: jjmie@hu.edu.jo

Website: www.jjmie.hu.edu.jo